Applications of Rheo-NMR-Microscopy to Complex Fluids.

A thesis presented in partial fulfilment of the requirements
for the degree of Doctor of Philosophy in Physics
at
Massey University
by Craig Rofe

May 6, 1997

Abstract

The non-Newtonian behavior of various complex fluids is described in detail, including shear thinning, slip and spurt phenomena. Dynamic NMR microscopy velocity profiles, achieved in capillary, cylindrical-Couette and cone-and-plate geometries, demonstrate that direct measurement of the above phenomena is possible.

NMR diffusion measurements, using polyethylene oxide solutions, reveal that the onset of entanglements is observed at a concentration around 1-2 % (w/v). Shear thinning is observed in 5 % monodisperse polyethylene oxide solutions using capillary velocity profiles. A power law analysis demonstrates an increase in shear thinning with increasing shear rate. A decrease in the power law exponent, n, from 0.4 to 0.35 is observed over the range of shear rates used here.

Slip is demonstrated by the discontinuous velocity profile obtained using 0.2 % Unam Xanthan solutions. An increase in the amount of slip with increasing shear stress is suggested, demonstrated in both capillary and cylindrical-Couette geometries. The exclusiveness of slip to particular Xanthan gums is also shown.

Velocity distributions of Cetyl Pyridinium Chloride-Sodium Salicylate micelles demonstrate the spurt phenomenon as a process observed above a critical shear stress, σ_c. This process is thought to differentiate from that of slip in that its properties rely on bulk fluid properties.

The mobility of polyolefins, containing side chains, were investigated by relaxation measurements in the melt. As the polymers were sheared, a decrease in the mobility was observed, consistent with the disentanglement of the chain network. Viscosity scaling laws, and the influence of polymer side branch length, were also studied.

Gradient coil developments are also described in detail. Linearity, homogeneity and screening conditions are investigated for a transverse quadrupole-target-field gradient coil. The need for large gradients are discussed with the implications to removing susceptibility effects found with model and natural systems.

Acknowledgements

This thesis is dedicated to Mina McKenzie who is greatly missed amongst her family and the wider community. Mina and I often talked about celebrating the completion of this thesis together, but even though our relationship has changed, we will celebrate together *and* apart. She still continues to guide me throughout my life, enabling me with strength and clarity for a sometimes puzzling world.

I thank my father for his continued support with education throughout my youth. A person who has the supported vision that education is the key in breaking negative cyclic trends for young Māori.

To Professor Paul Callaghan, my chief supervisor, thank you for your patience and guidance in the completion of this thesis. The six year journey we have undertaken has led us through crests and troughs but now we find ourselves on te maunga!

As is always the case, I will undoubtedly forget to thank everyone I want to, but here is an honest attempt:
Associate Professor Rod Lambert for his discussions on rheology and general co-supervisor role.

Geoff Nesbitt for his foster parent qualities and also giving me the opportunity to do research at Shell Research, Amsterdam, The Netherlands. Antonio Wilson and the AG/32 department for their warmth and support during the cold Dutch winter.

Lourdes de Vargas for inspiring me with her eternal high spirits, a 100% true Mexican woman scientist.

Bas Smeulders for his careful guidance with the wormlike micelle experiments.

Noel Foot, Steve Denby and other electronic workshop-support staff for their constant harassment in preparation for the 'outside' world.

Stephanie O'Sullivan for her constant support of my work.

My friends, Peter Saunders, Andrew Coy, Yang Xia and Bertram Manz, thank you for your support.

To others who have helped me directly, and indirectly, thank you.

Finally to my family, Louisa McKenzie and Emma McKenzie-Young, thanks for providing me with a warm and safe environment to take shelter from my thesis.

Contents

Abstract i

Acknowledgements ii

Table of Contents iv

List of Figures v viii

List of Tables ix xii

1 Rheo-NMR of Complex Fluids 1

1.1 Viscoelasticity 1

1.2 Macroscopic and Microscopic Views 2

1.3 Rheo-NMR 2

2 Rheological Background 4

2.1 Viscoelasticity 4

2.1.1 Linear Viscous & Elastic Behavior 5

2.1.1.1 The Generalised Maxwell Model 6

2.1.2 Non-Linear Viscoelasticity 7

2.1.2.1 The Maxwell Model 7

2.1.2.2 Shear Thickening, Shear Thinning and The Power Law Model 8

2.1.3 Molecular Models for Viscoelasticity 9

2.2 Classical Rheometry 9

2.3 Slip and Spurt 11

2.3.1 Slip 11

2.3.2 Spurt 13

2.4 Molecular Basis of Viscoelasticity 16

2.4.1 Rigid Rod 16

2.4.2 Isolated Polymer Random Coils 16

2.4.3 Entangled Polymer Random Coils 17
2.4.4 Wormlike Surfactants 20

3 Nuclear Magnetic Resonance (NMR) 21
3.1 Basic Theory of NMR 21
3.1.1 Quantum Description 21
3.1.1.1 Excitation and the Rotating Frame 23
3.1.1.2 Ensemble Averaging of the Nuclear States 24
3.1.2 Semi-Classical Description 26
3.1.2.1 Excitation 26
3.1.3 Relaxation 29
3.1.4 Chemical Shift 30
3.1.5 Signal Detection 30
3.2 NMR Microscopy 33
3.2.1 Gradients 33
3.2.2 Spatial Encoding 33
3.2.2.1 Spin Density and k-Space 33
3.2.2.2 Fourier Imaging 34
3.2.3 Encoding for Motion 36
3.2.3.1 q-Space Imaging 36
3.2.4 Combining Spatial and Motional Encoding 38
3.3 Software and Hardware used in NMR 39
3.3.1 Imageshow 39
3.3.2 Spectrometers 39
3.4 Rheometers 40
3.4.1 The Capillary Rheometer 41
3.4.2 The Cylindrical-Couette Rheometer 42
3.4.3 Combined Cylindrical-Couette-Cone-and-Plate Rheometer . 44
3.4.4 Power Law Velocity Profiles 49

4 Shear Thinning of Semi-Dilute PEO Solutions 50
4.1 Diffusion & Velocity Measurements 51
4.1.1 Experimental Setup 51
4.1.2 Results 53
4.2 Discussion 59
4.3 Conclusions 61

5 Slip Behavior of Xanthan Gum Solutions **63**
5.1 Xanthan Gum 63
5.1.1 Structure 64
5.1.2 Properties 64
5.1.3 Molecular Weight Distribution 65
5.2 Cone and Plate Viscosity Measurements 68
5.3 Velocity Measurements in Cylindrical-Couette Flow 71
5.3.1 Experimental Setup 71
5.3.2 Results 73
5.4 Velocity Measurements in Capillary Flow 79
5.4.1 Experimental Setup 79
5.4.2 Results 79
5.4.3 Discussion 87
5.5 Conclusions 89

6 The Spurt Effect of Wormlike Micelles **91**
6.1 Cetyl Pyridinium Chloride/Sodium Salicylate Micelle 91
6.1.1 Structure 91
6.1.2 Rheology 92
6.1.2.1 Strain-Controlled Experiments 92
6.1.2.2 Stress-Controlled Experiments 97
6.2 Determination of Flow Curve Using MRI 100
6.3 Velocity Measurements 100
6.3.1 Setup 100
6.3.2 Results 101
6.3.3 Discussion 105
6.4 Conclusions 109

7 Mobility of Polyolefins **110**
7.1 Polymerisation of Carishop Polymers 110
7.2 Setup 113
7.2.1 Previous Results 113
7.2.1.1 Polyolefin Characterisation 113
7.2.1.2 Viscosity Anomaly 114
7.3 Results 117
7.3.1 Viscosity Measurements 117
7.3.2 Relaxation Measurements 120
7.3.2.1 T_2 Zero Shear 120
7.3.2.2 T_2^* Influence of Shear 126

7.4 Conclusions 128

8 Large Magnetic Field Gradients **129**
8.1 The Need for Large Magnetic Field Gradients 129
8.2 Probe Development 130
8.2.1 The Quadrupole Gradient Coil 130
8.2.1.1 Homogeneity and Gradient Calculations 133
8.2.1.2 Active Screening of the Quadrupole Coil's 'End Fields' 135
8.2.1.3 Eddy Field Calculations 139
8.2.2 The Target-Field Gradient Coil 144
8.2.2.1 The Target Function 145
8.2.2.2 Homogeneity and Gradient Calculations 149
8.2.2.3 Former Design and Wiring 149
8.2.2.4 Gradient Strength and Eddy Current Testing . . . 152
8.3 High Spatial Resolution & Double Phase Encoding 154
8.3.1 Susceptibility Effects 154
8.3.2 Diffusive Effects 156
8.3.2.1 Homogeneous Systems 156
8.3.2.2 Heterogeneous Systems 157
8.3.3 Experimental Setup 157
8.3.4 Experimental Results 158
8.4 Conclusions 165

9 Future Directions **166**
9.1 Revisiting Experiments 166
9.2 New Experiments 167

Bibliography **169**

Author's Publications Arising From Thesis **175**

List of Figures

2.1 Cartesian stress coordinates. 4
2.2 Maxwell element: spring-dashpot. 6
2.3 Flow curve: shear thinning, shear thickening and Newtonian behavior. 9
2.4 Slip layer hypothesis. 12
2.5 Flow curve: stress minimum and stress plateau. 14
2.6 Capillary flow: shear band. 15
2.7 Polymer: random coil-bead spring analogy. 17
2.8 Reptating polymer. 18

3.1 Proton's discrete energy levels. 22
3.2 Rotating $\mathbf{B_1}$ field components. 24
3.3 Simultaneous precession of magnetisation. 28
3.4 Fast and slow motional regimes 29
3.5 Free induction decay and spectra. 32
3.6 Fourier imaging pulse sequence. 35
3.7 Pulsed gradient spin echo pulse sequence. 36
3.8 Fast Fourier transform of 3-D $\mathbf{q}$ data set. 40
3.9 Capillary rheometer. 41
3.10 Cylindrical-Couette rheometer. 43
3.11 Cone-and-plate rheometer. 44
3.12 Combined cone-and-plate-cylindrical-Couette rheometer. 47
3.13 Combined cylindrical-Couette-cone-and-plate rheometer and driving motor. 48

4.1 Capillary system for PEO. 52
4.2 Diffusive echo attenuation of 930 000 da PEO/D_2O. 54
4.3 Entanglement concentration for PEO 55
4.4 Cylindrical-Couette velocity profile for water. 56
4.5 Cylindrical-Couette velocity comparison H2O/PEO. 56
4.6 Cylindrical-Couette velocity comparison PEO vs frequency. 57

4.7 Cylindrical-Couette power law fit for PEO. 57
4.8 Capillary power law fit for PEO. 58
4.9 PEO viscosity scaling. 60
4.10 PEO logarithmic viscosity scaling. 61
4.11 Migration profile. 62

5.1 Xanthan primary structure. 64
5.2 GPC of Xanthan solutions. 67
5.3 Constant shear viscosity response of Unam Xanthan solution within cone-and-plate geometry. 69
5.4 Dynamic response of Unam Xanthan solution. 70
5.5 Cylindrical-Couette geometry within super-conducting magnet. . . 71
5.6 **q** image data processing. 75
5.7 Velocity stackplot of Unam Xanthan solution within cylindrical-Couette geometry. 76
5.8 Double slice velocity pulse sequence. 76
5.9 (a) Velocity distribution of Unam Xanthan solution within cylindrical-Couette rheometer. (b) Comparison of normalised velocities versus frequency. 77
5.10 Power-law velocity profile fit for cylindrical-Couette geometry. . . . 78
5.11 Velocity profile across capillary of Xanthan solution versus flow rate. 80
5.12 Normalised velocity distribution across pipe of Unam Xanthan solution versus flow rate. 81
5.13 Power law velocity profile fitting across pipe of Unam Xanthan solution. 82
5.14 Comparison of normalised velocity profiles along pipe. 83
5.15 Comparison of normalised velocity profiles at varying reservoir-pipe contractions. 84
5.16 Power law velocity profile fit across pipe for smallest reservoir-pipe contraction ratio. 84
5.17 Velocity profile across capillary of Unam solution after peristaltic pumping. 85
5.18 Velocity profile across pipe of Aldrich and Kelsan Xanthan solutions. 85
5.19 Slip velocity versus wall stress of imaging and rheometry. 86

6.1 Cetyl Pyridinium Chloride/Sodium Salicylate wormlike micelle structure. 92
6.2 Linear regime of CPyCl/NaSyl wormlike micelle. 93
6.3 Dynamic response of CPyCl/NaSyl wormlike micelle. 94

6.4 Time response of CPyCl/NaSyl wormlike micelles when experiencing different magnitude step-strains. 95
6.5 Response of CPyCl/NaSyl wormlike micelles with strain-controlled experiment. 96
6.6 Response of CPyCl/NaSyl wormlike micelles with stress-controlled experiment. 98
6.7 Enhanced flow instability of CPyCl/NaSal wormlike micelles with phase transition. 99
6.8 CPyCl/NaSal wormlike micelles capillary velocity profiles. 102
6.9 Normalised capillary velocity profiles for CPyCl/NaSal wormlike micelles. 103
6.10 Velocity profile for CPyCl/NaSal micelle in cylindrical-Couette geometry. 104
6.11 Calculated local shear rate versus position of CPyCl/NaSal micelles in capillary geometry. 106
6.12 Flow curve of CPyCl/NaSal calculated from its local shear rate in capillary geometry. 107
6.13 Calculated capillary velocity profiles of CPyCl/NaSal micelles. . . 108

7.1 Olefin primary and secondary insertion reaction. 111
7.2 Tacticity processes of polyolefins. 112
7.3 Previous viscosity anomaly of C_{10-18} 116
7.4 Massey PGSE probe. 117
7.5 Combined rheometer viscosity measurements of $C_{10,12,18}$ polyolefins. 118
7.6 C_{12} viscosity measurements. 119
7.7 Spin echo pulse sequence. 120
7.8 T_2 measurements for C_{12} polyolefin. 120
7.9 Comparison of T_2 measurements for mono-disperse polypropylene and C_{12} polyolefin. 121
7.10 Binary T_2 echo decay. 124
7.11 Deconvolution of polyolefin spectrum. 124
7.12 T_2 measurements for different Carishop. 125
7.13 T_2^* for C_{12} and C_{18} under shear. 127

8.1 Quadrupole coil orientation. 131
8.2 Quadrupole coil's magnetic field distribution. 132
8.3 Discrete wire configuration for quadrupole coil. 132
8.4 Calculated gradient magnitude for quadrupole coil. 134
8.5 Calculated gradient homogeneity for quadrupole coil. 134

8.6 Cylindrical polar coordinate system for current distributions. . . . 135
8.7 Screening volume for transverse coil. 138
8.8 Dummy saddle coil dimensions. 140
8.9 Gradient calculations for dummy saddle coil. 141
8.10 Three dimensional magnetic field plot- dummy saddle coil and quadrupole coil. 142
8.11 Comparative field profiles- saddle and quadrupole coils. 143
8.12 Calculated current inverse space distributions. 146
8.13 Calculated real space current distributions. 147
8.14 Calculated wire paths. 148
8.15 Quadrupole gradient coil probe. 150
8.16 Rf tuning circuit. 151
8.17 Pre-emphasis pulse sequence. 152
8.18 Phase-frequency and phase-phase spin echo pulse sequences. 155
8.19 Phase-frequency and phase-phase spin echo pulse sequence used for glass/acetone image comparison. 161
8.20 Geranium stem images which used phase-frequency and double phase encoding schemes. 162
8.21 Double phase encoding ability to provide chemical selection. 163
8.22 Experimental and calculated diffusive attenuation under phase-phase encoding scheme. 164

List of Tables

7.1 Molecular weight of polyolefins using GPC, GPC-light scattering . 113
7.2 Viscosity trend of polyolefins using GPC-light scattering. 115
7.3 Proton Magnitude 122

8.1 Experimentally determined gradient magnitudes for the quadrupole and target field gradient coils. 152
8.2 Inductance and resistance measurements of the quadrupole-target-field gradient coils. 153

Chapter 1

Rheo-NMR of Complex Fluids

1.1 Viscoelasticity

The behavior of materials under mechanical deformation has important implications for industry. Both the polymer and food processing industries have major research interests in this type of material science, since many manufacturing processes depend upon a substance's behavior when *stressed.* For example, polymers are commonly produced by an extruder type process which mixes the materials in a 'cork screw' mechanism.

The simplest approach in characterising the mechanical behavior of materials is to class the materials into two extreme categories, namely *viscous* or *elastic.* Liquids and solids are typically included in these sections respectively. The viscous nature of materials was first studied by Isaac Newton in 1687[1] who characterised the materials as having a *shear stress* that was directly dependent upon the *rate of shear strain.* In contrast to this description, elastic materials have a shear stress which is sensitive to the *amount* of strain. The principal studies on this phenomena were carried out by Robert Hooke in 1676[1].

Many materials are not well described by either simple category, exhibiting both viscous *and* elastic behavior. These substances are known as *viscoelastic.* The distinction between solid and liquid is not clear for such a class of materials. Furthermore, even materials commonly thought of as liquid or solid will exhibit such limiting behavior only over certain observational time scales. As we shall see, the response of a material depends on the relative magnitude of the material's relaxation time to the time of observation. For example, the relaxation time for water is on the order of 10^{-12} s, whereas silicate glass is $> 10^5$ s. Compared to the time over which one typically observes deformation ($\approx$ms to years), silicate glass appears to be a solid and water a liquid. An equal and alternative view would be

to characterise glass as a super-cooled fluid.

1.2 Macroscopic and Microscopic Views

In practice the viscoelastic behavior of materials is observed from the response to an applied force. The engineering approach is to investigate the *macroscopic* behavior of a substance. For 'solids' it is the *displacement* (strain) which is investigated as opposed to 'liquids' where the *rate* of displacement (rate of strain) is studied. For general viscoelastic materials the response to applied stress may be used to define the constitutive properties of the material. Constitutive descriptions do not require a knowledge of molecular structure.

In the microscopic view point, it is the molecular properties which govern the constitutive behavior of materials. Molecular models take account of local entropic and enthalpic interactions, of molecular organisation and molecular dynamics in order to predict constitutive behavior. In this thesis we will be concerned with molecular descriptions for 'random coil'[2], 'rigid rod'[3] and 'wormlike surfactant'[4] systems. We shall see that the organisation of the molecules plays an important role in determining the behavior of complex fluids experiencing stress. The aspects of organisation dealt with here will include entanglements and self-assembly. Finally, it is important to emphasise that the dynamical behavior, in particular molecular rotation of diffusion will play a crucial role in determining constitutive properties.

1.3 Rheo-NMR

The term *rheology* was coined by E.C. Bingham[1] in 1929. He defined rheology as "the study of the deformation and flow of matter." The origins of rheology can be traced to Newton and Hooke although some authors attribute its origins to the Egyptians in the sixteenth century BC. However it emerged as a separate field of research in the 1920's when industrial use of plastics, rubbers and clays became more widespread. Rheology is arguably the study in which both the constitutive behavior *and* molecular properties of a material are combined. An experimental tool is required to link both the molecular and viscoelastic behavior of materials. Various techniques used to study rheological behavior include neutron scattering[5, 6], optical birefringence[7, 8] and laser Doppler anemometry[9]. Although some work on molecular orientation while under shear is noted with neutron scattering[10], broadly classifying, the previous techniques rely on a macroscopic interaction with the measuring device. However, *Rheo-NMR*[11] combines *Nuclear Magnetic Reso-*

nance of materials with the application of mechanical stress. In doing this, NMR can act as a molecular probe, providing a technique which offers information of viscoelastic behavior at both microscopic *and* macroscopic scales. For example, relaxation parameters are available associated with a molecule's rotational tumbling or morphological constraints while being sheared. An additional asset Rheo-NMR provides is the ability to measure a molecule's displacement caused by stress. This measurement may take the form of a diffusion or velocity profile where the latter (refer Xia & Callaghan[12]), as we will see, provides an idea of the local rate of strain. Although dual point laser Doppler anemometry is noted for the direct measurement of the strain rate[9], the method however is insufficient in providing measurement at a molecular scale.

This thesis investigates the way in which NMR measurements of velocity may be used to study rheological behavior. One aim of this thesis is to 'marry' the molecular description of materials with constitutive parameters derived from velocity profile measurements. Another aim has been to focus on the development of the velocity measurement in geometries not previously investigated using NMR. The investigation includes a study of model systems covering a range of molecular structures.

Chapter 2

Rheological Background

2.1 Viscoelasticity

In this chapter we will deal with the response a *viscoelastic* material has when subjected to stress, σ. Stress is defined as force, F, per unit area, S, according to:

$$\sigma_{ij} = \frac{F_j}{S_i} \tag{2.1}$$

where the first index refers to the orientation of the area normal and the second,

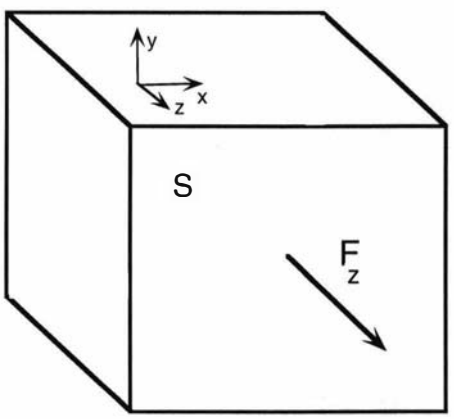

Figure 2.1: A material experiencing a force, F_z, normal to the surface, S, has a stress component defined as σ_{zz}.

to the direction of the force. These relationships are illustrated in figure 2.1. Because of the three possible area and force directions, a stress tensor having nine components can be defined. It can be shown[13] that the stress tensor is symmetric ie. $\sigma_{ij} = \sigma_{ji}$. Thus for the cartesian coordinate system adopted here $\sigma_{xy} = \sigma_{yx}$, $\sigma_{yz} = \sigma_{zy}$ and $\sigma_{xz} = \sigma_{zx}$. This equality arises from considering the

angular momentum of an element of a fluid. Thus with the fluids presented in this thesis, only *six* constitutive equations of state are required.

Two further parameters, used to describe rheological behavior, are the 'normal stress differences' (N_1, N_2):

$$N_1 = \sigma_{xx} - \sigma_{yy} \tag{2.2}$$

$$N_2 = \sigma_{yy} - \sigma_{zz} \tag{2.3}$$

For an incompressible fluid mass conservation requires:

$$\frac{\partial v_x}{\partial x} + \frac{\partial v_y}{\partial y} + \frac{\partial v_z}{\partial z} = 0 \tag{2.4}$$

where v_x, v_y and v_z are the cartesian components of the velocity of the fluid. The forces on the fluid within a volume and on the surface of that volume can be equated to the rate of change of momentum of the fluid. The result is:

$$\frac{\partial \sigma_{ij}}{\partial x_j} + \rho f_i = \rho \left\{ \frac{\partial v_i}{\partial t} + v_j \frac{\partial v_i}{\partial x_j} \right\} \tag{2.5}$$

where ρ is the homogeneous density and f_i is the body force per unit mass acting on the fluid. Eqn. (2.5) is referred to as the fluid's momentum equation and is sometimes expressed as the 'Navier-Stokes' equation, when the Newtonian constitutive relationships are incorporated.

Although all of the above relationships are not used in this thesis, they are mentioned for completeness. Note that in this thesis we shall be principally concerned with *shear* stress of which there are three components: σ_{12}, σ_{23} and σ_{13}.

2.1.1 Linear Viscous & Elastic Behavior

The response of a system to stress is described by the constitutive relations for that material. This response is measured by strain or its time derivatives. For small shear strains, γ, linear relationships can be expressed in the form[2]:

$$\left\{ 1 + \alpha_1 \frac{\partial}{\partial t} + \alpha_2 \frac{\partial^2}{\partial t^2} + \ldots + \alpha_n \frac{\partial^n}{\partial t^n} \right\} \sigma = \left\{ \beta_0 + \beta_1 \frac{\partial}{\partial t} + \beta_2 \frac{\partial^2}{\partial t^2} + \ldots + \beta_n \frac{\partial^n}{\partial t^n} \right\} \gamma \tag{2.6}$$

If β_0 is the only non-zero parameter we then have:

$$\sigma = \beta_0 \gamma \tag{2.7}$$

where the equation describes the Hookean type behavior typical of solids. β_0 is the elastic modulus, g. When β_1 is the only non-zero parameter, Newtonian viscous behavior, characteristic of a simple liquid, is described:

$$\sigma = \beta_1 \frac{\partial \gamma}{\partial t} \tag{2.8}$$

where β_1 is more commonly known as the Newtonian shear viscosity, η_0.

2.1.1.1 The Generalised Maxwell Model

In this thesis we will be concerned with fluids which exhibit both elastic and viscous behavior. The simplest linear viscoelastic model is the 'Maxwell model' for which all the coefficients in Eqn. (2.6) are zero except for α_1 and β_1. This leads to the following differential equation:

$$\sigma + \lambda\dot{\sigma} = \eta\dot{\gamma} \tag{2.9}$$

where λ is known as the relaxation time. The meaning of λ is more apparent when the solution to Eqn. (2.9) is sought. When a constant shear rate is applied at time $t = 0$, the stress at time, t, is:

$$\sigma(t) = \sigma_0 \left(1 - e^{-\frac{t}{\lambda}}\right) \tag{2.10}$$

where σ_0 is the resultant equilibrium stress as t approaches infinity, given by $\eta\dot{\gamma}$. Thus the shear stress grows exponentially to reach σ_0. The mechanical analogy to the Maxwell element is a spring connected in series with a dashpot (see Fig 2.2). A simple analysis based on this model suggests $\lambda = \frac{\eta}{g}$.

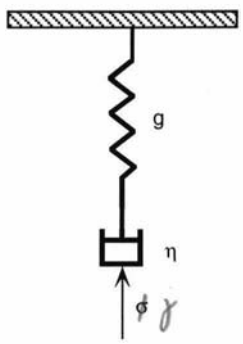

Figure 2.2: A Maxwell element consists of a spring with elastic modulus, g and a dashpot with viscosity, η.

The *generalised* Maxwell model introduces a spectrum of relaxation times, λ_i, describing the behavior of i Maxwell elements connected in parallel. A material's constitutive equation can also be expressed in terms of its history and present response (see Eqn. (2.14). Such a relationship can include a *memory function* which describes the rate of change of the ratio of stress and strain. For a Maxwell model the memory function has the form:

$$M(t) = \sum_i \left(\frac{g_i}{\lambda_i}\right) e^{\frac{-(t-t')}{\lambda_i}} \tag{2.11}$$

With oscillatory shear it is common to define a *complex modulus* which describes the magnitude and phase of the shear stress as a function of frequency. The *loss* (G') and *storage* (G'') moduli are defined as the in phase and quadrature response respectively. When the Maxwell model is adopted, the storage and loss moduli have the following dependence:

$$G'(\omega) = \sum_i \frac{g_i \lambda_i^2 \omega^2}{(1+\lambda_i^2\omega^2)} \tag{2.12}$$

$$G''(\omega) = \sum_i \frac{g_i \lambda_i \omega}{(1+\lambda_i^2\omega^2)} \tag{2.13}$$

The memory function (Eqn. (2.11)) can be determined by measuring the frequency dependence of G' and G''. By fitting the observed behavior with equations (2.12) and (2.13) the spectrum of relaxation times can be determined. Since the Maxwell function used here describes a material only in its linear region, it is essential the extent of this region be determined.

2.1.2 Non-Linear Viscoelasticity

The non-linear behavior of materials will be a significant subject of the study in this thesis. Non-linear viscoelacticity concerns the response of a system experiencing large strains and in particular the dependence of shear stress on rate of strain under steady state conditions. We begin by considering a variation of the Maxwell model which will be appropriate in the description of the wormlike surfactant system described in section 2.4.4.

2.1.2.1 The Maxwell Model

Non-linear behavior can be incorporated into the Maxwell model if a damping function ($e^{-k|\gamma|}$) is introduced, where k is the damping coefficient. This adaption of the Maxwell model was originally described by *Wagner*[14]. The constitutive equation (Eqn. (2.14)) combines the memory function (Eqn. (2.11)) with the damping function as follows:

$$\sigma'(t) = -\int_{-\infty}^{t} \sum_i \frac{g_i}{\lambda_i} e^{-\frac{(t-t')}{\lambda_i}} |\gamma(t,t')| e^{-k|\gamma(t,t')|} dt' \tag{2.14}$$

This type of rheological description relies on the time and strain dependent parts of the constitutive equation being separable. The damping coefficient k is determined by carrying out a series of step-strain experiments with varying magnitudes of deformation. The strains can vary from linear regions to non-linear regions. The

relaxation modulus, $G_0(t)$, is dependent, for linear strains, only on the spectrum of relaxation times, thus leading to an exponential decay:

$$G_0(t) = \sum_i \frac{g_i}{\lambda_i} e^{-\frac{t}{\lambda_i}} \tag{2.15}$$

For non-linear strains the value of the relaxation modulus is lowered for a strain-softening material. Providing the strain is time independent it follows that the shape of the curves will not depend on strain:

$$G(t) = e^{-k\gamma} \sum_i \frac{g_i}{\lambda_i} e^{-\frac{t}{\lambda_i}}$$

By comparing the relaxation moduli for the linear and non-linear regions, the damping coefficient can be determined as shown in equation (2.16).

$$e^{-k\gamma} = \frac{G(t)}{G_0(t)} \tag{2.16}$$

A plot of $\ln(\frac{G(t)}{G_0(t)})$ vs γ will yield a straight line of slope, $-k$.

A final check as to the consistency of the Maxwell-Wagner model can be achieved by steady shear measurements. It can be shown that the shear stress can be determined if λ_i and k are known, namely[14]:

$$\sigma(\dot{\gamma}) = \sum_i \frac{\eta_i \dot{\gamma}}{(1 + k\lambda_i \dot{\gamma})^2} \tag{2.17}$$

This theoretical prediction may then be compared to the measured flow curve of σ vs $\dot{\gamma}$.

2.1.2.2 Shear Thickening, Shear Thinning and The Power Law Model

As well as the Maxwell model used to describe the non-linear characteristics of a material many other models are possible. One empirical characterisation which is widely used is known as the *Power Law* relationship, in which the shear stress is related to the shear rate via:

$$\sigma_{xy} = m\dot{\gamma}^n \tag{2.18}$$

$$\Rightarrow \eta(\dot{\gamma}) = m\dot{\gamma}^{n-1} \tag{2.19}$$

where m is a constant. It can be seen from Eqn. (2.19) that, a value of $n > 1$ would result in a viscosity increase with increasing shear rate, thus characterising a shear thickening material. Alternatively, the cases $n = 1$ or $n < 1$, describe Newtonian and shear thinning behavior respectively. The characteristic stress curvature in both shear thinning and shear thickening is seen in Fig 2.3. The molecular basis

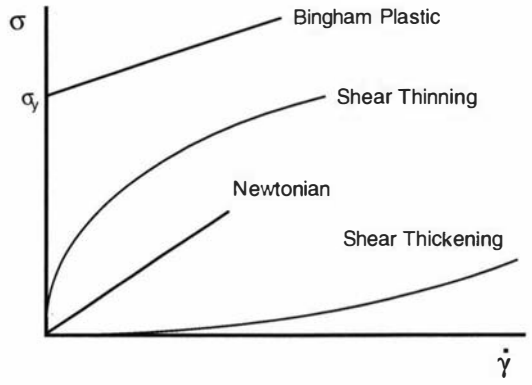

Figure 2.3: The reduction of viscosity with increasing shear rate is termed a shear thinning process, the reverse, a shear thickening process.

for shear thickening and shear thinning will be discussed later in the context of polymer entanglements.

Some materials, known as Bingham plastics, exhibit a yield stress, σ_y, as shown in figure 2.3.

2.1.3 Molecular Models for Viscoelasticity

The generalised Maxwell model and the power law fluid equation describe macroscopic constitutive behavior without reference to molecular origin. In this thesis we shall be particularly concerned with the non-linear viscoelastic behavior of polymer solutions, including random coil, rigid rod and wormlike surfactant solutions. Molecular models will be discussed in section 2.4.

2.2 Classical Rheometry

In the traditional approach to rheometric measurements one measures a material's stress while it is being deformed. The stress is measured indirectly by measuring either the resultant pressure or force. An alternative and similar process for measurements consists of measuring the deformation, or rate of deformation of a material, while it is experiencing a given stress. The common geometries used for such measurements are known as the *cone-and-plate*, *cylindrical-Couette* and *capillary*. Each geometry has a characteristic shear field.

The cone-and-plate apparatus consists of a cone held vertically above a rotating circular plate. The details of this geometry can be found later in section 3.4.3. The applied shear rate is calculated for a given angular velocity of the plate in

accordance with the known cone angle. The shear rate is radially uniform for this geometry and provides an excellent environment for experiments which require a homogeneous shear rate. The stress in the material is determined from the torque on the cone while the bottom plate is rotated. Because of the known geometry, the contact surface area is known and the stress can be calculated.

An alternative but similar rotating geometry is the cylindrical-Couette, where a material is placed in the annular gap between two concentric cylinders of different radii. Either the outer or inner cylinder is rotated and the resultant stress is again indirectly measured by the torque experienced on the non-rotating cylinder. Although this geometry does not provide a homogeneous shear rate with increasing radius, it does however provide a near perfect homogeneity when the gap is small. The approximation is discussed in detail in section 3.4.2.

In capillary geometry the material is pumped through a pipe of known diameter. The shear rate is determined from knowledge of the flow rate and the shear stress from pressure difference, ΔP, across the pipe length, l. In particular, the wall shear stress and shear rate are often sought. The theoretical velocity distribution for a Newtonian material in this geometry is given by Eqn. (2.20). R is the radius of the capillary and v_{max}, the maximum velocity of the fluid in the tube. The local shear rate is given by the derivative of Eqn. (2.20) w.r.t. r, (Eqn. (2.21)). The maximum shear rate at the capillary wall is given by Eqn. (2.22)

$$v(r) = v_{max}\left[1 - \frac{r^2}{R^2}\right] \tag{2.20}$$

$$\frac{\partial v(r)}{\partial r} = \dot{\gamma} = \frac{2v_{max}r}{R^2} \tag{2.21}$$

$$\Rightarrow \dot{\gamma}_{wall} = \frac{2v_{max}}{R} \tag{2.22}$$

$$= \frac{4Q}{\pi R^3} \tag{2.23}$$

$$= \frac{32Q}{\pi D^3} \tag{2.24}$$

where Q is the volume flow rate $\frac{1}{2}\pi R^2 v_{max}$. Even when the velocity distribution is not parabolic, equation (2.24) can be used to define an *apparent* shear rate.

Whatever the constitutive behavior of the fluid, the wall shear stress is always given by:

$$\sigma = \frac{\Delta P R}{2l} \tag{2.25}$$

where $\frac{\Delta P}{l}$ is the pressure gradient along the pipe. The capillary rheometers that were used in this thesis are described in section 3.4.1.

2.3 Slip and Spurt

In many of the capillary flow studies in this thesis, the simple parabolic velocity profile did not occur because of the strongly non-Newtonian properties of the fluid. One particular example of strong non-Newtonian deviation concerns apparent slip at the wall of the pipe. Slip may be associated with some perturbation to the fluid property near the wall surface which allows very high local shear rates. Another cause of high shear rate may be 'spurt' associated with discontinuities in the fluid constitutive behavior, a bulk property unrelated to surface effects but only with the high stress at the outer layers of the fluid.

2.3.1 Slip

The apparent slip phenomenon refers to the existence of a narrow region of very high shear rate next to a solid surface. It appears as if the non-slip condition has been violated. It is often caused by an abnormally low viscosity of a fluid mixture in an inhomogeneous stress field due to solute-wall interaction. In other words, an enhanced fluid flow is observed at a particular stress level in excess of that expected in the absence of direct wall effects. Experimental evidence has shown an increase of up to 50 % of the viscometric predictions (based on cone-and-plate data) is possible[15] in some polymer systems. Such an observation is associated with the apparent slip phenomenon.

The slip phenomenon is not new and has been documented in many earlier studies of Green[16], Scott-Blair[17], Reiner[18] and Mooney[19]. The last author provided a method for determining the magnitude of any violations of the 'no slip' condition. Other studies documented slip effects for the flow of suspensions[20], polymer melts[21] and polymer solutions[22]. The Mooney[19] analysis of apparent slip in capillary flow is based on a hypothetical thin slip layer next to the wall. This discontinuity, depicted in figure 2.4, gives rise to an enhanced flow rate, Q. The total flow rate arises from the addition of the velocity fields bounded by $r = 0$ and $r = R - \delta$ to the additional offset slip velocity, V_s, found between $r = R - \delta$ and $r = R$. If the slip layer is small compared to the overall diameter, D, then the flow rate can be expressed:

$$\frac{32Q}{\pi D^3} = 8\frac{V_s}{D} + \frac{4}{\sigma_w^3}\int_0^{\sigma_w} \sigma^2\dot{\gamma}(\sigma)d\sigma \tag{2.26}$$

where σ_w is the shear stress at the capillary wall. Therefore, for a given shear stress at the wall, a plot of $\frac{32Q}{\pi D^3}$ as a function of $1/D$, at constant σ_w, will give a straight line with a constant slope of magnitude $8V_s$. The intercept with the ordinate gives the value of the shear rate without slip (infinite diameter). Thus,

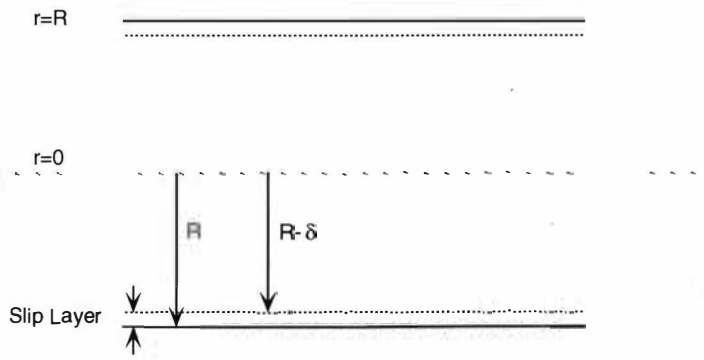

Figure 2.4: The increase in flow in a thin layer, δ, close to the tube walls has been postulated by Mooney to explain the slip phenomenon.

the shear stress vs. shear rate behavior can be determined free from the effects of slip.

It must be emphasised that accurate measurements are required to produce a constant value of the wall shear stress while determining the slip velocity. The Mooney analysis remains the most widely-used method for quantifying apparent slip. Pérez-González et al[23] have reported apparent slip in a capillary geometry using a 0.2% solution of a polysacharide gum known as *Xanthan*. The authors used the Mooney method to obtain the magnitude of the slip velocity for different length, L, to diameter, D, ratios of the capillaries. The conclusion of this study was that the slip velocity is not only a function of the applied shear stress but also dependent on $\frac{L}{D}$. This second dependence was broadly classified into three categories; firstly, small capillary lengths ($\frac{L}{D} < 100$) where end effects were dominant, secondly, where $100 < \frac{L}{D} < 300$ and slip development and end effects exist and thirdly, where $\frac{L}{D} > 300$ and flow is fully developed. The *development* of slip in this study is a unique finding and further investigation is needed into this effect (see section 5.4).

Other attempts have also been made to measure the magnitude of slip in the capillary geometry[24] using Nuclear Magnetic Resonance Velocimetry. A 0.2 % Xanthan solution and a 2.5 % particulate system containing 5-50 μm irregular, soft agar gel particles were used. The results were anything but conclusive as regards to the determination of a slip velocity magnitude, relying on non-zero data points which fall well within the experiment's range of error. The study did however provide a conclusive demonstration of non-Newtonian flow profiles.

A method for correcting for cylindrical-Couette slip has also been reported by

T. Kiljański[25]. The study assumes a linear relationship of the slip velocity as one progresses into the fluid, away from the shearing surface. With this inclusion, the correct shear rate can be calculated for the rheometer. Power-law fluids have not been excluded in this report and can be adequately described with this method. Experimental support was offered by H. Schlegel's[26] work who performed rheological studies in a cylindrical-Couette rheometer for three different gap settings. Again with this study, direct measurement of the slip magnitude has eluded the investigation. The study of slip in this geometry, thus far, allows the possibility of direct measurement of the slip velocity magnitude to be obtained.

2.3.2 Spurt

A discontinuity in the flow behavior of polyethylene was reported[27] in 1958 by Bagley et al. G.V. Vinagradov also investigated this effect[28] and coined the term 'spurt' effect. Other studies, including that of McLeish and Ball[29], offer an explanation of the spurt effect using the Doi-Edward's theory of polymer dynamics to be discussed in section 2.4.3. Spurt is a bulk fluid property which might be expected under conditions of very strong shear thinning sufficient to cause a minimum in the shear stress vs. rate of strain curve. Such conditions might cause an unstable flow, similar to that reported by Vinagradov, once an associated critical shear stress, σ_c, has been exceeded. The instability occurs depending upon the existence of an 'upper branch' on the flow curve as shown in figure 2.5. If the shear stress again increases on the flow curve beyond the minimum, an abrupt change with shear rate can exist for an infinitesimal change with shear stress, $\Delta\sigma$, as depicted in figure 2.5(a).

As will be discussed later in section 2.4.3, a sample's molecular mass and its characteristic mass dispersity may smooth the flow curve resulting in the stress minimum being barely distinguishable. Such a result is shown in figure 2.5(b) where a stress plateau is observed. If the shear stress increases after the plateau, again an abrupt change with shear rate is possible. Thus, the existence of a discontinuity in shear rate is critically dependent on the increase in shear stress or 'upper branch'. It has been suggested that σ_c corresponds to the maximum stress, σ_{max}, found on the flow curve[29] (see Fig. 2.5(a)). In fact where exactly the critical stress lies on the flow curve is uncertain, being described as a hysteresis discontinuity[27, 30]. Thus, it is important at which end of the flow curve, high or low stress, one is approaching the stress region. Although σ_c is unstable, it is guaranteed to be found in the region $\sigma_{min} \leq \sigma_c \leq \sigma_{max}$. In a capillary geometry, McLeish et al also predict the double valuedness of the shear rate will manifest itself in a distinctive '*shear band*' fashion . This involves the local shear rate near

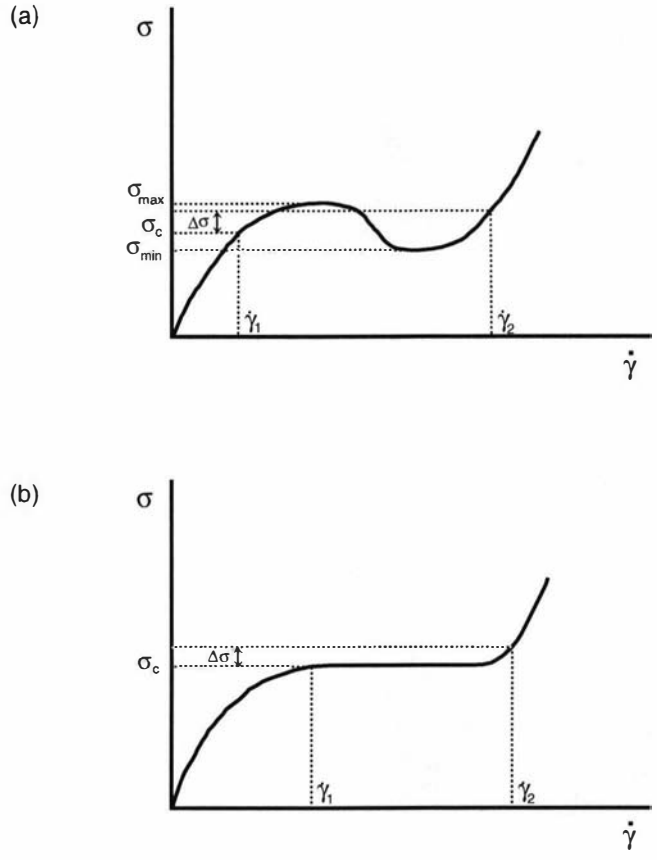

Figure 2.5: (a) With a minimum observed in the flow curve, a small change in stress, $\Delta\sigma$, may result in an abrupt change in shear rate, $\dot{\gamma}_1 \rightarrow \dot{\gamma}_2$. (b) This phenomenon is still possible for when a plateau is observed on the flow curve.

the tube centre changing abruptly to a higher shear rate near the capillary wall. Figure 2.6 shows the development of a shear band, eventually leading to slip at the tube walls, as the pressure gradient along the capillary is increased. If the upturn in the flow curve occurs at sufficiently high shear rates then the band may be narrow and indistinguishable from apparent slip.

A similar abrupt change in local shear rate would be expected in the flow profile obtained for a cylindrical-Couette rheometer if a sufficient shear stress gradient is obtained across the fluid.

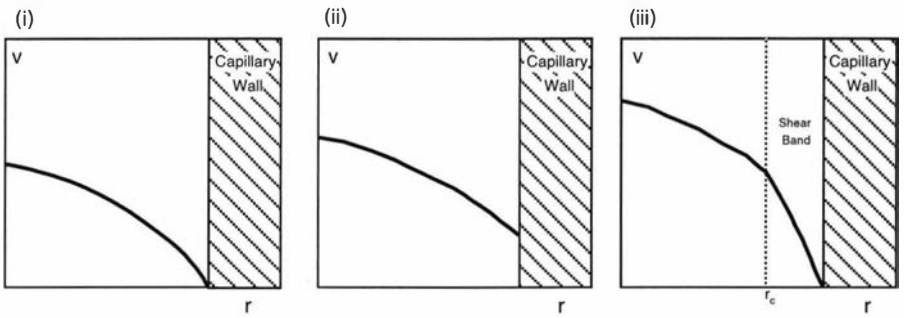

Figure 2.6: The development of flow in a capillary tube, (ii), leads to an enhanced shear rate close to the wall. This phenomenon is akin to slip (refer Sec. 2.3.1) but progresses into the fluid, (iii), at higher flow rates as a shear band.

2.4 Molecular Basis of Viscoelasticity

Molecular models are used to describe the viscoelastic behavior of certain rheological systems. Three such models, with their characteristic inter-actions and behavior are described below.

2.4.1 Rigid Rod

Consider a system where each of the molecules may be thought of as long, thin rods, with little or no flexibility. In a dilute solution, with no flow, the molecules have maximum entropy with random orientation. The interactions of one molecule with another will be dominated by excluded volume effects. Excluded volume effects will also be important in the vicinity of a nonadsorbing, solid wall resulting in concentration inhomogeneity. The non-uniform solute concentration extends over distances comparable to the length of the rod, as the centre of mass cannot approach close to the impenetrable wall. This creates a interfacial depletion layer, for which the exact profile of a rigid rod has been investigated[31]. When the solution is subjected to steady shear, there will be a decrease in entropy corresponding to a storage of elastic energy. This orientation is opposed by Brownian motion, in which the random thermal movements tend to produce a uniform distribution of orientations. The rate of such motion can be characterised by a rotary diffusion coefficient, Υ, or by a relaxation time, $\tau = 1/6\Upsilon$. This parameter is the measure of the time for end-over-end rotation. Additional tumbling of the rod-like molecules may be caused by the shearing forces[31] in which a marked increase in the depletion layer has been postulated. This occurs by the decrease in allowable positions of the rod's centre-of-mass next to the wall, thus enhancing the steric excluded volume effect already present in the fluid at rest. These processes have been suggested as the cause of the slip phenomenon, where a decrease in the viscosity of the fluid, close to the rheometer's walls, is found.

In this thesis we have chosen to investigate the above effects using a polysaccharide called *Xanthan* gum. It is a rod-like molecule, possessing highly non-linear viscosity in dilute solutions[32]. Dilute Xanthan concentrations also exhibit a finite elasticity and have been studied for the effects of slip[23, 33].

2.4.2 Isolated Polymer Random Coils

Another molecular structure found in systems of rheological interest are those where a number of monomers are connected together, in a flexible manner, via a covalent bond. This flexibility[34]– [36] leads to a large configuration space for chain conformation. Because the number of states available to the chain decreases

as the end-to-end distance increases, this results in a reduction in entropy. As

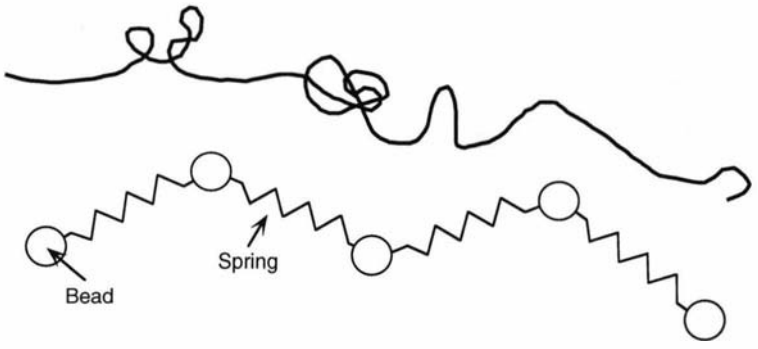

Figure 2.7: The flexible coil nature of a polymer molecule can be represented as a bead-spring model.

a consequence the free energy of an isolated polymer coil will increase as it is stretched causing it to store energy because of the decrease in entropy associated with the restriction of configurations it can assume. For mathematical simplicity it is common to depict the submolecules as a bead-spring model shown in Fig. 2.7. Such a model adequately describes many viscoelastic properties of these materials, such as the frequency-dependent complex moduli[37].

2.4.3 Entangled Polymer Random Coils

Polymer melts and solutions, sufficiently concentrated that random coils are overlapped, are described by different dynamics. The crucial difference concerns the existence of entanglements between chains. Provided the molar mass is larger than a critical value for the onset of entanglements (a fixed value for the melt but concentration-dependent for solutions) the polymer may be thought to be confined to a tube defined by the other polymer members. Movement of the chain consists of Brownian motion along the tube. Eventually this motion enables the chain to enter a new environment, a process known as reptation. The Doi-Edwards[38] reptation model starts from considering a polymer being constrained in a tube. The boundaries of the tube are determined by the topological constraints due to the other polymers in the solution. The dynamics of the polymer are characterised by three distinctive motional regimes. Firstly, at the shortest time scale, there is segmental motion of the polymer chain where the constraints of the other polymers are not felt (ie. chain segments do not come into contact with the tube wall). Secondly, there is motion of the polymer chain along the curvilinear con-

tour of the tube, a process known as reptation (see Fig. 2.8) and thirdly there is motion in which there is complete dissociation of the polymer with its initial tube constraints. The last process is known as tube disengagement. All three motions have an associated characteristic scaling time, namely: τ_e, denoting the onset of the effect of tube constraints, τ_R, describing reptation with curvilinear diffusion and τ_d, dynamics governed by disengagement processes. These times depend on molar mass, M, in the following manner: $\tau_e \sim M^0$, $\tau_R \sim M^2$, $\tau_d \sim M^3$.

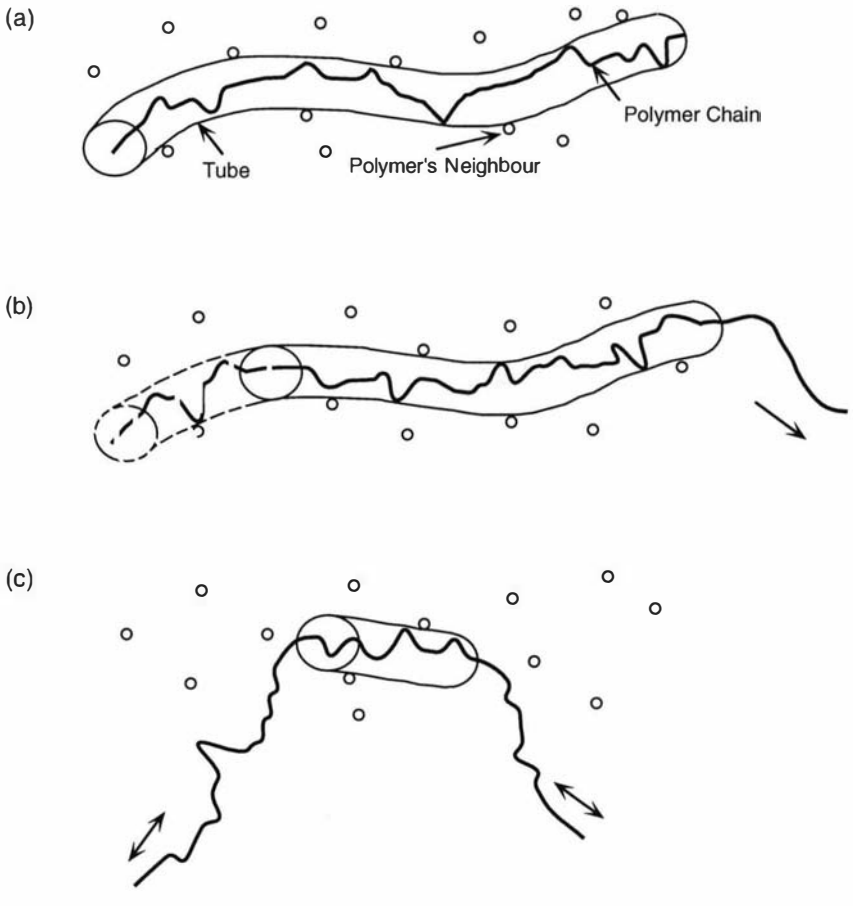

Figure 2.8: Four successive stages of tube loss for a reptating chain. (a) The initial conformation of the primitive chain and tube, (b) as the chain moves to the right it leaves the original tube boundary. Further movement, (c), leaves only a fraction of the chain in the original tube.

The constitutive equation for semi-dilute solutions and polymer melts, arising from the reptation model, predicts that when the shear rate becomes very high

($\dot{\gamma} \gg {\tau_d}^{-1}$) the viscosity has the following dependence[39]:

$$\eta(\dot{\gamma}) \simeq \eta(0)(\dot{\gamma}\tau_d)^{-3/2} \tag{2.27}$$

This relationship suggests that the shear stress will decrease with increasing strain rate. However if the polymer has a broad molecular weight distribution, the spectrum of τ_d is broad and the effect is to reduce the magnitude of the exponent in equation (2.27). Hence the predicted reduction in shear stress may disappear. The broadening behavior may explain the experimental elusiveness of the shear reduction, as many high molecular weight systems cannot avoid polydispersity.

Eqn. (2.27) is, strictly, derived under the shear conditions: $1/\tau_d \ll \dot{\gamma} \ll 1/\tau_R$. If the shear rate approaches $1/\tau_R$ it is predicted that the shear stress will again increase. The predicted stress minimum will not be observed unless the ratio of $\frac{\tau_d}{\tau_R}$, which is related to the molecular weight of the polymer, is large. This condition is often not met in experiments and stable flow is usually observed. However, if a system is monodisperse and $\frac{\tau_d}{\tau_R}$ is large enough the flow curve may contain a minimum. Such unusual constitutive behavior may lead to spurt of a fluid once a critical stress, σ_c, is exceeded (refer to figure 2.5).

2.4.4 Wormlike Surfactants

Some ionic and anionic surfactant systems, especially systems containing positive headgroups, form complex, clear gels with strong elastic properties[40]. With dilute concentrations, the cationic systems do not contain enough material to form three dimensional structures. Instead, the mixture forms rodlike micelles and is dominated by the processes described above (section 2.4.1). During flow, however, the collision rate between the micelle aggregates is increased resulting in the formation of a supermolecular structure. The processes which govern the production of such a structure can be explained in terms of the simple kinetic model that accounts for the flow-induced aggregation of rodlike micelles[41].

At higher concentrations, the supermolecule is formed in a non-transient state. Because of the polymer-like nature of the molecule, it is sometimes referred to as 'wormlike', the length of the 'worm' being concentration dependent. Wormlike micelles exhibit strong non-linear behavior[4, 42] but with a narrow distribution of relaxation times. This behavior has been suggested as being due to the aggregates breakdown when sheared above a critical shear rate. The micelle provides an ideal example for the ideal Maxwell model system described in section 2.1.2.1.

A wormlike micelle, consisting of a mixture of cetylpyridinium chloride and sodium salicylate, is to be studied in this thesis. Rheological properties of the aggregate have been studied[4], including time-dependent shear stress and oscillatory measurements.

Chapter 3

Nuclear Magnetic Resonance (NMR)

3.1 Basic Theory of NMR

The resonant behavior of nuclei placed in a magnetic field was discovered independently by two groups in 1945, namely; Bloch et al[43] and Purcell et al[44]. A description of the various interactions of magnetic resonance can be explained both quantum mechanically and semi-classically.

3.1.1 Quantum Description

The interaction of an atomic nucleus placed in a magnetic field can be described in terms of its intrinsic total angular momentum, **I** and magnetic moment, μ;

$$\mu = \gamma \hbar \mathbf{I} \tag{3.1}$$

The constant γ is called the gyromagnetic ratio and for protons has the value of 2.67×10^8 s^{-1} T^{-1}. In quantum mechanics, both μ and **I** are treated as operators and $\hbar$ is Planck's constant divided by 2π. **I** is known as the spin angular momentum operator. Closely related to the angular momentum operator, **I** is the angular momentum quantum number, I, whose value is a half-integer or whole-integer and is specific to the nucleus' characteristic symmetry. For example, a ^{1}H hydrogen (proton) or ^{13}C nucleus has $I = \frac{1}{2}$, whereas a ^{2}H deuterium nucleus has $I = 1$.

Operators for each cartesian component of the angular momentum can be defined as I_x, I_y and I_z respectively. Note that these operators do not commute. The state, $|\Psi\rangle$, of the nuclei in the magnetic field, will be described in terms of the component of the angular momentum along the z-axis. Associated with these states are corresponding eigen values, m, which can have values ranging from

eigenvalues

$I, (I-1), ..., -I$. For example the hydrogen nucleus, where $I = \frac{1}{2}$, can have the values $m = -\frac{1}{2}$ or $m = \frac{1}{2}$. Therefore the magnetic moment can be determined from the well known angular momentum operators in Eqn. (3.1) as the following:

$$\mu_z = \gamma \hbar I_z \tag{3.2}$$

In quantum mechanics the general state, $|\Psi\rangle$, of a nucleus can be expressed as a linear combination of the basis states, $|m\rangle$, thus:

$$|\Psi\rangle = \sum_m a_m |m\rangle \tag{3.3}$$

where a_m represents the complex amplitude of the basis state $|m\rangle$ present in $|\Psi\rangle$.

If a nucleus is placed in a magnetic field, then the magnetic moment interacts with the field with each basis state $|m\rangle$ having a different energy level. This splitting is known as the *Zeeman* interaction. The interaction energy for a magnetic moment μ in a magnetic field $\mathbf{B}$ is $-\mu \cdot \mathbf{B}$. From Eqn. (3.2) the Hamiltonian for the case of a field having magnitude, B_o, oriented along the z-axis is:

$$\mathcal{H} = -\gamma \hbar B_o I_z \tag{3.4}$$

The energy levels of this Hamiltonian are related to the eigenvalues, m as follows:

$$E_m = -\gamma \hbar B_o m \tag{3.5}$$

An example of the discrete energy levels for a proton ($I = \frac{1}{2}$) is shown in figure 3.1.

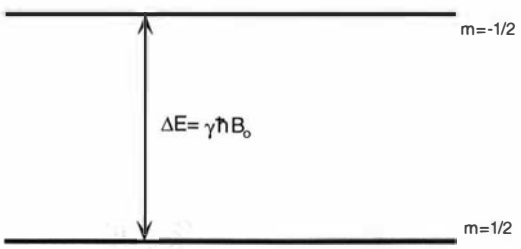

Figure 3.1: The *Zeeman* energy splitting of a proton, when subjected to a magnetic field, is determined by the two discrete energy states the nucleus can acquire. The two possibilities are inherent to the spin having an angular momentum quantum number of $\frac{1}{2}$.

The nuclear states' time dependence is described by the Schrödinger equation using the Hamiltonian from Eqn. (3.4):

$$i\hbar \frac{\partial}{\partial t}[|\Psi\rangle] = \mathcal{H}|\Psi(0)\rangle \tag{3.6}$$

An alternative form of this equation is:

$$|\Psi(t)\rangle = U(t)|\Psi(0)\rangle \tag{3.7}$$

where $U(t)$ is the evolution operator. Note that the time dependence is inherently expressed within the evolution operator and the states are 'stationary'. As the Hamiltonian in Eqn. (3.4) is time independent one can express the evolution operator as:

$$U(t) = e^{i\gamma B_o I_z t} \tag{3.8}$$

The exponential operator is analogous to well known rule used in geometric transformations, namely:

$$R_z(\phi) = e^{i\phi I_z} \tag{3.9}$$

where $R_z(\phi)$ corresponds to a rotation of ϕ degrees about the z axis. Indeed this similarity suggests that in a magnetic field, states $|m\rangle$ precess about the z axis at a frequency of ω_o where

$$\omega_o = \gamma B_o \tag{3.10}$$

This precessional frequency is known as the Larmor frequency and is a fundamental equation in NMR.

3.1.1.1 Excitation and the Rotating Frame

Detection of the spins' precession requires the nuclear states to be excited. Keeping in line with the quantum description given here, the excitation would involve the absorption of energy equal to the transition between the energy levels, namely:

$$\Delta E = \hbar\omega = \gamma\hbar B_o \tag{3.11}$$

Such an energy source could be an oscillating magnetic field, B_1, transverse to B_o, with frequency ω. This field can be described as the combination of two fields of magnitude, B_1, rotating counter clock-wise as shown in figure 3.2. With the application of this B_1 field the Hamiltonian for the nuclear states, in the laboratory frame, is now:

$$\mathcal{H} = -\gamma\hbar B_o I_z - 2\gamma\hbar B_1 \cos\omega t I_x \tag{3.12}$$

The effect of one of the B_1 field components on the spin states can be ignored as it is rotating in the opposite sense to the spin states, effectively at a frequency of 2ω, and the magnitude of the component, $B_1 \ll B_o$.

It is helpful to change our frame of reference to one where B_1 is stationary. This change is required to eliminate the time dependence of the Hamiltonian thus allowing the use of the simple evolution operator of Eqn. (3.8). This change of

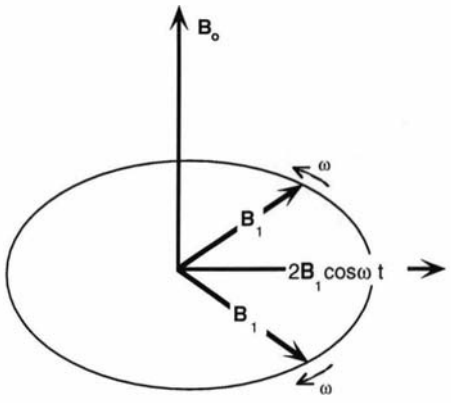

Figure 3.2: The applied transverse magnetic field, B_1, can be described as a combination of two fields rotating counter-clockwise. This description is the basis of the rotating frame description.

reference is a useful tool and will be used later when describing the spin states with a 'classical picture'. Thus in the rotating frame the Hamiltonian in Eqn. (3.12) is now:

$$\mathcal{H} = -\gamma\hbar(B_o - \frac{\omega}{\gamma})I_z - \gamma\hbar B_1 I_x \tag{3.13}$$

Eqn. (3.13) suggests if an oscillating magnetic field is applied, transverse to the field B_o with ω equaling the Larmor frequency, ω_o, the longitudinal field vanishes. This leaves the effective field along the rotating frame x-axis. Thus precession of the spin states is now about this axis, a process known as *nuclear magnetic resonance*.

Of course the measurements made within NMR are obtained not for one nucleus but for a number of nuclei. Thus this measurement requires an ensemble average approach.

3.1.1.2 Ensemble Averaging of the Nuclear States

The measurement of the component of angular momentum, m, of a nucleus in state $|m\rangle$ can be determined by calculating $\langle m|I_z|m\rangle$. According to Eqn. (3.3) a nucleus in some state $|\Psi\rangle$ would involve the multiplication:

$$\begin{aligned}\langle\Psi|I_z|\Psi\rangle &= \sum_{m,m'} a_m a^*_{m'}\langle m'|I_z|m\rangle \\ &= \sum_{m,m'} a_m a^*_{m'} m\langle m'|m\rangle\end{aligned}$$

$$= \sum_m |a_m|^2 m \tag{3.14}$$

if the states $|m\rangle$ and $|m'\rangle$ are orthogonal. The value $|a_m|^2$ represents the normalised probability that the the state will be found in state $|m\rangle$. Thus the 'expectation value' of a large number of nuclei in the same state, $|\Psi\rangle$, is the mean value of the eigen values weighted by $|a_m|^2$. In contrast to this, measurements made within NMR may involve states which are not identical and require an *ensemble average* calculation over sub-ensembles, with associated classical probability, p_Ψ:

$$\overline{\langle\Psi|I_z|\Psi\rangle} = \sum_\Psi p_\Psi \langle\Psi|I_z|\Psi\rangle \tag{3.15}$$

It is convenient at this point to define the states for a nuclei of $I = \frac{1}{2}$, namely:

$$\begin{aligned} |\tfrac{1}{2}\rangle &= \begin{bmatrix} 1 \\ 0 \end{bmatrix} \\ |-\tfrac{1}{2}\rangle &= \begin{bmatrix} 0 \\ 1 \end{bmatrix} \end{aligned} \tag{3.16}$$

Therefore the angular momentum operator can be calculated as:

$$I_z = \frac{1}{2}\begin{bmatrix} 1 & 0 \\ 0 & -1 \end{bmatrix} \tag{3.17}$$

From Eqn. (3.3) the state of the nuclei can be expressed as an admixture of the individual states:

$$|\Psi\rangle = a_{\frac{1}{2}}\begin{bmatrix} 1 \\ 0 \end{bmatrix} + a_{-\frac{1}{2}}\begin{bmatrix} 0 \\ 1 \end{bmatrix} \tag{3.18}$$

Finally using Eqn. (3.15) the ensemble average can be calculated for the spin $\frac{1}{2}$ nuclei as:

$$\overline{\langle\Psi|I_z|\Psi\rangle} = \frac{1}{2}\left(\overline{|a_{\frac{1}{2}}|^2} - \overline{|a_{-\frac{1}{2}}|^2}\right) \tag{3.19}$$

Eqn. (3.19) may be interpreted as that the expectation value of I_z is determined by the difference in population between the upper and lower energy levels. The Boltzman distribution describes the thermal equilibrium population of a state $\begin{bmatrix} 1 \\ 0 \end{bmatrix}$ or $\begin{bmatrix} 0 \\ 1 \end{bmatrix}$, separated by energy $\hbar\gamma B_o$. This distribution can be used to calculate the mean probabilities as:

$$\overline{\left|a_{\pm\frac{1}{2}}\right|^2} = \frac{e^{\pm\hbar\gamma B_o/2k_BT}}{e^{\hbar\gamma B_o/2k_BT} + e^{-\hbar\gamma B_o/2k_BT}} \tag{3.20}$$

where k_B is Boltzman's constant and T is the equilibrium temperature of the nuclei' surroundings measured in units of Kelvin. At room temperature, the ratio

$\hbar\gamma B_o/2k_BT$, for a typical magnet used in NMR, has the value on the order of $\frac{1}{5}$. Because of this magnitude and using the series expansion of an exponential, Eqn. (3.20) can be simplified as:

$$\overline{\left|a_{\pm\frac{1}{2}}\right|^2} = \frac{1}{2}(1 \pm \hbar\gamma B_o/2k_BT) \tag{3.21}$$

Eqn. (3.21) is an important result as it suggests that there is a slightly higher number of nuclei in the lower energy level. This asymmetry is very important as the resultant magnetisation component $M_z = M_o$, is available to be observed during the NMR process. The ability to use the magnetisation vector is peculiar to ensembles of non-interacting spin $\frac{1}{2}$ nuclei and will be employed in the thesis where proton NMR is used exclusively.

3.1.2 Semi-Classical Description

As discussed in the last section, an ensemble of spins, for $I = \frac{1}{2}$, placed in a magnetic field, $\mathbf{B}$, can be described in terms of a two dimensional magnetisation vector, $\mathbf{M}$. $\mathbf{M}$ undergoes a torque produced by the external field, in which a change of angular momentum must occur in accordance with Newton's second law. Hence the change in the magnetisation vector $\mathbf{M}$ can be equated to the torque as seen:

$$\frac{\partial \mathbf{M}}{\partial t} = \gamma(\mathbf{M} \times \mathbf{B}) \tag{3.22}$$

The solution to equation (3.22) yields the precession of the magnetisation vector about the external field's direction at a rate, $\omega_o = \gamma B_o$, where $\mathbf{B} = B_o\mathbf{k}$.

3.1.2.1 Excitation

The application of another oscillating field B_1, transverse to B_o at the same Larmor frequency, again can be represented by the component of B_1 rotating in the same sense as $\mathbf{M}$, namely:

$$\mathbf{B}_1 = B_1(\cos\omega_o t\mathbf{i} + \sin\omega_o t\mathbf{j}) \tag{3.23}$$

where $\mathbf{i}$, $\mathbf{j}$ and $\mathbf{k}$ are the unit vectors aligned along the x, y and z axes respectively. Thus each component of Eqn. (3.22) can be expressed as:

$$\begin{aligned}
\frac{\partial M_x}{\partial t} &= \gamma(M_yB_o + M_zB_1\sin\omega_o t) \\
\frac{\partial M_y}{\partial t} &= \gamma(M_zB_1\cos\omega_o t - M_xB_o) \\
\frac{\partial M_z}{\partial t} &= \gamma(-M_xB_1\sin\omega_o t - M_yB_1\cos\omega_o t)
\end{aligned} \tag{3.24}$$

With the initial magnetisation being aligned with the z-axis, ie. $\mathbf{M}(0) = M_o\mathbf{k}$ the solution to Eqns. (3.24) are:

$$\begin{aligned} M_x &= M_o \sin\omega_1 t \sin\omega_o t \\ M_y &= M_o \sin\omega_1 t \cos\omega_o t \\ M_z &= M_o \cos\omega_1 t \end{aligned} \tag{3.25}$$

These equations represent a complicated motion of precession about $\mathbf{B}_o$, at frequency ω_o, and about $\mathbf{B}_1$, at frequency ω_1, simultaneously (see Fig. 3.3). As in the previous quantum mechanical description of NMR, a transformation to a frame of reference rotating with B_1 about z with frequency ω_o is required. This change leads to equations (3.25) becoming:

$$\begin{aligned} M_x &= 0 \\ M_y &= M_o \sin\omega_1 t \\ M_z &= M_o \cos\omega_1 t \end{aligned} \tag{3.26}$$

In the frame of the rotating field B_1, the previous complicated evolution becomes a simple rotation about the direction of B_1 by an angle $\omega_1\Delta t$, where Δt is time the oscillating field is applied. Hence different angles of rotation are possible by simply varying the time of application of the oscillating field B_1.

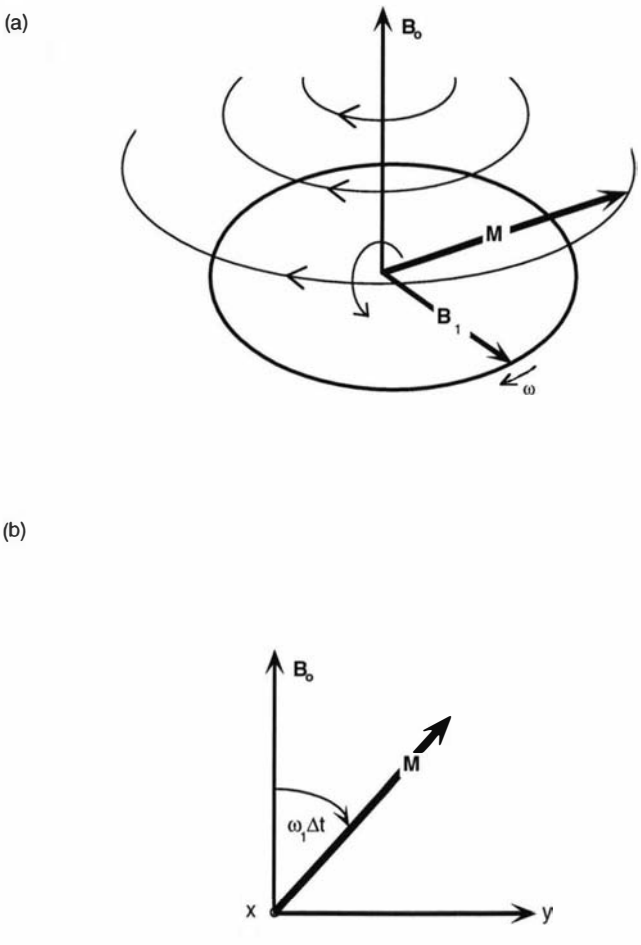

Figure 3.3: (a) Excitation of the nuclei produces simultaneous precession of the proton's magnetisation vector about the main field, B_o and applied oscillating field, B_1. (b) By changing the frame of reference to a rotation about B_o, at frequency ω_o, the complicated motion becomes a simple rotation about the x-axis.

3.1.3 Relaxation

After the application of the r.f. magnetic pulse, the spins will eventually return to thermal equilibrium with their surroundings. This process is known as spin-lattice relaxation and involves the spins transferring their energy to the surrounding lattice. To a very good approximation, spin lattice relaxation involves an experimental restoration of equilibrium magnetisation. For example , following inversion of the magnetisation at time $t = 0$, the M_z component evolves as:

$$M_z(t) = M_o(1 - 2e^{-\frac{t}{T_1}}) \tag{3.27}$$

The time constant T_1 is known as the spin-lattice relaxation time and is typically in the range of 0.1 to 10 seconds for protons at room temperature. The origin of this relaxation is predominantly reorientational fluctuations of inter-proton dipolar interaction. A characteristic correlation time, τ_c, for dipolar fluctuations separates regimes of slow and fast motion (see Fig. 3.4). A T_1 minimum is observed when the Larmor frequency is equal to the correlation frequency ie. $\omega_o\tau_c = 1$. If the dipoles are mobile and fluctuating very fast, the correlation time will be small. This mobile regime is known as extreme narrowing.

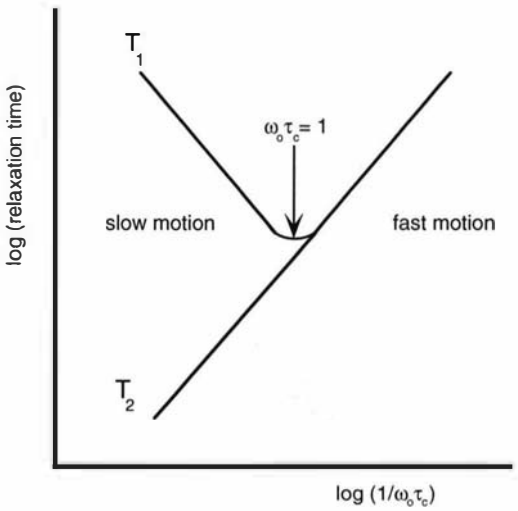

Figure 3.4: Fast and slow motional regimes for dipolar fluctuations are separated by a T_1 minimum.

The process of relaxation to thermal equilibrium between spins, not surprisingly, is referred to as spin-spin relaxation. This process is characterised by the

time constant, T_2. Energy transfer from spin to spin, indirectly via the lattice, contributes to this type of relaxation along with direct spin-spin processes. This leads to the result that $T_2 \leq T_1$. By contrast with the spin-lattice process, spin-spin relaxation is dominated by phase relationships *between* spins and leads to an exponential decay of the transverse magnetisation (see Eqn. 3.28). T_2 times are in the range of 10 μs to 10 s. Given a starting transverse magnetisation $M_{x,y}(0)$;

$$M_{x,y}(t) = M_{x,y}(0)e^{-\frac{t}{T_2}} \tag{3.28}$$

The Anderson-Weiss[45] treatment for relaxation treats the fluctuating dipolar fields via a time dependent frequency, offset from the average longitudinal field precession frequency ω_o. The ensemble mean square average of this frequency fluctuation is $\overline{\Delta\omega^2}$. For the extreme narrowing regime the relationship between T_2 and correlation time τ_c, is the following:

$$\frac{1}{T_2} = \overline{\Delta\omega^2}\tau_c \tag{3.29}$$

Thus for rotationally mobile dipoles, long T_2 times are expected while a short relaxation time suggests a lack of mobility. The time constants T_1 and T_2 can become significantly different when interaction between spins fluctuate very slowly, as they do in solids (see Fig. 3.4).

3.1.4 Chemical Shift

The electron environment of a nucleus will effect its angular momentum thus shifting its resonant frequency. The shift is strongly dependent on which nuclei one is dealing with but typical values are a few ppm[1] for protons. Unlike direct dipole interactions, spherical terms in the chemical shift Hamiltonian are not zero. Thus even under rapid rotational tumbling of nuclei, characteristic of liquids, the chemical shift is still evident. Important information concerning chemical environment is thus available for both solid and liquid samples.

3.1.5 Signal Detection

An rf coil placed around the sample is responsible for both excitation and detection of the nuclei. Excitation may involve a 90° rf pulse. According to the discussion on page 27, this would require a pulse of duration $\Delta t = \frac{\pi}{2\gamma B_1}$ and frequency ω_o. An oscillatory voltage, typically μV, would then be induced across the coil, produced from the precession of the nuclei after r.f. excitation. By mixing this signal with two reference signals, one 90° out of phase (a process known as

[1] ppm $\equiv$ Parts per million.

heterodyning), both in-phase and quadrature signals can be detected. Using the terminology of the semi-classical description employed earlier, this type of signal detection essentially measures M_x and M_y magnetisations. If $\mathrm{M}(t)$ represents the macroscopic magnetisation at time t then the detection could be expressed as:

$$\begin{aligned} \mathrm{M}(t) &= M_o[\mathbf{i}\cos\omega_o t + \mathbf{j}\sin\omega_o t]e^{-\frac{t}{T_2}} \\ &= M_o e^{i\omega_o t}e^{-\frac{t}{T_2}} \end{aligned} \tag{3.30}$$

where $\mathbf{i}$ and $\mathbf{j}$ are the unit vectors in the x and y directions respectively. We choose an alternative complex number representation in which the real and imaginary components represent M_x and M_y, hence the commonly used terms *real and imaginary* signals. The signal is oscillatory, decaying and induced by the free precession. Thus the signal is known as the *free induction decay* or FID. Shown in figure 3.5 are the Fourier transform of the complex signals giving both real (*absorption*) and imaginary (*dispersion*) frequency spectra.

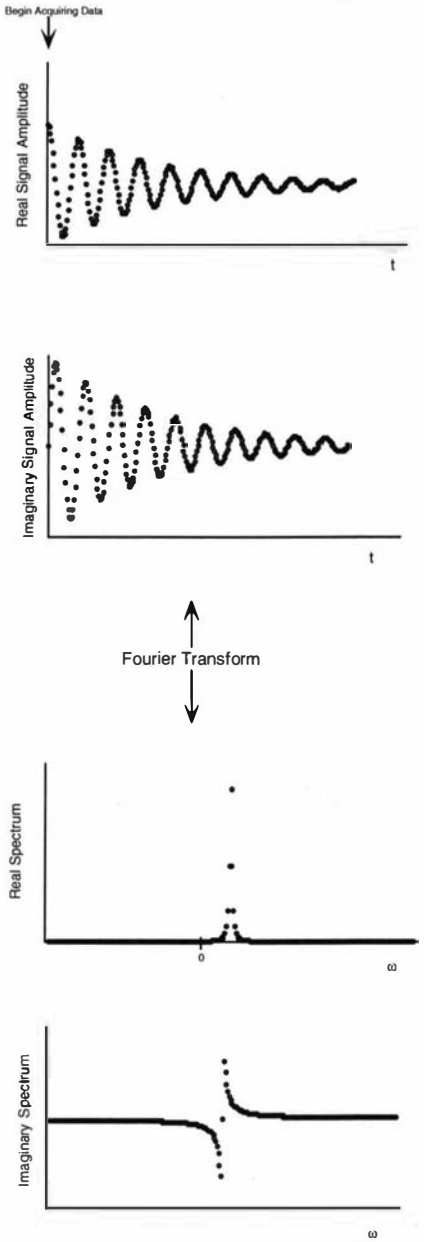

Figure 3.5: The relaxation of the transverse magnetisation of the nuclei is observed after the 90° excitation pulse. The example shown demonstrates an experiment occurring 'off resonance'.

3.2 NMR Microscopy

NMR microscopy involves the spatial encoding of spins using magnetic field gradients.

3.2.1 Gradients

If the magnetic field is varied across the sample, nuclei will experience precessional frequencies dependent upon their position. A linear field variation, or *gradient*, allows simple spatial encoding of the nuclei via frequency or phase encoding. These gradients are usually applied as pulses from independent gradient coil sets and the resulting fields (in the direction of B_o) are superimposed on B_o. To enable only nuclei in a selected region to be excited, for instance in a slice, frequency selection is essential. This frequency selection is produced by the application of a time modulated rf excitation pulse in conjunction with simultaneously applied gradients.

3.2.2 Spatial Encoding

The spatial dependence of the frequency described above, is a result of the linear variation of a magnetic field in addition to the polarizing field amplitude, B_o. Thus the Larmor frequency can now be defined as:

$$\omega(\mathbf{r}) = \gamma B_o + \gamma \mathbf{G} \cdot \mathbf{r} \tag{3.31}$$

where $\mathbf{G}$ is the **grad** of the pulsed gradient field component parallel to $\mathbf{B_o}$ and $\mathbf{r}$ is the coordinates of the nuclear spin. The frequency distribution described above is at the foundation of the imaging of nuclei. Methods of reconstructing an image are numerous[46]– [54]. We will concentrate on one method in particular known as 'spin warp' or *Fourier imaging.*

3.2.2.1 Spin Density and k-Space

To enable the reconstruction of an NMR image, one must be able to 'map' the local density of the nuclear spins. We will define this density parameter as $\rho(\mathbf{r})$. If we consider a small volume, dV, of spins emitting a signal, dS, according to Eqn. (3.30), the magnitude of this signal will be:

$$dS \propto \rho(\mathbf{r}) dV e^{i\omega(\mathbf{r})t} \tag{3.32}$$

$$= \rho(\mathbf{r}) dV e^{i(\gamma B_o + \gamma \mathbf{G}\cdot\mathbf{r})t} \tag{3.33}$$

simplifying the proportionality to an equality. Notice that the above equation does not take into account the effects of relaxation mentioned in section 3.1.3. This

absence is allowable providing the phase spread of the transverse magnetisation due to the applied gradient, $\gamma \mathbf{G} \cdot \mathbf{r}t$, is larger than the phase spread due to T_2. As a result of the heterodyning process, described on page 31, the term, γB_o, can be eliminated if a similar reference frequency is chosen. With this mixing the signal only oscillates with frequency $\gamma \mathbf{G} \cdot \mathbf{r}$. Thus the overall signal obtained from a sample is given by:

$$S(t) = \int\int\int \rho(\mathbf{r}) e^{i\gamma \mathbf{G} \cdot \mathbf{r}t} d\mathbf{r} \tag{3.34}$$

where the integral is taken over volume, $d\mathbf{r}$. The above equation can be simplified more with the introduction of a vector, $\mathbf{k} = \frac{\gamma \mathbf{G} t}{2\pi}$. The vector has the units of reciprocal space. Eqn. (3.34) becomes:

$$S(\mathbf{k}) = \int\int\int \rho(\mathbf{r}) e^{i2\pi \mathbf{k} \cdot \mathbf{r}} d\mathbf{r} \tag{3.35}$$

At first glance one may recognise Eqn. (3.35) as a *Fourier* relation. The associated inverse Fourier transform is thus:

$$\rho(\mathbf{r}) = \int\int\int S(\mathbf{k}) e^{-i2\pi \mathbf{k} \cdot \mathbf{r}} d\mathbf{k} \tag{3.36}$$

Eqns. (3.35) and (3.36) show that $S(\mathbf{k})$ and $\rho(\mathbf{r})$ are conjugate to each other. This relation is fundamental in NMR imaging. **k**-space can be 'mapped' by sampling the signal at different time intervals. Thus $S(\mathbf{k})$ is collected in the time domain and $\rho(\mathbf{r})$ is defined in the frequency domain.

In practice **k**-space can be traversed in a variety of ways, including the method of *filtered back projection*[55]–[58] and *Fourier Imaging*. Only the latter will be discussed in any detail where inverse space is mapped with a cartesian coordinate system.

3.2.2.2 Fourier Imaging

As described in the previous section, Fourier imaging (FI) consists of the cartesian mapping of **k**-space. This is achieved by sampling of the FID during the application of a gradient, G_x. A typical pulse sequence is shown in figure 3.6 where we have aligned the 'read' gradient along the x-axis. A gradient applied outside the time interval associated with the FID collection is known as the 'phase' gradient, named so because of the phase modulation it imparts on the signal. Thus the signal obtained from this type of spatial encoding can be expressed[59, 60]:

$$S(k_x, k_y) = \int_{-\frac{a}{2}}^{\frac{a}{2}} \left[\int_{-\infty}^{\infty} \int_{-\infty}^{\infty} \rho(x, y, z) e^{i2\pi(k_x x + k_y y)} dx dy \right] dz \tag{3.37}$$

where a is the slice thickness aligned along the z-axis. Assuming a homogeneous distribution of nuclei within the slice, the outer integral can be ignored as it

represents an averaging process. Thus Eqn. (3.37) becomes:

$$S(k_x, k_y) = \int_{-\infty}^{\infty} \int_{-\infty}^{\infty} \rho(x, y) e^{i2\pi(k_x x + k_y y)} dx dy \tag{3.38}$$

Eqn. (3.38) shows a two dimensional Fourier transform of the spin area density, $\rho(x, y)$, the reconstruction of which is obtained again by the inverse Fourier transform:

$$\rho(x, y) = \int_{-\infty}^{\infty} \int_{-\infty}^{\infty} S(k_x, k_y) e^{-i2\pi(k_x x + k_y y)} dk_x dk_y \tag{3.39}$$

Both the reconstruction of $\rho(x, y)$ and collection of $S(k_x, k_y)$ are achieved by computer. The components k_x and k_y are given by $\frac{\gamma G_x t_x}{2\pi}$ and $\frac{\gamma G_y t_y}{2\pi}$ respectively. The time coordinates, which are usually of different duration, are associated with the application of the respective gradients. The process of sampling **k**-space along the x-axis is achieved by a fixed read gradient and then repeated for successively increased values of k_y.

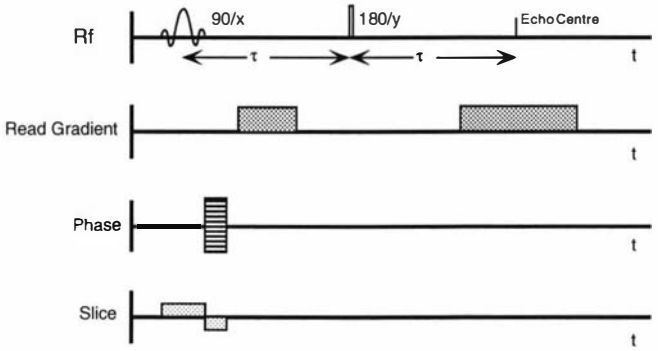

Figure 3.6: The Fourier imaging pulse sequence described consists of a spin echo with the characteristic phase gradient applied before the read gradient. The inversion of the slice gradient is to rephase the spins which have acquired a phase shift during rf modulation.

The 180° rf pulse shown in figure 3.6 inverts the precession of the spins thus reversing the dephasing of the ensemble. If the inversion pulse is applied after time, τ, after the excitation pulse, then the rephasing of the spins is expected at time, 2τ, after the 90° pulse. Thus this type of spin manipulation is known as a *spin echo*. There are several reasons for wanting to use such a pulse sequence. One advantage is the sampling of the *complete* echo as opposed to the top of the FID (see figure 3.5) resulting in the data being acquired in the time domain for both negative and positive times. This fact, along with the use of positive and negative phase gradients, allow the four quadrants of inverse space to be sampled.

A second advantage is the ability to use the spin echo to encode for motion of the spins as well as their positions.

3.2.3 Encoding for Motion

The spin echo pulse sequence described in the previous section can be used to determine a spin's motion by applying a pair of gradients, each having amplitude, g, and duration, δ, before and after the 180° rf pulse. This process, known as *pulsed gradient spin echo* (PGSE)[61], effectively 'tags' the spins by means of phase. Any movement of the nuclei within the time, Δ (see Fig 3.7), will result in a *local* phase shift after the refocussing of the spin echo. This phase shift will be proportional to the displacement of the local spins over time, Δ.

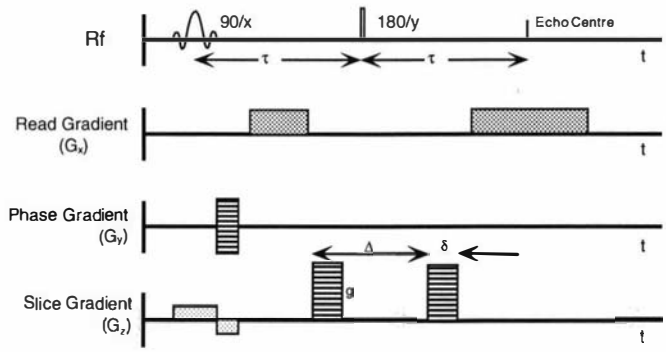

Figure 3.7: The pulsed gradient spin echo (PGSE) pulse sequence allows the spins to be labeled according to a local phase shift. This phase shift, which is proportional to the spin's displacement over time, Δ, is acquired with movement, while under the influence of a field gradient, $\mathbf{g}$.

A technique suitable for investigating the distribution of nuclear motion is q-*space imaging.*

3.2.3.1 q-Space Imaging

The first experimental demonstration and theoretical analysis for the PGSE sequence was given by Stejskal and Tanner[62]. This work led to the well known *narrow pulse approximation* ($\delta \ll \Delta$) in which the echo amplitude, E, is described as a function of $\mathbf{g}$, δ and Δ:

$$E(\mathbf{g}, \delta, \Delta) = E_o e^{-\gamma^2 \delta^2 g^2 D \Delta} \tag{3.40}$$

where D is the centre-of-mass self diffusion coefficient of the nuclei. The Stejskal-Tanner description[63] is based on the function, $P_s(\mathbf{r}|\mathbf{r}', \Delta)$, which is defined as the spatial probability distribution. This parameter describes the probability that a nucleus, initially at position $\mathbf{r}$, will have moved to position $\mathbf{r}'$ at a later time, Δ. The normalised echo amplitude, described in Eqn. (3.40), is influenced by the probability function in the following way:

$$E(\mathbf{g}, \delta, \Delta) = \int \rho(\mathbf{r}) \int P_s(\mathbf{r}|\mathbf{r}', \Delta) e^{i\gamma\delta\mathbf{g}\cdot(\mathbf{r}'-\mathbf{r})} d\mathbf{r}' d\mathbf{r} \tag{3.41}$$

which for the case of superimposed diffusion and flow leads to[64, 65]:

$$E(\mathbf{g}, \delta, \Delta) = e^{-\gamma^2\delta^2 g^2 D\Delta} e^{i\gamma\delta\mathbf{g}\cdot\mathbf{v}\Delta} \tag{3.42}$$

D is the self diffusion coefficient and $\mathbf{v}$ is the flow velocity. From Eqn. (3.42) it can be seen the echo amplitude depends upon the self-diffusion and its phase depends upon the component of the flow in the direction of the gradient, $\mathbf{g}$.

In practice, the probability function must be averaged over the ensemble characterised by the starting point, $\mathbf{r}$. Hence the 'averaged propagator' is defined as:

$$\overline{P_s}(\mathbf{R}, \Delta) = \int_{pixel} \rho(\mathbf{r}) P_s(\mathbf{r}|\mathbf{r} + \mathbf{R}, \Delta) d\mathbf{r} \tag{3.43}$$

where $\mathbf{R}$ is the dynamic displacement given by $\mathbf{r}' - \mathbf{r}$. This 'new' correlation function describes the probability that nuclei will travel a displacement, $\mathbf{R}$, over a time interval, Δ. Now Eqn. (3.41) can be written:

$$E(\mathbf{g}, \delta, \Delta) = \int \overline{P_s}(\mathbf{R}, \Delta) e^{i\gamma\delta\mathbf{g}\cdot\mathbf{R}} d\mathbf{R} \tag{3.44}$$

where the signal has been normalised, hence the absence of $\rho(\mathbf{r})$. As in section 3.2.2.1, equation (3.44) can be identified as a Fourier relation where $E(\mathbf{g}, \delta, \Delta)$ and $\overline{P_s}(\mathbf{R}, \Delta)$ are conjugate. Analogous to the definition of $\mathbf{k}$-space, a space reciprocal to the dynamic displacement, $\mathbf{R}$, is defined as[54]:

$$\mathbf{q} = \frac{\gamma\delta\mathbf{g}}{2\pi} \tag{3.45}$$

Thus Eqn. (3.44) can be written as:

$$E(\mathbf{q}, \Delta) = \int \overline{P_s}(\mathbf{R}, \Delta) e^{i2\pi\mathbf{q}\cdot\mathbf{R}} d\mathbf{R} \tag{3.46}$$

The PGSE experiment can therefore be thought of as an imaging process in which the sampling occurs in the conjugate $\mathbf{q}$ space and, upon the inverse Fourier transform, yields the image of $\overline{P_s}(\mathbf{R}, \Delta)$ in $\mathbf{R}$ space. $\mathbf{q}$-space is traversed by incrementing the gradient magnitude, g, a similar process to that observed for

k-space (see Sec. 3.2.2.1). For the finite width gradient case a more complex solution is obtainable by replacing Δ with $\Delta - \frac{\delta}{3}$ in the self diffusion exponent. For flow the exponent is unchanged.

For Brownian motion $\overline{P_s}(\mathbf{R}, \Delta)$ is a Gaussian curve centred at $\mathbf{R} = 0$, the square root of the self-diffusion coefficient is equal to the Full-Width-Half-Maximum (FWHM) of this curve, given by:

$$FWHM = \frac{2\gamma\delta g}{\pi}\sqrt{(\ln 2)D\Delta} \tag{3.47}$$

Where flow is also present the diffusive motion is superimposed on a local velocity, **v**. $\overline{P_s}(\mathbf{R}, \Delta)$ still retains its Gaussian shape but now it is centered at $\mathbf{R} = \mathbf{v}\Delta$. It is this offset which will be used throughout this thesis to calculate velocity distributions.

What has not yet been discussed is the process by which we can determine a distribution of velocities. This entails *both* spatial *and* motion encoding.

3.2.4 Combining Spatial and Motional Encoding

A typical dynamic imaging experiment, shown previously in figure 3.7, may involve an ensemble of spins undergoing Brownian *and* translational motion. Associated with each of these types of motion are the self-diffusion coefficient, D and velocity, **v** respectively. The signal obtained in the time domain will be influenced by both the PGSE gradient, **g**, and spatial gradient, **G**. The resultant signal will be modulated in both **k**- and **q**-space. These perturbations are separable and according to Eqns. (3.35) and (3.46) the signal will have the form:

$$\begin{aligned} S(\mathbf{k},\mathbf{q}) &= \int \rho(\mathbf{r}) e^{i2\pi\mathbf{k}\cdot\mathbf{r}} \int \overline{P_s}(\mathbf{R},\Delta) e^{i2\pi\mathbf{q}\cdot\mathbf{R}} d\mathbf{R} d\mathbf{r} \\ &= \int \rho(\mathbf{r}) E(\mathbf{q},\mathbf{r},\Delta) e^{i2\pi\mathbf{k}\cdot\mathbf{r}} d\mathbf{r} \end{aligned} \tag{3.48}$$

Eqn. (3.48) states that image reconstruction in **k**-space will yield $\rho(\mathbf{r})E(\mathbf{q},\mathbf{r},\Delta)$. One must remember that $\overline{P_s}(\mathbf{R}, \Delta)$ is inherently normalised and thus $E(0,\mathbf{r},\Delta)$ is unity. This is an important result as it allows the reconstruction of the spin density map when the PGSE gradient is zero. This implies that $E(\mathbf{q},\mathbf{r},\Delta)$ is separately obtainable from $\rho(\mathbf{r})$ by normalising to the zero **q** image.

Summarising, a signal consisting of modulations caused by both position and motion can be reconstructed into spatial images with each pixel in that image having a characteristic phase modulation which arises from the spin's displacement over time, Δ. The phase modulation is proportional to **g** which is incremented from an amplitude of $0 \rightarrow g_{max}$. Therefore, if a series of images are generated modulated with increasing **q**, an inverse Fourier transform with respect to **q**,

returns the averaged propagator. Thus the experiment is three dimensional, with two spatial dimensions and one motion dimension.

In most of the experiments performed in this thesis the average propagator will be influenced by both flow *and* diffusion. It will thus consist of a gaussian whose width is determined by Eqn. (3.47) and whose displacement from the origin will give a measure of the averaged velocity in that pixel.

3.3 Software and Hardware used in NMR

3.3.1 Imageshow

Imageshow is a software package designed principally by Y. Xia and A. Coy[2] and used at Massey University. The source code is written in Pascal and has been created to operate on Macintosh computers. Full detail of the software can be found elsewhere[66] as only a brief description of the software's specifications will be given here.

Imageshow is an image processing and displaying tool. Image dimensions from 64×64 pixels to 256×256 pixels, can be processed. As well as many other arithmetic processes such as addition and subtraction of images, the software is capable of handling sets of multiple 2-D (ie. 3-D sets) in order to calculate parameters associated with the third dimension. In particular it is possible to Fourier analyse this dimension so as to obtain the averaged propagator in the **q** direction (see page 37), with 256-1024 point resolution.

A typical 3-D velocity data set is shown in figure 3.8 where both real and imaginary **q**-slices are shown. The associated velocity and diffusion maps are also shown. Because of time constraints it is usual to only collect on the order of 8-16 **q**-slices.

In practice, for velocity mapping, it is convenient to obtain the 2-D spatial FFT using the computer in the spectrometer unit. After this has been completed the real and imaginary frequency domain data is transferred to the Macintosh computer for a final inverse **q** FFT. For various reasons more than one spectrometer was used in this thesis. An explanation of this follows.

3.3.2 Spectrometers

Three spectrometer-magnet systems were used throughout this thesis. One of these consisted of a JEOL FX60 spectrometer with a water-cooled electromagnet, the proton resonant frequency of which was 60 MHz (1.5 T). This system was used

[2] Previous PhD students in the Physics Department at Massey University.

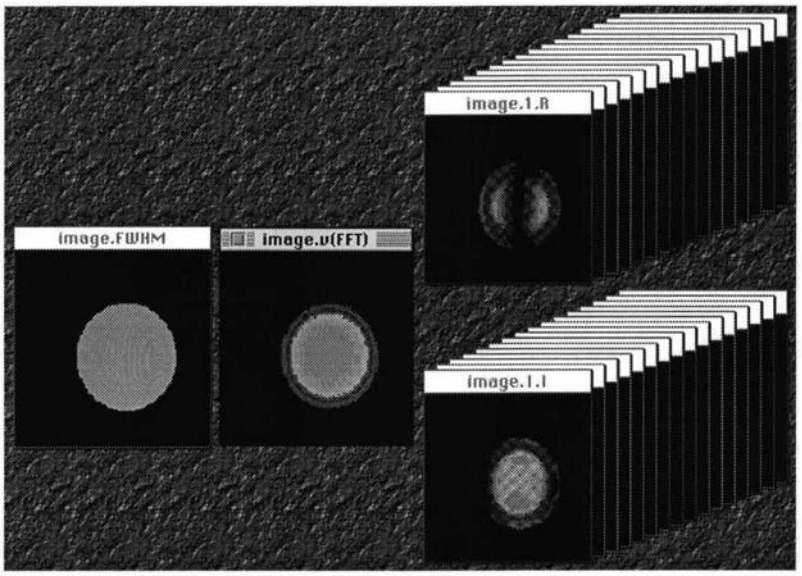

Figure 3.8: The 3-D data set shows a series of proton images of flowing water through a capillary tube. The phase modulation apparent in these images is due to the evolution of the spins in q-space where an incremented gradient **g** is applied. An FFT wrt **q** reveals both the diffusion and velocity in the direction of **g**.

principally for diffusion measurements along with a study of velocity distributions within a cylindrical-Couette geometry (see section 3.4.2).

The experiments completed on this system coincided with the purchase of a super-conducting vertical bore magnet and Bruker AMX spectrometer. A larger proton resonant frequency of 300 MHz (7.05 T) was available. This system was used to determine velocity distributions in a variety of geometries including capillary flow through tubes. Both of the above spectrometers are located at Massey University, NMR laboratory, Palmerston North, New Zealand.

The third spectrometer was an earlier version of the Bruker AMX; the Bruker AM. The magnet used with this spectrometer provided a proton resonant frequency of 200 MHz (4.70 T). The work was a collaborative project with the Royal Dutch Shell Laboratories in Amsterdam, The Netherlands and involved a relaxation study of polyolefin mobility. These experiments were carried out by the author during a period of ten months at the Dutch laboratories.

3.4 Rheometers

A discussion of the various rheometers used in this thesis follows. Included in this are the general features of each type of rheometer, ie. detection scheme, geometry

etc., as well as a detailed analysis of design for each specific magnet described in the previous section.

3.4.1 The Capillary Rheometer

The standard data obtained from a capillary rheometer, of known length and diameter, is the pressure drop at a known flow rate. From this data the apparent viscosity can be determined as a function of apparent shear rate. The local shear rate which varies across the tube is not usually determined. End effects, sometimes very prominent, are also usually 'Bagley' corrected[1]. A capillary rheometer has

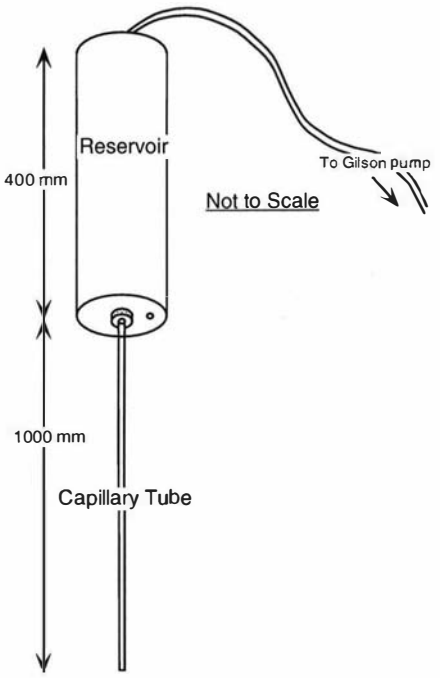

Figure 3.9: The capillary rheometer produces a variable shear rate across the capillary tube as well as having to be 'Bagley' corrected for entrance and exit effects.

been designed to measuring the velocity profile of some non-Newtonian polymeric systems across a capillary tube. The rheometer consisted of three different diameter tubes, of length 1.0 m (see Fig. 3.9), attached to a tubular reservoir via a swage-lock system. The five inner and outer diameters were: 1.5, 2.6, 3.4, 3.9, 5.0 ± 0.1 mm ID, 3.5, 4.2, 5.1, 6.6, 7.5 ± 0.1 mm OD. Rheometer measurements consisted of accurate velocity profiles obtained across the diameter of the capillary tube, while a solution was pumped through it. The rheometer was placed

inside a standard Bruker mini-imaging probe which in turn was placed inside the magnet. Temperature control is available from -170 → +200 °C using a Bruker VTU system. For temperatures above ambient, nitrogen gas is pumped through the probe via a heating coil. For those temperatures below ambient , nitrogen gas is passed over liquid nitrogen before the heating coil.

The tubular reservoir (48.88 mm OD and 38.40 mm ID) to which the capillaries are attached has a 'bleed' hole located at the top. With the length of the reservoir being 400 mm, a storage volume of approximately 150 ml is possible. A small hole is also located at the bottom of the reservoir to enable pressure measurements near the capillary entrance. The pressure measurement gives the pressure difference between the beginning of the capillary tube and its exit at atmospheric pressure. This parameter is important in estimating the shear stress along the walls of the capillary. A 407 SenSym pressure transducer, connected to a 6.0 V d.c. power supply was used.

The flow rate is controlled by a Gilson, Minipulse 3, peristaltic pump. This pump has an eight roller head which reduces pulsation of the flow. An air gap of 1.0 cm located at the top of the reservoir, ensures that what pulsation is present is dampened due to the compressibility of the air.

The flow rate selection process was automated by using a Motorola, eight bit, shift register, connected to the AMX spectrometer. A TTL pulse from the spectrometer enables equally stepped flow rates. Each individual flow rate magnitude is selected by choosing the appropriate maximum flow rate.

3.4.2 The Cylindrical-Couette Rheometer

A cylindrical-Couette rheometer consists of two concentric cylinders, one inside the other (Fig. 3.10). Either the outer or the inner cylinder is rotated to deform the material placed between them. With cylindrical-Couette rheometers, the wall stress of a material is deduced by a torque measurement on the inner rod. As mentioned on page 5, rheological parameters such as viscosity can be determined given the stress and shear rate. The NMR method is used to measure the velocity profile across the deformation region for this geometry. The exact velocity distribution obtained for a Newtonian sample is given by Eqn. (3.49) where again r is the positional variation, a is the inner rod radius, b is the outer cylinder radius and ω, the angular frequency of rotation. In contrast to Eqn. (2.21) the local shear rate is now given by Eqn. (3.50). The difference between these equations is a direct result of the cylindrical polar coordinates chosen. If the sample gap is chosen to be small enough, the cylindrical-Couette geometry can produce a

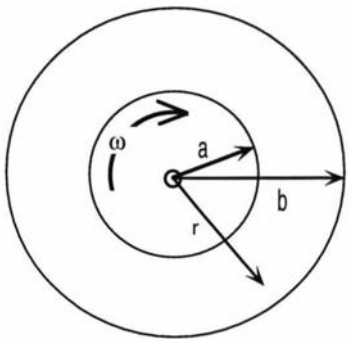

Figure 3.10: The cylindrical-Couette rheometer consists of two concentric cylinders with either the inside or outside cylinder rotating. The local shear rate of the sample varies across the sample gap according to Eqn. (3.51).

minimal variation in shear rate as a function of position as seen in Eqn. (3.51).

$$v(r) = \frac{a^2\omega}{b^2 - a^2}\left[\frac{b^2 - r^2}{r}\right] \tag{3.49}$$

$$\dot{\gamma} = r\frac{\partial\omega}{\partial r} = -\frac{\partial v}{\partial r} + \frac{v}{r} = \frac{a^2\omega}{b^2 - a^2}\left[\frac{2b^2}{r^2}\right] \tag{3.50}$$

$$\text{With} \quad r \sim b \quad \Rightarrow \dot{\gamma} \approx \frac{2a^2\omega}{b^2 - a^2} \tag{3.51}$$

Two cylindrical-Couette rheometers were constructed both consisting of a 1.98 mm ID, 4.96 mm OD glass NMR tube placed inside a 9.0 mm ID, 10.0 mm OD glass NMR tube. The only difference between the two rheometers is the length of the flexible drive shaft. This difference arises from the rheometers being used in different magnets. The shorter drive shaft length is to be used in a 1.50 T electromagnet, where the rheometer is orthogonal to the direction of the main field. In contrast, the longer drive shaft is to be used in a 7.05 T super-conducting magnet where only axial access is possible. There is a distance of 0.70 m between the center and the outside of the magnet. An inner rod rotation was chosen for simplicity of the drive mechanism. The Weissenberg effect (polymer climbing the inner rod)[1] can pose a problem with this kind of rotation, but is very dependent on viscosity and molecular weight of the sample. The rheometers are both driven by a 12.0 V d.c. electric brush motor. Because of the 'sparks' caused by the motion of the brushes, careful placement of the motor outside the magnet is essential to avoid perturbation of the r.f. signal. Both rheometers were checked to see if any difference had arisen in the F.I.D. after the motors were turned on. The result

was negative. The rotation rate can be controlled with the same eight bit shift register described earlier on page 42.

3.4.3 Combined Cylindrical-Couette-Cone-and-Plate Rheometer

A third rheometer was constructed for use at the Royal Dutch Shell Research Laboratories, Amsterdam in the Netherlands. This consisted of a combined cylindrical-Couette with an additional cone-and-plate (Fig. 3.12).

The details for the velocity dependence of the cylindrical-Couette have already been discussed in the previous section. The cone-and-plate rheometer is described pictorially in Fig. 3.11. The separation of the cone and plate depends on radius,

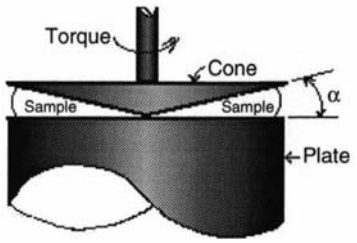

Figure 3.11: The cone-and-plate rheometer provides an ideal geometry for rheological studies as it has no variation of shear rate across the sample region for sufficiently small cone angle.

r, as $r \tan \alpha$. Because the local velocity on the cone surface is also proportional to the radius the shear rate for this geometry, Eqn. (3.54), has no radial dependence.

$$\dot{\gamma} = \frac{\partial v}{\partial z} \tag{3.52}$$

$$= \frac{\omega r}{r \tan \alpha} \tag{3.53}$$

$$= \frac{\omega}{\tan \alpha} \tag{3.54}$$

Although one suffers the obvious sample reduction with the cone-and-plate geometry, resulting in a reduction of the NMR signal, the lack of shear rate variation with position far outweighs this disadvantage.

The torque on the inner surface of the cone is produced by the shear stress ($\sigma_{r\theta}$) for varying radii on the surface of the cone. According to Eqn. (3.58) this gives an a^3 dependence for the torque, where a is the outer radius of the cone.

$$T = \sigma_{r\theta} \times \text{area of cone} \times r \tag{3.55}$$

$$= \sigma_{r\theta} \int_0^a 2\pi r \cdot r dr \tag{3.56}$$

$$= \sigma_{r\theta} 2\pi \left[\frac{1}{3} r^3\right]_0^a \tag{3.57}$$

$$= \frac{2\pi\sigma_{r\theta} a^3}{3} \tag{3.58}$$

To enable a combined cylindrical-Couette and cone-and-plate rheometer to be constructed, investigation into the cylindrical-Couette's relationship between torque and shear stress has to be undertaken. Equation (3.61) shows this relationship as follows:

$$T = \sigma_{r\theta} \times \text{area of cylinder} \times r \tag{3.59}$$

$$= 2\pi a \int_0^l dl \times a \tag{3.60}$$

$$= \sigma_{r\theta} 2\pi a^2 l \tag{3.61}$$

where l is the length of inner cylinder. A temperature controlled, combined cylindrical-Couette plus cone-and-plate rheometer, was to be incorporated into a 200 MHz Bruker super conducting magnet. The minimum rheometer cell diameter of 9.4 mm (see Fig. 3.12) is constrained to the r.f. coil's diameter of 16.0 mm and 1 mm surrounding vacuum cell. By equating equations (3.51) and (3.54) one can ensure that the shear rates experienced in the two sample regions are the same.

$$\frac{2a^2\omega}{b^2 - a^2} = \frac{\omega}{\tan\alpha} \tag{3.62}$$

$$\Rightarrow \alpha = \tan^{-1}\left(\frac{1}{2}\left[\frac{b^2}{a^2} - 1\right]\right) \tag{3.63}$$

Thus equation (3.63) requires a 'cone angle', α, of 7° if the dimensions are as given in Fig. 3.12.

The combined torque experienced by both sections in the rheometer is the sum of two terms given by equations (3.58) and (3.61), as follows:

$$T = \sigma_{r\theta} 2\pi a^2 l + \frac{\sigma_{r\theta} 2\pi a^3}{3} \tag{3.64}$$

$$= 2\pi\sigma_{r\theta} a^2 \left[l + \frac{a}{3}\right] \tag{3.65}$$

Temperature variation of the cell was achieved by pumping nitrogen gas through a standard Bruker heating coil unit, into the cell, obtaining temperatures of between 20- 200°C . A cylindrical vacuum jacket of 0.5 mm glass walls with a 1.0 mm separation was used to thermally insulate the cell, in an attempt to minimise temperature variation in the sample space.

A *vespel* center piece with a *vespel-graphite* bearing was used to reduce friction. Both materials can withstand temperatures up to 250 °C.

The rheometric drive and torque measuring motor used was a *Haake M150 Viscosimeter*, with maximum driving frequency of approximately 8 Hz. The motor's maximum torque rating was 1.47×10^{-2} N m. To eliminate magnetic fields that would perturb the FID, a length of 1.2 m was chosen for the centre guided aluminum rod which attached the motor to the rheometer inside the magnet (Fig. 3.13). This rod could be moved up and down via a screw thread bearing underneath the motor. After the rheometer was positioned inside the probe, the probe positioned inside the magnet, the rod could be lowered and attached onto the rheometer.

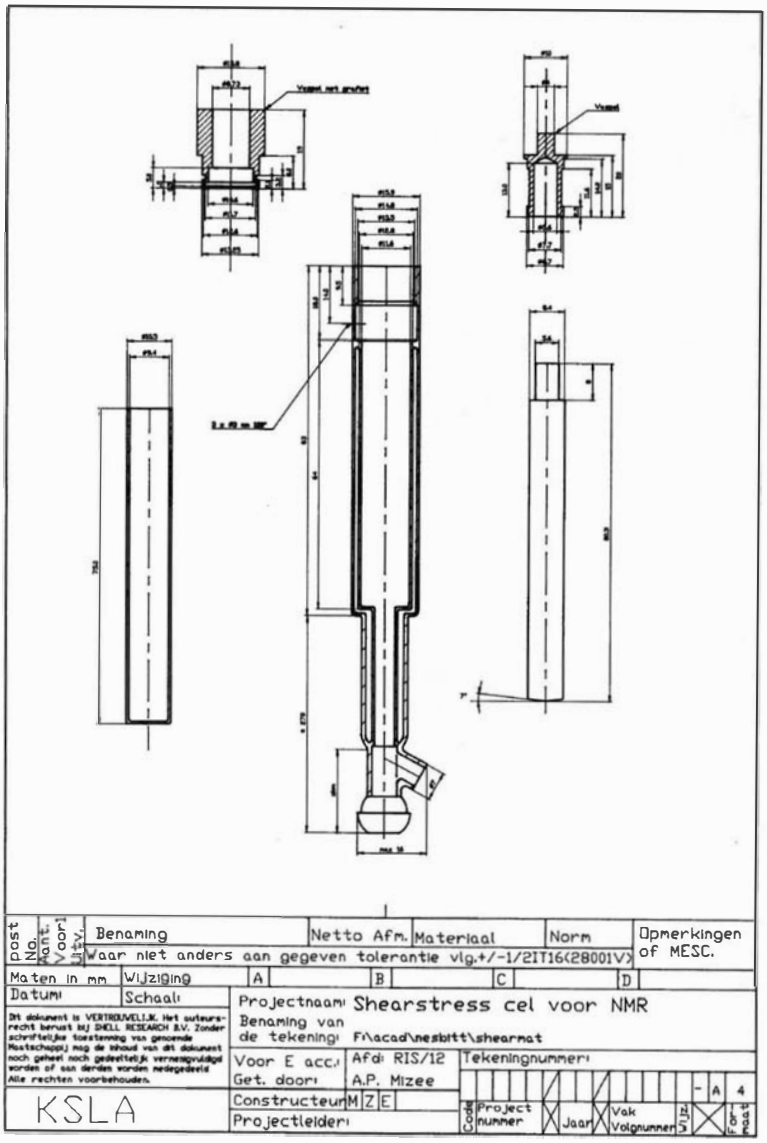

Figure 3.12: Schematic diagram of a variable temperature, combined cone-and-plate and cylindrical-Couette rheometer, for operation in a 200 MHz super conducting magnet. A 7° 'cone angle' ensures shear rates are equal in each of the rheometer regions.

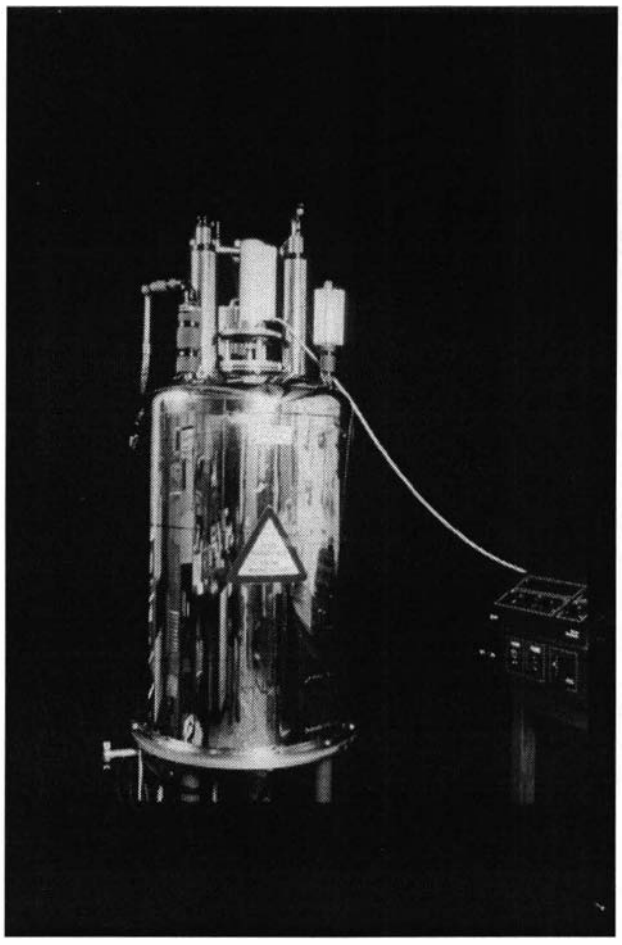

Figure 3.13: To eliminate unwanted noise, produced by the combined cylindrical-Couette and cone-and-plate rheometer's electrical motor, a distance of 1.2 m was chosen between the motor and the r.f. coil.

3.4.4 Power Law Velocity Profiles

The power law constitutive equation (Eqn. (2.18)), applied in different shearing geometries, leads to analytical solutions of the velocity distribution unique to each respective rheometer. The case of the capillary is described in equation (3.66), with R the radius of the tube, ΔP the pressure difference between the ends of the capillary and ΔL the length of the tube. This result assumes a boundary condition of zero velocity at the capillary wall. This zero-slip condition will be evident in most of the data we present here but is not always true (see Sec. 2.3.1).

$$v(r) \sim \left[\frac{\Delta P}{\Delta L}\right]\left(\frac{n}{n+1}\right)\left[R^{(n+1)/n} - r^{(n+1)/n}\right] \tag{3.66}$$

To derive the cylindrical-Couette velocity profile the momentum equation (Eqn. (3.67)) and the local shear rate (Eqn. (3.68)) are expressed in cylindrical polar coordinates, again applying the non-slip boundary condition. This yields the azimuthal velocity v_ϕ:

$$\frac{\partial}{\partial r}\left(r^2\sigma_{r\phi}\right) = 0 \tag{3.67}$$

$$\dot{\gamma} = r\frac{\partial \omega}{\partial r} \tag{3.68}$$

$$\Rightarrow \quad v_\phi = -k_1 r^{1-2/n} + k_2 r \tag{3.69}$$

where $k_1 = \left(\frac{c_1}{m}\right)^{1/n}$, $k_2 = c_2$ and c_1, c_2 are arbitrary constants.

With a central rod, of outside radius r_i, rotating with frequency ω inside the outer cylinder, of inside radius r_o, the boundary conditions are thus set: $v_\phi = \omega r_i$ at $r = r_i$ and $v_\phi = 0$ at $r = r_o$. The result is depicted in a non-dimensional form in Eqn. (3.70) with $K = \frac{r_i}{r_o}$ and $R = \frac{r}{r_o}$.

$$\frac{v_\phi}{\omega r_i} = \frac{R\left(1 - R^{-2/n}\right)}{K\left(1 - K^{-2/n}\right)} \tag{3.70}$$

It must be emphasised that the power law theory has no particular physical significance. For example it does not explain the dependence of the rheological behavior on a molecular property. Nevertheless it is helpful as a measure of the relative shear thickening or shear thinning via the magnitude of the power law exponent n.

Chapter 4

Shear Thinning of Semi-Dilute PEO Solutions

Previous investigations made by Xia and Callaghan of the behavior of *polydisperse* polyethylene oxide (PEO)[12] solutions, demonstrated the shear dependent viscosity often observed in semi-dilute polymer solutions, polymer melts and colloidal suspensions. Semi-dilute PEO/H_2O solutions exhibit a viscosity which decreases with increasing shear rate, as described in section 2.1.2.2. This phenomenon is known as *shear thinning*. The non-linear behavior was illustrated by Xia and Callaghan by measuring the velocity profiles of 0.5-4.5 % (weight per volume (w/v)) PEO/H_2O solutions across a vertical capillary tube. This data was compared to a Poiseuille flow distribution, characteristic of a Newtonian fluid. The measurements were carried out at 60 MHz in a horizontal electromagnet (Jeol FX60). An enhanced velocity gradient was observed near the cylinder's wall associated with the lowering of the local viscosity of the material. Other shear thinning studies, including the investigation here, which have appeared in publications are given in references[67]–[74].

As the production of monodisperse polymers in sufficiently large quantity for flow measurement is difficult and expensive, studies involving polydisperse polymers are usually more attractive. The work presented here investigates the behavior of *monodisperse* PEO semi-dilute solutions with diffusion, flow and viscosity measurements. To demonstrate the shear thinning behavior of this fluid in different shearing geometries, capillary, cone-and-plate and cylindrical-Couette systems were studied (refer to Sec. 3.4).

4.1 Diffusion & Velocity Measurements

The concentration dependence of self-diffusion for semi-dilute, polydisperse, PEO/D_2O solutions has been investigated by Xia and Callaghan[12]. Their findings suggested that the diffusion scaled with concentration, c, as $c^{-1.75}$. This exponent is predicted by the Doi/Edwards/de Gennes theory of reptation [38][75]– [77], based on a random coil whose dimensions scale with molar mass to the power of 0.6, consistent with excluded volume statistics. The study also included an investigation of 1.5-4.5 % (w/v) polydisperse PEO/H_2O solutions, demonstrating a characteristic 'plug' flow in capillaries. The flow profiles exhibited non-Newtonian behavior once the concentration was sufficient for entanglement effects to occur. A power law fitting procedure was utilised to gauge the extent of deviation from Poiseuille behavior, leading to a value of n of around 0.4 (refer Eqn. (3.14)).

One of the aims of the present work was to study the diffusion of *monodisperse* PEO/D_2O, and to compare its concentration dependence with the previous work of Xia and Callaghan. Another aim was to compare shear thinning behavior, extending the study to capillary *and* cylindrical-Couette geometry. It was hoped that the narrower molecular weight distribution might reveal interesting differences.

4.1.1 Experimental Setup

Monodisperse PEO was obtained from Polymer Laboratories[1]. The manufacturers estimate of the molecular weight was 930 000 da with a polydispersity factor $\frac{M_w}{M_n} = 1.12$. Various PEO/D_2O concentrations were prepared, in the range of 0.5-8.0 % (w/v). The solutions were contained in 4.0 mm NMR test tubes with copper sulphate added to reduce the T_1 relaxation time and hence increase the signal-to-noise ratio. This type of 'doping' was also used by Xia and Callaghan who found no significant change in polymer diffusion coefficients, before and after doping. This result suggested no change in the rheology or structure of the solutions had occurred. It has also been our experience that such aqueous solutions are vulnerable to bacterial degradation. Sodium azide can be used to eliminate this. It was decided not to add such a disinfectant in order to minimise perturbation to the physical chemistry of the solutions. In retrospect this turned out to be a costly strategy because of the limited lifetime of the polymer solutions.

The work described here coincided with the purchase of a new super-conducting magnet and spectrometer. Equilibrium self-diffusion measurements were completed at 28 °C, using a modified JEOL FX60 NMR spectrometer, at a proton NMR frequency of 60 MHz. A home-built PGSE 'super-G_y' probe was used for

[1] Church Stretton, Shropshire, England.

the diffusion measurements. It consisted of a 4.0 mm ID copper r.f. coil and an unscreened planar gradient coil (G_y). The maximum field gradient possible was 48.7 T m^{-1} A^{-1}.

The velocity data were collected on the Bruker (AMX) spectrometer operating at 60 MHz when used in conjunction with the electromagnet described above and at 300 MHz when used in conjunction with the vertical bore, super-conducting magnet. Both the cylindrical-Couette and capillary measurements were completed in their respective magnets at a temperature of 28 °C. Because the capillary flow experiments in the vertical bore magnet were carried out using a 1.5 mm ID tube, a standard Bruker imaging probe was used with the smallest (5.0 mm ID) r.f. insert in order to optimise the signal-to-noise ratio. Two of the three screened gradient coils (G_x, G_y) offered a maximum gradient of 0.35 T m^{-1}, while G_z gave a larger field variation of 1.06 T m^{-1}. The solutions were pumped through the capillary by pressurised nitrogen, fed from an industrial gas cylinder with an adjustable pressure regulator (see Fig. 4.1). Thus a change in the flow rate could be easily achieved by changing the pressure in the reservoir. Due to the non-cyclic pumping system, a relatively large amount of the PEO/H_2O solution was required. This criterion was met by a one litre reservoir filled almost to capacity.

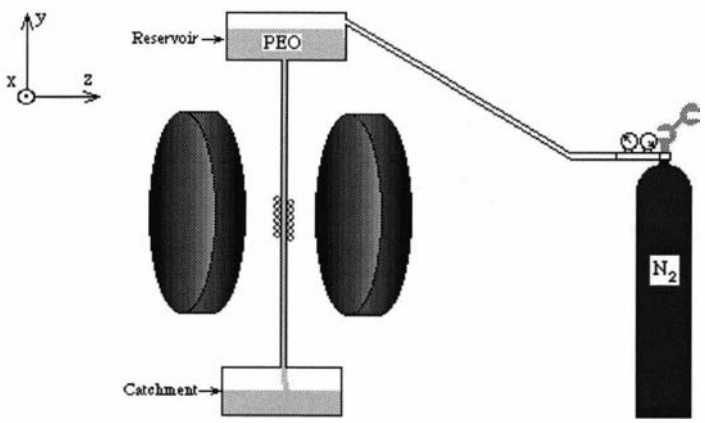

Figure 4.1: A maximum of 20 atm. pressure, provided from an industrial nitrogen cylinder, allowed a maximum flow rate of 5.8 ml min^{-1} through the 1.5 mm capillary tube. Care was taken to ensure line feeds were free from air bubbles which would cause serious anomalies in both position and velocity of the image.

Details of the cylindrical-Couette rheometer are given in section 3.4.2. The cell comprised of an inner rod of outside diameter 5.0 mm and an outer cylinder of

inner diameter 9.0 mm. The rheometer was housed inside a home-built imaging probe which used two *quadrupole* coils and a planar coil. The quadrupole (refer Sec. 8.2.1) coils, G_y and G_z, could generate a maximum gradient of around 7.12 T m^{-1}. The planar coil, G_x, offered a smaller linear field variation of 2.80 T m^{-1}. As well as rf synthesis, gradient switching was also controlled by the AMX spectrometer in conjunction with a Bruker B-AFPA 30 power amplifier. With a typical gradient coil resistance of around 2 Ω, a peak power of 1800 W is available. Depending upon the relevant pulse sequence used, the corresponding duty cycle may give a continuous power of up to 50 W.

Both the diffusion and velocity measurements utilised the pulsed gradient spin echo (PGSE) pulse sequence described in section 3.2.3. The diffusion data was calculated from the decrease of the echo amplitude as the magnitude of the gradients were increased (Eqn. (3.40)). The echo amplitude is proportional to the area of its corresponding Fourier spectrum, allowing an estimate with reduced noise because of the bandpass filtering effect of setting a narrow frequency window. Gradient durations in the range 0.1-1.0 ms were used, with separation between gradient pulses ranging from 10-100 ms. To ensure an accurate measurement of echo magnitude decay, at least 80 % attenuation was achieved in all measurements.

The velocity data was calculated by using the offset of the motional propagator with results from the ordered motion. An FFT with respect to the stepped gradient g, for each pixel in the **q** images, will reveal the shifted motion spectrum. A detailed description of this process is given in section 3.2.4.

4.1.2 Results

A sample echo attenuation plot for 930 000 da PEO in D_2O is shown in figure 4.2 along with a straight line fit based on Eqn. (3.40). The initial rapid decay is probably due to the proton signal arising from non-deuterated or partially deuterated water. This signal decays rapidly leaving the signal from the polymer protons uncontaminated at larger values of **q**. Hence the diffusion coefficients obtained from the higher **q** data are not affected by this anomaly. Figure 4.3 shows the polymer diffusion coefficients as a function of the w/v concentration of PEO. There exists a clear change in the slope around a concentration of 1-2 %, indicating the critical concentration, c^*, for the onset of polymer entanglements. The dependence of diffusion on concentration above c^* is consistent with the scaling exponent of around -1.7.

To illustrate the velocity data obtained from the cylindrical-Couette rheometer, a normalised velocity plot of a water sample is shown in figure 4.4. A central diametral slice was taken from a 128×128 velocity image with a 15.0 mm field of

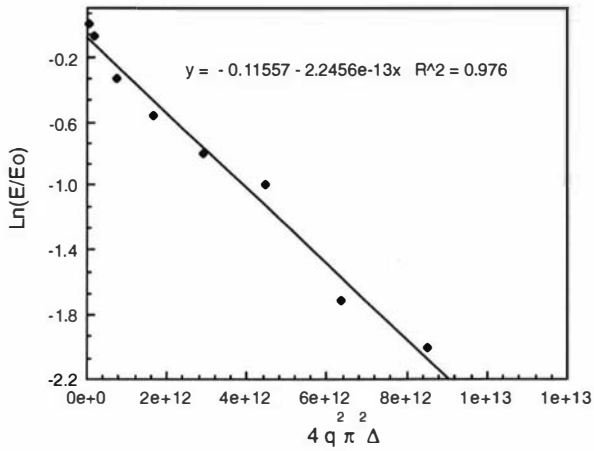

Figure 4.2: The echo attenuation associated with application of the increasing $\mathbf{q}$ gradient is a result of non-refocussed magnetisation. This is caused by the random motion associated with diffusion. The logarithmic plot of the signal versus $\mathbf{q}^2$ reveals a straight line, the slope of which is the diffusion coefficient. Note $\mathbf{q} = \gamma\delta\mathbf{g}/2\pi$.

view (FOV). The positive and negative lobes can be seen on the normalised plot, corresponding to the velocity measured perpendicular to the inner rod's direction. A rotational speed of both 0.4 and 0.8 Hz shows no change in the shape of the velocity profile typical of a Newtonian fluid, such as water. A power law fit (refer Sec. 3.4.4), with an exponent of $n = 1.0$, agrees well with the velocity distribution for this geometry.

The shape of the velocity profile obtained using 5 % monodisperse PEO/H_2O (Fig. 4.5) is quite different from that of water. In the polymer solution, shear thinning effects lead to a velocity profile which exhibited a high shear region close to the inner rod. A comparison of this region expanded (Fig. 4.6), as the inner rod's rotational frequency is increased, shows a subtle increase in the local shear rate. The difference in gradient is more pronounced closer to the inner rod where the local stress is larger (see Eqn. (3.51). A power law exponent of around 0.4 shows a good agreement for the smallest rotational speed of 0.4 Hz (see Fig. 4.7). A smaller exponent of around 0.35 best described the largest angular velocity profile. This tendency to lower power law exponent with increasing shear rate is also apparent in mechanical measurements using a cone-and-plate rheometer (Fig. 4.6) and is entirely consistent with both the Doi-Edwards and Graessley[78] models for entangled polymer non-linear viscosity.

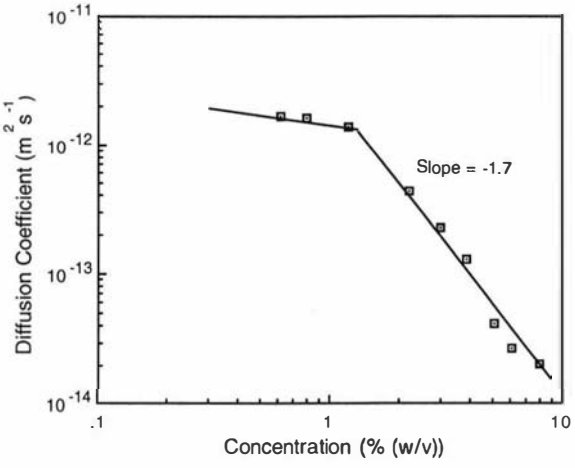

Figure 4.3: Double logarithmic plot of diffusion versus concentration for 930 000 da PEO in D_2O. The change in the slope at around 1 % concentration suggests a c^* transition to an entangled state.

Figure 4.8 shows comparative data for the same solution flowing in a capillary tube. Again a diametral slice is shown with a corresponding FOV of 2.5 mm. A comparison can be made between the velocity distribution of the 5 % PEO/H_2O and a power law fit of $n = 0.4$. Although the velocity contrast is poor, a reasonable agreement is found. The maximum velocity of approx. 11.0 mm s^{-1} determines that the shear rate is 30 s^{-1} at the tube walls.

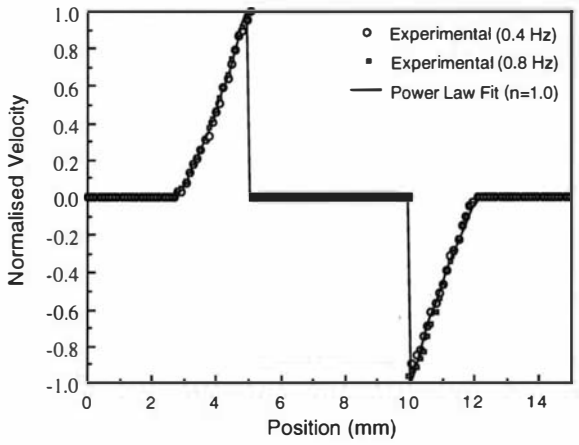

Figure 4.4: The Newtonian behavior of water in a cylindrical-Couette rheometer is demonstrated by the fitted power law exponent of $n = 1.0$.

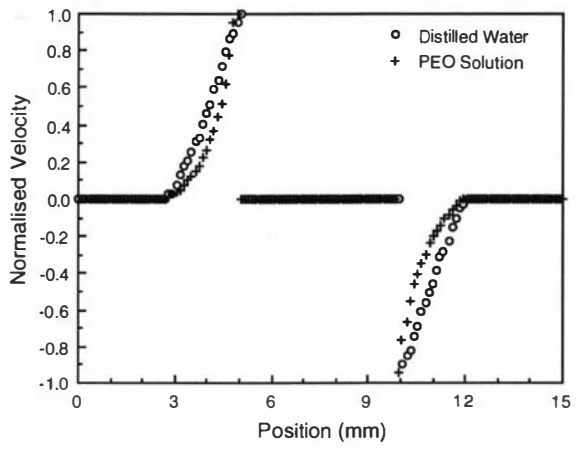

Figure 4.5: A comparison of water and PEO/water velocity profiles in a cylindrical-Couette geometry, rotating at a frequency of 0.8 Hz, shows an increase in the velocity gradient close to the inner rotating rod.

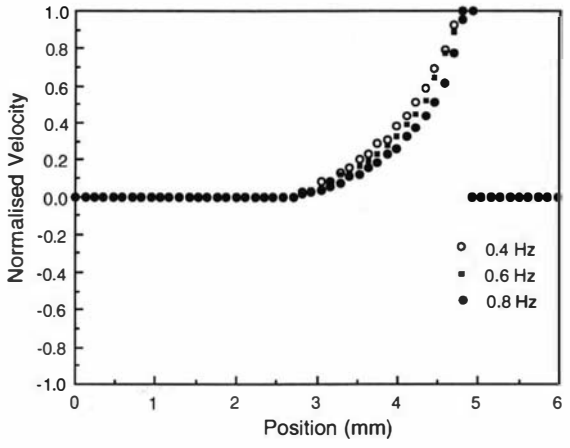

Figure 4.6: As the frequency of rotation is increased an increase in the velocity gradient is seen in regions of high shear, next to the inner rod.

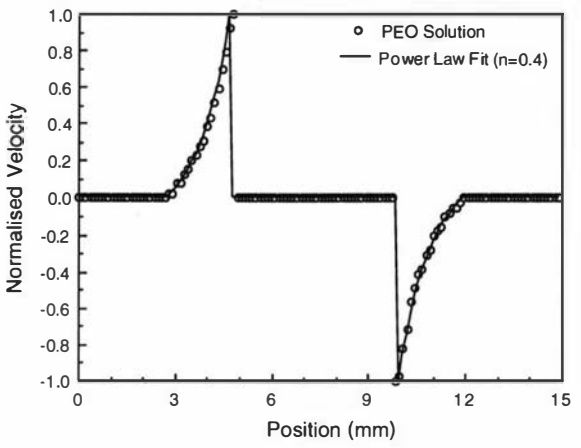

Figure 4.7: The extent of shear thinning is depicted by fitting a power law fit to the velocity data. An exponent of $n = 0.4$ best describes the velocity distribution in the cylindrical-Couette geometry.

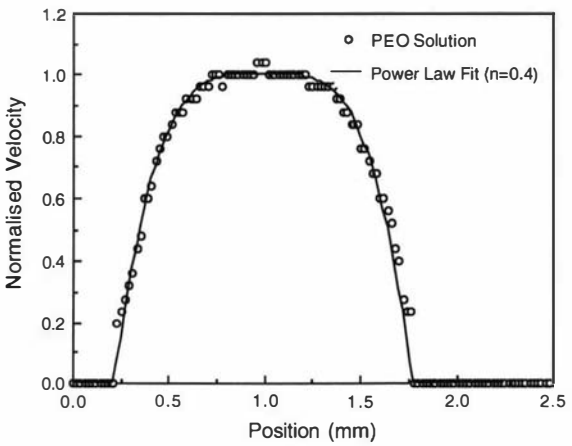

Figure 4.8: A similar power law exponent of $n = 0.4$ is obtained for velocity data in a capillary geometry as that of the cylindrical-Couette.

4.2 Discussion

It is clear that the diffusion and velocity profile data obtained by Xia and Callaghan, using polydisperse PEO in water, is broadly similar to that observed here using monodisperse PEO. The present data can be used to obtain an independent estimate of the molecular weight of the monodisperse PEO, used in this work. Xia and Callaghan carried out a measurement of monodisperse PEO self diffusion with varying molar mass at a fixed concentration of 5.0 % (w/v). A polymer diffusion coefficient of 3×10^{-14} m^2s^{-1} is found for the 5 % concentration with the work presented here. This corresponds to a molecular weight of around 950 000 da found with Xia and Callaghan's monodisperse PEO study. This molecular weight agrees well with the manufacturers estimated molecular weight of 930 000 da.

The concentration, c^*, found for the 930 000 da PEO is larger than that observed by Xia and Callaghan, consistent with the larger molecular weight of PEO (1.6×10^6 da) used in the earlier work. The scaling dependence of the diffusion coefficient on concentration for the 930 000 da PEO ($c^{-1.67}$) is also close to that measured previously ($c^{-1.75}$). It is not our intention to debate whether such apparent scaling behavior is evidence that the reptation hypotheses are correct, but simply to demonstrate that these findings are broadly consistent with previous measurements.

Cylindrical-Couette velocity measurements demonstrated the shear thinning behavior of the semi-dilute PEO solution. The fitted velocity profile show good agreement with a corresponding power law exponent of 0.4. It is noted that this value is consistent to a similar fitting procedure for the capillary measurements. This consistency is evident despite the fact that the material is subjected to vastly different local shear rates; 0-7.2 s^{-1} for the cylindrical-Couette and 0-30 s^{-1} for the capillary. In addition, this work is again comparable to the capillary velocity measurements of Xia and Callaghan which show the same power exponent at similar 4.5 % concentration.

Independent viscosity measurements were also carried out on the 5 % PEO solution using a Bohlin cone-and-plate rheometer (see Sec. 3.4.3). The cone had a 2.5 ° incline and a 30 mm OD. A 4.29 Kg m^{-1} torsional bar was used to ensure a sufficient response was recorded from the material's deformation. An identical temperature to that used in the velocity measurements (28 °C) was provided by a variable temperature water bath. A shear rate range was chosen to provide a comparative strain rate regime as the cylindrical-Couette and capillary velocity measurements. The shear rate was started from 5.0 s^{-1}, swept to 50.8 s^{-1}, then returned to 5.0 s^{-1}. Each individual measurement was maintained for 10 s before continuing to the next data point. No hysteresis effects were found. Figure 4.9

reveals the reduction in the viscosity as the shear rate is increased with one sixth of the material's low shear viscosity achieved as 50 s^{-1} is reached. A closer inspection

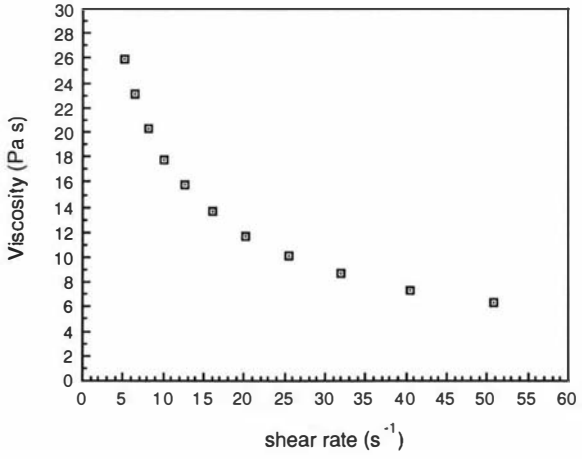

Figure 4.9: Again the shear thinning behavior of a PEO solution is demonstrated, but here the absolute viscosity has been measured.

of the scaling of this viscosity with shear rate is achieved if the double logarithm of Fig. 4.9 is sought. Eqn. (2.19) predicts the slope of the logarithmic plot would allow the magnitude of the power law exponent to be determined. Figure 4.10 suggests that the value of this exponent is around 0.39. The agreement of this exponent with power law exponent values determined earlier using velocity profile fitting, is encouraging. These findings suggest that the constitutive equation (Eqn. (2.18)) has general applicability in predicting velocity profiles and that analysis of these profiles provide another method for determining the extent of shear thinning.

A possible explanation for shear thinning is that migration[79] of solvent and solute forms an inhomogeneous flow regime. The resulting concentration gradient may be caused by the difference in the local shear rate and result in a difference in the local viscosity. Thus in the study here, such a model would predict that the increase in the velocity observed at the capillary walls could be due to a higher concentration of water in the highest shear rate regions. Thus a larger PEO concentration would be found in the center of the tube.

A chemical-selective pulse sequence was used to establish if any differences in PEO/H_2O concentrations could be detected in the capillary while the PEO solution was being pumped. Chemical-selective imaging is not new, having been

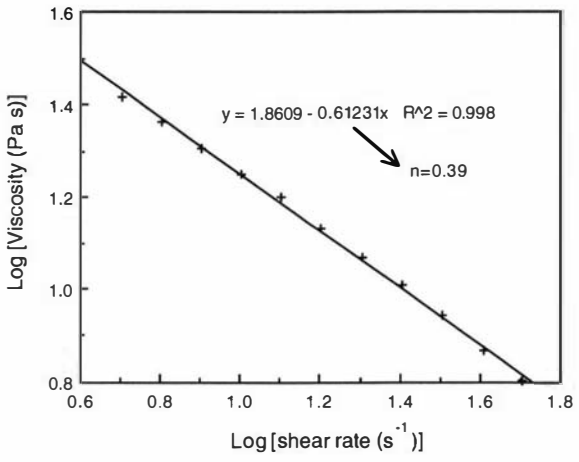

Figure 4.10: An independent method for determining the power law exponent reveals a value similar to previous velocity profile fitting methods.

reported in other applications of NMR imaging to botany[80, 81] and material science[82] (see also Sec. 8.3). Chemical-selection is based on the NMR frequency difference of nuclei due to their different chemical and hence electronic environment. (refer to Sec. 3.1.4). Thus, a method for selecting only the protons located on the PEO chain without water protons is available. Approximately 300 Hz separates the water and PEO spectra, ensuring no 'overlap' of the signals obtained from the respective nuclei. A pulse sequence similar to that used here is shown in Fig. 3.6 where the 180° 'hard' pulse is now replaced by a 180° 'soft' pulse. The lack of coexisting field gradients for this 180° pulse means that the frequency selection is 'chemical' rather than 'spatial'.

The 5.0 % solution of PEO/H_2O was pumped through the same 1.5 mm capillary tube with flow conditions identical to those described earlier. Profiles of the proton intensity are shown in Fig. 4.11 for both the water and PEO signals. To enhance the comparison, both profiles have been normalised. No significant differences between the plots were observed and the magnitude is similar across the entire cross-section of the tube. Thus no evidence was found to support a migration model for the shear thinning phenomenon.

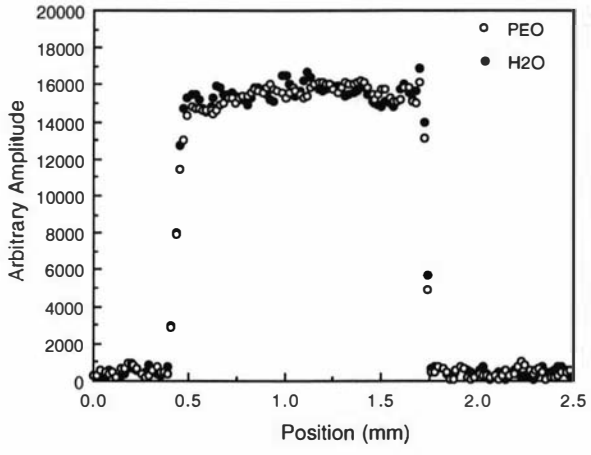

Figure 4.11: Migration of PEO or water appears absent, as the magnitudes for both respective profiles are essentially the same.

4.3 Conclusions

In summary, *monodisperse* PEO exhibits shear thinning behavior in both capillary and cylindrical-Couette shearing geometries. The capillary results are similar to those found in an earlier study using polydisperse PEO in water. Similar agreement is found in a study of polymer self-diffusion and its dependence upon concentration. The extension to Couette geometry as described in this work is quite new and illustrates that Rheo-NMR studies can be carried out with small sample volume in this more convenient arrangement. We have also found, using the cylindrical-Couette cell, that shear thinning increases with increasing shear rate. The extent of shear thinning is measurable by the power law velocity fitting procedure and is entirely consistent with rheometric studies using a cone-and-plate viscometer, as well as being consistent with both the Doi-Edwards and Graessley models of shear thinning in entangled polymer solutions. It is a significant outcome of the present study that despite the monodispersity of the polymer used, no 'spurt effect' was observed in capillary flow. In all the velocity profiles examined, a no slip boundary condition was found and the dependence of flow rate on applied stress appeared monotonic. In chapter 6, where a study of wormlike surfactant flow is described, strong spurt effects will be demonstrated.

Chapter 5

Slip Behavior of Xanthan Gum Solutions

In this chapter it is the intention of the author to repeat earlier experiments which have *indirectly* observed the slip phenomenon. As discussed in section 2.3.1 Mooney plots have been a useful tool, demonstrating that the slip velocity is not only a function of wall shear stress, σ_w, but also of the ratio of a capillary's length to diameter ($\frac{L}{D}$)[23]. These studies were completed using 0.2 % (w/v) *Unam* Xanthan gum solutions, gravitated from a reservoir into varying length and diameter horizontal capillary tubes. The capillary wall stress was estimated by measuring the pressure at the entrance of the capillary tube using a diaphragm pressure transducer. The flow rate's dependence on tube diameter leads to an estimate of the magnitude of the slip velocity.

The data presented here is predominantly velocity profile measurements obtained across a pipe using the same capillary geometry as the earlier studies described above. It was hoped that a *direct* measurement of the slip velocity could be achieved, as well as its dependence on $\frac{L}{D}$ and reservoir-capillary dimensions[83].

5.1 Xanthan Gum

Xanthan gum is a polysaccharide used in industry as a food thickener. The gum can also produce stabilising emulsions and lubricants. Industrially useful polysaccharides not only sweeten mixtures but also modify the rheological properties of aqueous solutions[84, 85].

5.1.1 Structure

Xanthan gum is a high molecular weight heteropolysaccharide comprising three monosaccharides; mannose, glucose and glucuronic acid. The repeating unit structure of Xanthan gum[86, 87] is shown in figure 5.1. A molecular weight of up to 2 million da can be expected for Xanthan gum[88], but values as high as 13-50 million da have also been reported. X-ray diffraction studies show that Xanthan

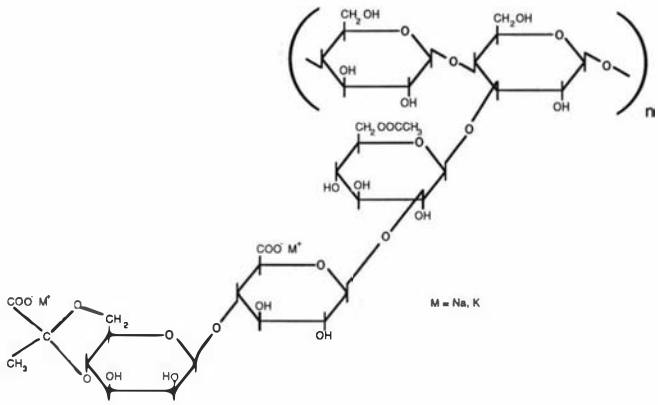

Figure 5.1: The primary structure of Xanthan gum reveals the repeating unit of the polysaccharide is comprised of three monosaccharides: mannose, glucose and gluconic acid.

gum has a right handed helical backbone with the tri-saccharide side branches aligning with the backbone[89]. Solution studies have also shown the Xanthan molecule is rodlike with a certain degree of flexibility[90].

The overall conformational stability has been suggested to rely on non covalent interactions between backbones of different chains[91]. It has been suggested that these weak interactions form complex network aggregates which are easily disrupted under the influence of shear.

5.1.2 Properties

Solutions of Xanthan gum display unique rheological properties such as high viscosity at low concentrations, high viscosity at low shear rates and high elasticity[92]. Xanthan solutions exhibit high stability over a wide range of solution conditions, including ionic strength variations, heat, pH changes, shear, additions of acids, bases and salts[93].

Xanthan gum solutions are pseudoplastic; when shear stress is applied the viscosity of the solution decreases in proportion to the amount of shear. Upon release of shear the viscosity is instantaneously restored. The decrease in viscosity with applied shear is a result of complex aggregates, bound by weak hydrogen bonding, easily broken under shear. Once the shearing force is removed, the aggregates reassociate to produce high viscosity. These aggregates, along with stiff rod-like molecules, are also the reason for Xanthan solutions having a high viscosity at low shear rates.

5.1.3 Molecular Weight Distribution

Three different sources of Xanthan gum were used in the study presented here: Unam[1], Kelsan[2] and Aldrich[3]. The molecular weight distribution of all three polymers was determined by gel permeatation chromatography (GPC). This work was carried out by Dick Poll at the Biochemistry Department, Massey University. The GPC method involves the gravitation of polymer solutions through a vertical tube filled with regular diameter beads. The larger molecular weight polymers pass through the column faster as they are less likely to be absorbed by the beads. By using a standard sample of known molecular weight as a reference, the molecular weight distribution of another polymer system may be determined.

Saturated solutions of Xanthan polymers were made using distilled water and then filtered through 0.2 μm filter paper. A 300 mm length, 10 mm ID tube was loosely packed with 12.0 μm crosslinked agarose beads and filled with 50 mM sodium chloride in water. Each Xanthan solution in turn was passed through the column and detected by a light sensitive meter positioned at the bottom of the column. The absorption of the light is proportional to the concentration of the solution. Figure 5.2 shows a plot of concentration of the solutions versus the log of time. To establish the *absolute* molecular weight of the Xanthan samples, a saturated solution of poly(ethylene) oxide (PEO) was also prepared and passed through the GPC column. Previous light scattering measurements of this polymer carried out by Polymer Laboratories[4] gave predominant molecular weights of 847,000 and 105,000 da. Comparison of each Xanthan data set with the PEO data shows peak molecular weights on the order of 1.0 Mda for both Unam and Kelsan but a lower value of 0.7 Mda for Aldrich. Also lower weight components are observed centered around 10 kda.

[1] (U)niversidad (N)acoinal (A)utonoma de (M)exico.

[2] Named by the Kelco chemical company.

[3] Aldrich chemical company.

[4] Polymer Laboratories, Church Stretton, Shropshire, England.

It must be noted that comparison of branched polymers such as Xanthan gum with PEO, which is a linear polymer, can give misleading results. In general a smaller dimension is expected for a branched polymer than a linear polymer of the same molecular weight. Since GPC separation depends on size, we expect an apparent molecular weight for a branched polymer which is lower than its true weight. A combination of light scattering and GPC can overcome the apparent weight problem and is discussed in more detail on page 113.

Since light scattering-GPC measurements are unavailable for comparison with the above GPC results, the molecular weights measured here give a comparative measurement. Any difference in apparent and actual molecular weights of the above study are assumed small, as the branch length is comparatively small to the backbone length.

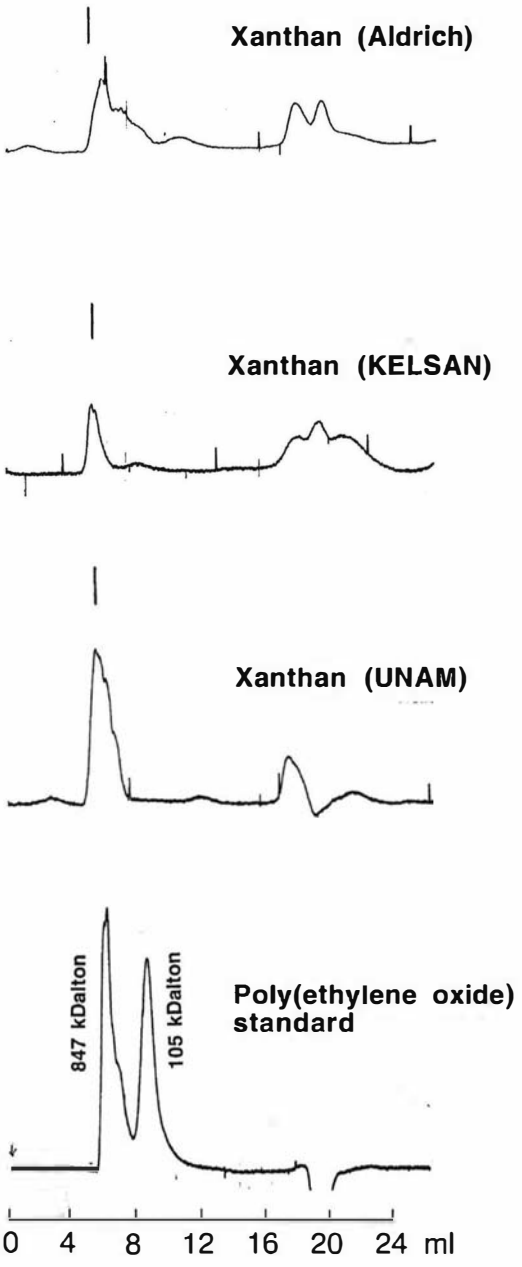

Figure 5.2: Gel permeatation chromatography (GPC) reveals the molecular weight of the Xanthan gums are on the order of 1 Mda. Comparisons of GPC data of a non-branched polymer (poly(ethylene oxide)) and a branched polymer (Xanthan gum) are assumed correct as side branch length is comparatively small.

5.2 Cone and Plate Viscosity Measurements

To investigate the shear thinning and elastic properties of 0.2 % Unam Xanthan gum solution, a *Bohlin* cone-and-plate rheometer was used for rheological measurements. This work was carried out by Rod Lambert[5]. A full description of the cone-and-plate cell is given in section 3.4.3. A 2.5° angle, 30 mm OD cone was chosen with a similar sized plate connected to a computerised water bath keeping the temperature constant to within ± 0.1 °C. The measurements here were completed at a temperature of 22.0 °C.

A 0.2 % (w/v) solution of Unam Xanthan gum was prepared using distilled water as a solvent. Because the solution degraded within approximately four days after preparation, it was essential that every new solution was prepared identically. Also, because the Xanthan solution was to be used in NMR experiments requiring long experimental time (see section 5.4), a large quantity had to be prepared each time. Another reason for careful preparation of the Xanthan solutions was the tendency of the solutions to coagulate, forming highly viscous 'blobs'. This effect is undesirable and can be avoided by long, slow mixing times. The following mixing method was used:

1. To ensure no bacteria were present in the mixing vessel, a 5.0 litre conical flask was sterilised using firstly detergent and distilled water. Secondly, the flask was rinsed with ethanol and finally distilled water.

2. 2.00 ± 0.01 litre of distilled water was measured using a standard measuring cylinder.

3. 4.00 ± 0.01 g of Unam Xanthan gum powder was weighed on a piece of dry filter paper using a digital balance.

4. The 2.0 litres of solvent was stirred using a magnetic stirrer operating at 60 rpm.

5. The Xanthan powder was slowly added to the solvent, 1.0 g every hour.

6. After mixing the solution was refrigerated at 4.0 °C for 24 hours.

7. 12 hours before an intended experiment the Xanthan solution was allowed to equilibrate to room temperature.

The comparatively low rotational stirring speed was to ensure no fragmentation of the Xanthan polymer. Refrigeration of the solution provided protection from bacterial degradation over the further period of time needed before dissolution.

[5] Physics Department, Massey University

Shown in figure 5.3 are the results from two constant shearing experiments. Each experiment was completed at different shear rate regimes to establish whether the extent of shear thinning is constant throughout a large shear rate range. The first shear rate range was from 0.004 - 0.06 s^{-1} and the second 0.8 - 501.2 s^{-1}. The experiment clearly demonstrates the decrease in viscosity as the shear rate is increased. By fitting a best fit regression line through the present data, a power law exponent, n, is given as $n = 0.402 \pm 0.002$.

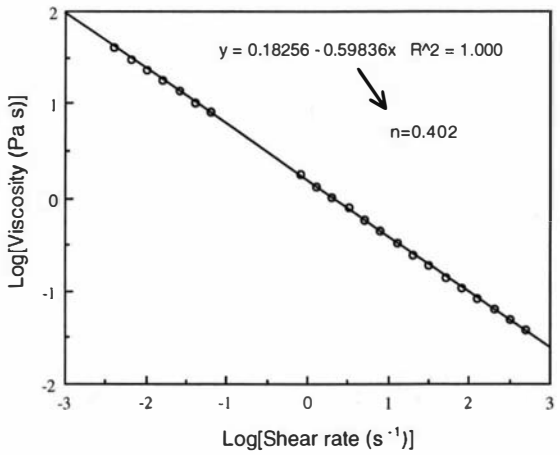

Figure 5.3: Powerlaw fitting of the viscosity versus shear rate data show $n = 0.402$. This value is consistent to as low a shear rate as 0.0040 s^{-1}.

Dynamic oscillatory experiments were also completed on the Xanthan sample as seen in figure 5.4. The same cone-and-plate, as used in the constant shear experiments, was used here. The results clearly reveal the storage modulus , G', having a higher value than the loss modulus, G'', even to as low a frequency as 0.1 Hz. Thus the solution behaves as an elastic fluid in a comparatively low shear rate regime. Such behavior of low concentration solutions has been attributed to the Xanthan polymer having high structure and being solid-like[92]. The suspending properties of Xanthan gum are largely attributed to these properties.

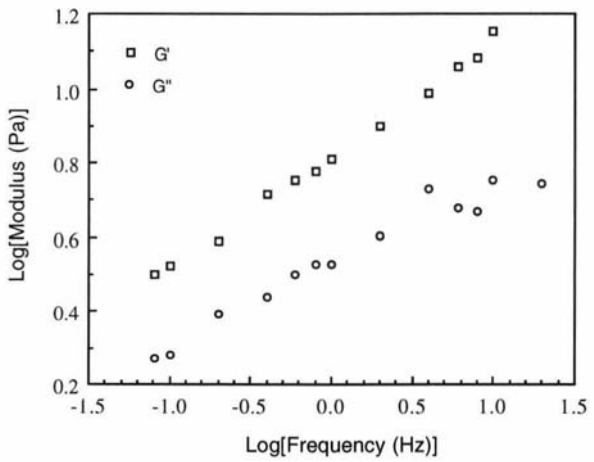

Figure 5.4: Dynamic rheological tests reveal that 0.2 % Unam Xanthan solution has a storage modulus larger than the loss modulus to as low a frequency as 0.1 Hz. This elastic behavior of Xanthan gum is typical for low concentration solutions.

5.3 Velocity Measurements in Cylindrical-Couette Flow

5.3.1 Experimental Setup

Investigation of the 0.2 % Xanthan gum solution was undertaken to see if the slip behavior could be observed directly. This was achieved by measuring the velocity distribution of the solution while being sheared in a cylindrical-Couette geometry. The geometric details of the rheometer are given in section 3.4.2 and chapter 4 where, for the latter reference, the rheometer was used for velocity measurements of the PEO solutions. Of note are the inner and outer diameters of the inner rotating rod rheometer namely; 3.28 ID, 4.96 OD and 9.00 ID 10.00 OD mm. With these dimensions and an approximate maximum rotation frequency of 2 Hz, a maximum shear rate of up to 10 s^{-1} is possible for a Newtonian solution. The orientation of the rheometer used in a 7.05 T super-conducting vertical magnet is shown in figure 5.5. As a large signal-to-noise ratio was sought, a 10.0 mm

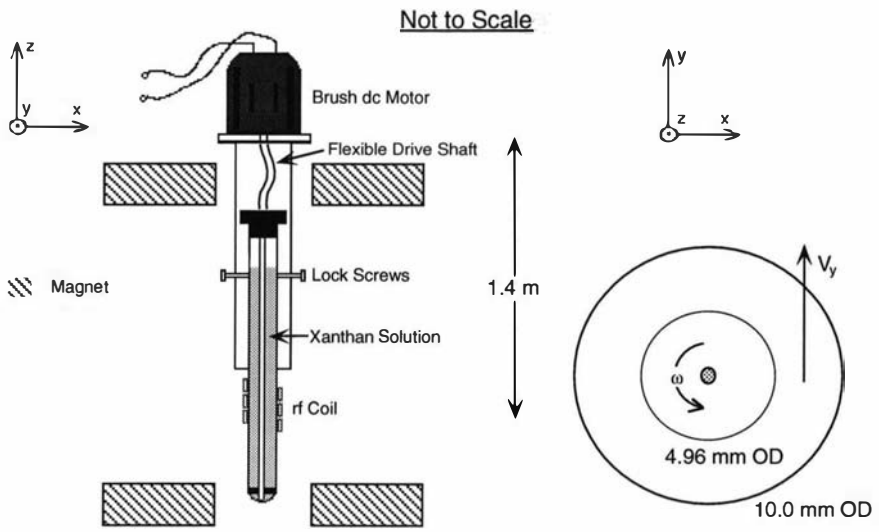

Figure 5.5: The cylindrical-Couette rheometer was placed in a vertical 7.05 T super-conducting magnet. A 10.0 mm ID r.f. coil was chosen to maximise the 'filling factor' and hence the signal-to-noise ratio.

ID r.f. coil was chosen. This diameter allowed the maximum volume of sample nuclei to coil volume, known as the 'filling factor', a criterion used to optimise the signal-to-noise ratio.

The velocity distribution was calculated using the proton q-space Fourier trans-

form method described in section 3.2.3 where 8 q-slices were chosen to ensure a relatively short experiment time of around one hour. The Unam Xanthan gum solution was placed between the concentric cylinders. In addition a small portion of the sample was placed inside the inner cylinder. The existence of a sample in a region of non-shear, inside the inner cylinder, made possible an extrapolation of the rigid body velocity profile. This extrapolation into the region between the cylinders enabled a determination of the velocity of the outer surface of the inner rotating cylinder, thus revealing the extent of slip.

5.3.2 Results

Figure 5.6 shows images of the complete rheometer cell using a field of view of 12.0 mm. A series of two 128×128 real and imaginary q images show phase stripes associated with the movement of the nuclei. A comparison of these stripes from one q slice to the next reveals the evolution of the phase differences as the q gradient is increased from zero to a maximum of 1.06 T m^{-1}. In increasing the magnitude of the gradient the effects of diffusive attenuation are also clearly visible. The phase differences are compared over a time duration of 50.0 ms with each q gradient being applied for 1.5 ms. The modulus image, calculated from the first real and imaginary images of the sequence where the q gradient was zero, and the velocity image are shown at the end of the q-slice sequence. The modulus image, which shows the proton concentration as a function of position, would suggest the inner rotating rod was not perfectly circular. As the rod was indeed circular, the image effect has been attributed to the time delay between the application of the phase encoding and read encoding gradients. The intensity modulations are due to signal caused by non-relaxed nuclei from one FID collection interfering with those from another rf pulse in a subsequent acquisition. These distortions are absent if a pixel wide profile is chosen in the centre of the rheometer from left to right. Thus when the velocity profile of the rheometer is sought a similar profile must be taken.

A clearer contrast of the velocity distribution can be seen in figure 5.7 where a stackplot has been constructed. The region of non-shear within the cell can be seen where the velocity distribution $v(r)$ obeys a linear relationship with position r, $v = r\omega$. Thus this plane can be extrapolated to obtain the velocity of the outside of the inner rod, adjacent to the sheared solution.

To increase the accuracy of the velocity measurements the spatial resolution of the velocity map must be increased. This required the excitation of a smaller region of the sample if image 'foldback' was to be avoided. This excitation was produced by two slice selective pulses in the x and y directions. The exact pulse sequence is shown in figure 5.8. As the T_1 relaxation time of the 'undoped' 0.2 % Xanthan solution is long, repetition times up to 2 seconds were required. This time was shortened by applying 1 ms gradient pulses on all three gradients after collection of the FID (see Fig. 5.8). A 5.0 mm × 10.0 mm FOV for the respective x and y positions were chosen.

An example of the increased resolution velocity image is shown in figure 5.9 showing the velocity profile of the Couette cell. An approximate rotation speed of 0.26 Hz was set by adjusting the rheostat-controlled electric motor. As seen, an extrapolation reveals the velocity in the sheared region having a much lower value than that of the adjacent wall. This phenomenon has been attributed to slip where

a large velocity gradient in a thin layer has occurred between the inner rod and the Xanthan gum solution. The extent of slip can be considered by measuring the ratio of the extrapolated velocity on the outside of the inner rod to the maximum velocity obtained by the fluid at the same position. In comparing these ratios at two different rotation speeds of 0.26 and 0.53 Hz an increase in slip at faster rotation speeds is suggested (Fig. 5.9 (b)). Direct comparison of the velocities can be made as the ratios shown are normalised. It must be noted that since velocities for each pixel are calculated from an average over the corresponding distance, pixels that may overlap at boundaries such as the inner and outer cylinders are weighted with more error. Additionally with the inner rod moving perpendicular to the velocity direction a smearing or blurring of the average velocity may occur within the nearest pixel(s) to the rod.

In support of the power law model to characterise Xanthan gum in the previous section, figure 5.10 shows the normalised velocity data fitted with the analytical expression for a power law fluid in a cylindrical-Couette geometry (refer to Eqn. (3.70)). The agreement is quite good provided the slip phenomenon is incorporated. Thus in addition to the analytical velocity expression described in section 3.4.4 is the slip velocity, V_s, expressed as a fraction of the maximum velocity. This parameter can be seen on the inner wall of the outer cylinder where the finite velocity can be observed. This non-zero magnitude contrasts with a Newtonian fluid (refer to Eqn. (2.21)).

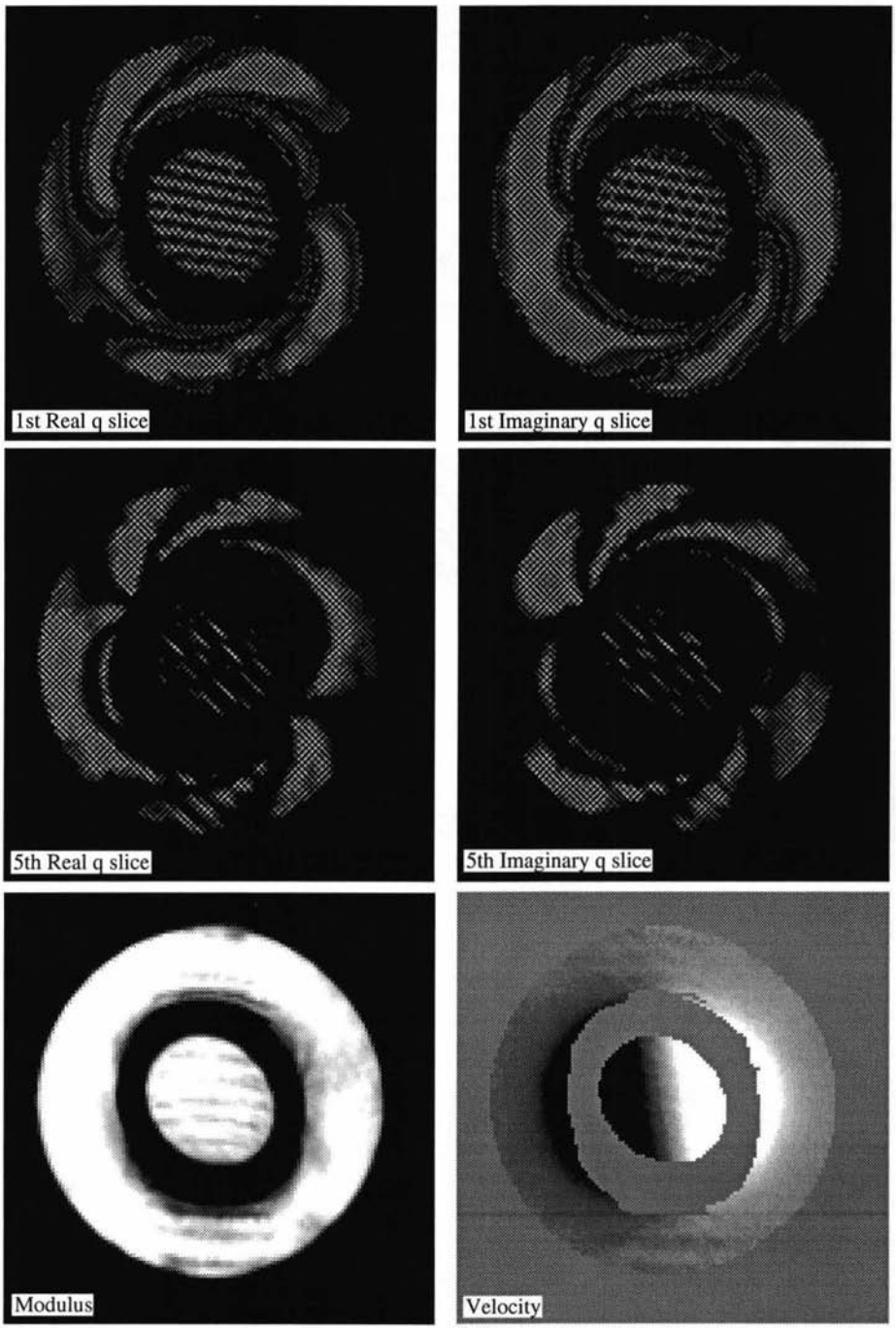

Figure 5.6: The phase stripes appearing in the three pair of real and imaginary q-slices suggest a very different velocity spatial dependence is observed between the inside and outside of the inner rod. Both the modulus of the first q images and the velocity image itself show a lack of signal in the image giving a fictitious asymmetry of the rheometer cell.

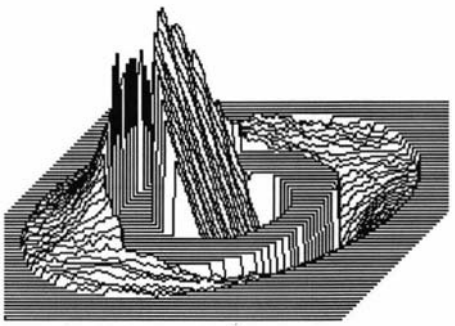

Figure 5.7: The velocities' linear spatial dependence can be clearly seen at the centre of the rotating inner rod. An extrapolation of this plane to the equivalent position of the outside of the inner rod will predict the velocity at this position.

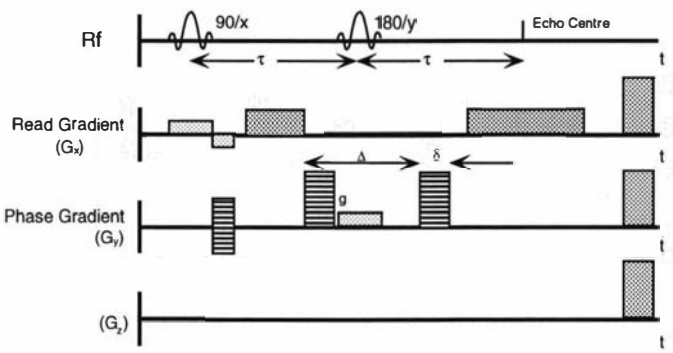

Figure 5.8: To increase the spatial resolution of the velocity calculation two slice selective pulses (90° and 180°) are used ensuring 'foldback' of the image is avoided.

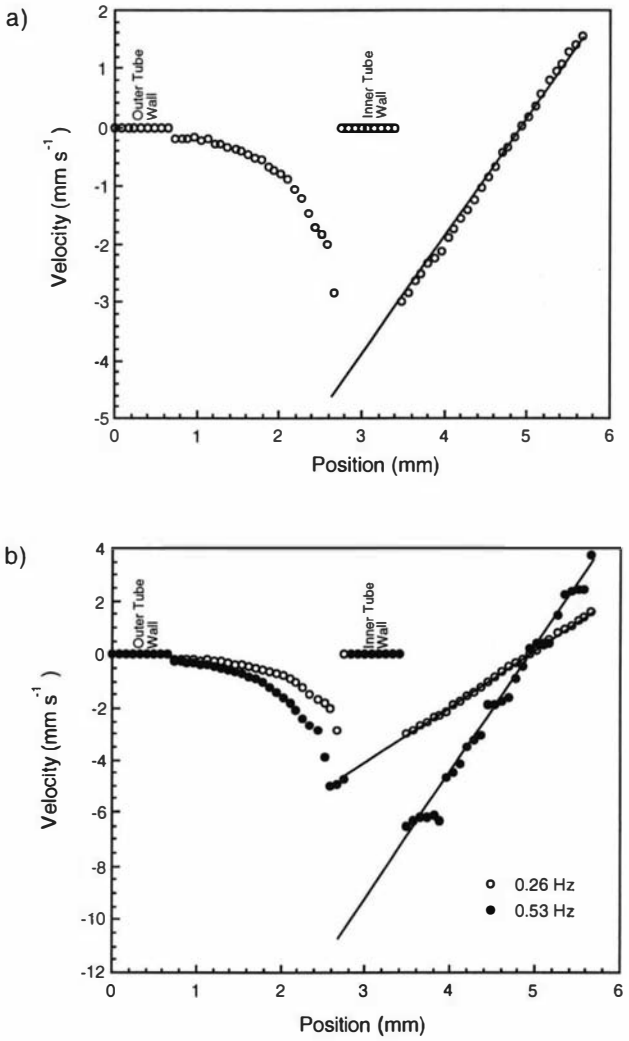

Figure 5.9: (a) The velocity distribution of the Xanthan gum in the cylindrical-Couette rheometer clearly shows the regions within the cell where non-shear (velocity has linear dependence with position) and shear are occurring. An extrapolation of the linearly dependent velocity reveals the amount of slippage that is occurring in the shearing area of the cell. (b) A comparison of the velocity distribution at frequencies of 0.26 and 0.53 Hz suggest an increase of slip at the inner and outer walls of the rheometer.

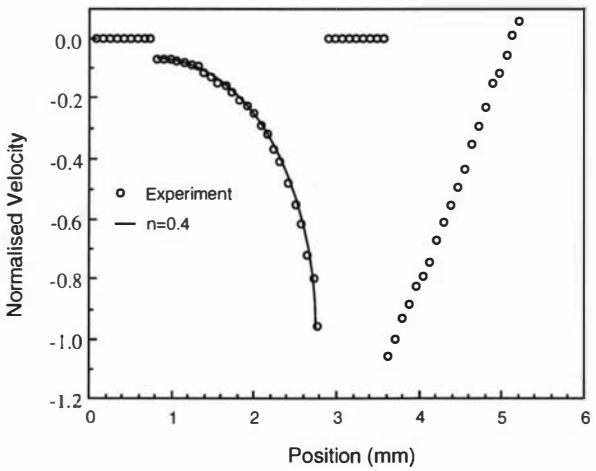

Figure 5.10: The power law behavior of Xanthan gum, consistent with other findings in section 5.2, is observed when the cylindrical-Couette normalised velocity distribution is fitted with the analytical data for the same geometry. Again a consistent power law exponent of 0.40 is demonstrated.

5.4 Velocity Measurements in Capillary Flow

5.4.1 Experimental Setup

A capillary rheometer (described in Sec. 3.4.1) was also used to investigate the slip behavior of the 0.2 % Xanthan gum solution. The capillary experiment had a special importance since it enabled direct comparison of results to be made with previous work in which slip was indirectly observed through flow rate and pressure measurements in the same geometry[23].

Capillary tube inner diameters of 2.6±0.1 and 5.0±0.1 mm were used, the overall capillary length being 1.0 m. This rheometer was placed in the same 7.05 T vertical magnet as described on page 71 . In contrast to the cylindrical-Couette rheometer, velocity measurements were collinear with the direction of the main magnetic field, z. This new direction was achieved by exchanging the assignment of the gradient coils x and z and by using an identical pulse sequence as in the cylindrical-Couette experiments (page 73).

In addition to the capillary rheometer described in section 3.4.1 a smaller diameter reservoir (30 mm OD, 20 mm ID) was also used here to investigate the effects of the velocity distribution across the tubes under different contraction ratios $\frac{W}{D}$ where W is the diameter of the Xanthan reservoir. With the use of both reservoirs contraction ratios of 15.4, 8 and 4 were available.

5.4.2 Results

Shown in figure 5.11 is a typical set of velocity profile data obtained for flow rates ranging from 1.10 to 5.60 ml min^{-1} in the 2.6 mm ID capillary tube. This flow rate range corresponds to an apparent shear rate range of 10.6 to 54.1 s^{-1}. The largest contraction ratio of 15.4 was used and a resolution of 31 μm enabled an accurate measurement of the velocity across the capillary tube. The position along the tube at which the velocity is measured is expressed as a ratio of the distance from the entrance of the tube, L, to the tube diameter, D, ie. $\frac{L}{D}$. Although this ratio is similar to the previous work of Mooney et al[19], it must be strongly emphasised that in the work presented here the definition of this ratio is not the same. Mooney et al refer to the total length of the capillary tube, whereas in the NMR work here reference is made to the distance the velocity profile is measured from the entrance of the pipe. To avoid confusion an alternative expression of $\frac{l}{D}$ is chosen for the different ratio of *length* of the capillary to the tube diameter. The data set of figure 5.11 have an $\frac{L}{D}$ of 216 whereas $\frac{l}{D}$ is 385.

As Mooney interpreted, a large apparent discontinuity in the velocity is observed at the capillary wall. This discontinuity is evident for all the measured flow

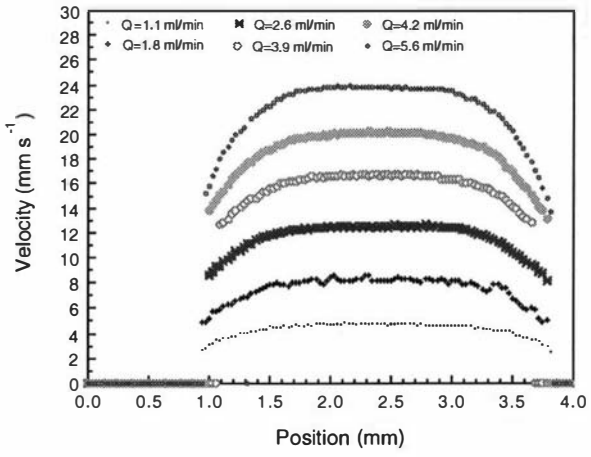

Figure 5.11: The velocity profiles obtained across the 2.6 mm ID capillary tube reveal a discontinuity next to the capillary wall. This 'step' is observed for all the measured flow rates to as low as 1.10 ml min^{-1} ($\dot{\gamma}_w$ =10.6 s^{-1}).

rates and can be more clearly seen in figure 5.12 where the velocities have been normalised to the maximum velocity of each profile. A slip velocity of around 0.6 of the maximum velocity and a constant profile shape is obtained for all flow rates. An analytical expression for the velocity distribution in capillary geometry here can be derived from the constitutive equation as described with Eqn. (3.66). The shape of the flow curve is expressed by the value of the power law exponent as seen in figure 5.13. A value of n=0.4 was obtained after a constant value of 0.6 of the maximum velocity had been added to the powerlaw data which was renormalised to incorporate slip. This powerlaw exponent is consistent with both the cone-and-plate rheometry viscosity measurements (refer to page 69) and cylindrical-Couette velocity distribution measurements (refer to page 74).

De Vargas et al[23] reported a variation in the slip velocity as a function of $\frac{l}{D}$ in which measurements were made using a contraction ratio range of 26 to 80. The slip velocity variation appeared asymptotic with increasing wall shear stress, a behavior thought related to where entrance effects become absent and the velocity profile steady. This phenomenon occurs for $\frac{l}{D} \geq 400$. To establish whether similar end effects were detectable by velocity measurements along the 2.6 mm capillary tube (ie. by varying $\frac{L}{D}$), velocity profiles were obtained at a fixed flow rate over a range of L values. Figure 5.14 shows such profiles for a single flow rate of around 5.0 ml min^{-1} ($\approx$ 50 s^{-1}) and a contraction ratio of $\frac{W}{D}$ = 15.4. Even with a large change with $\frac{L}{D}$ of 79 to 214, no appreciable difference in the

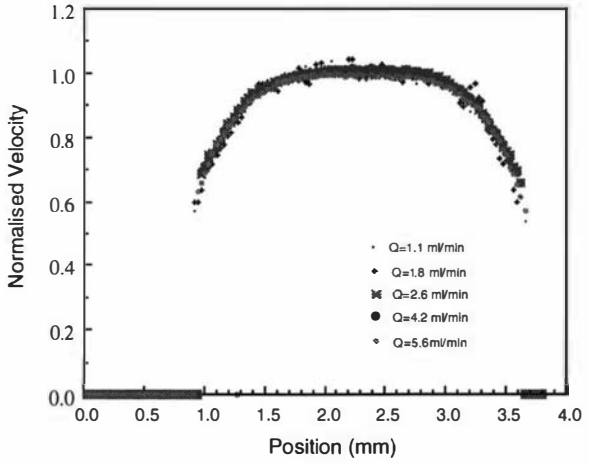

Figure 5.12: The normalised velocity distribution across the capillary reveals a consistent magnitude of slip of around 0.6 of the maximum velocity is obtained as well as consistent shaped profile.

normalised velocity distribution is apparent. A similar behavior is observed for each individual $\frac{L}{D}$ for varying flow rate. There exists an apparent contradiction with de Vargas et al work. It must be emphasised a direct comparison can only be made if different length tubes are attached when measuring the velocity profile. In the work presented here we vary $\frac{L}{D}$ whereas de Vargas et al vary $\frac{l}{D}$. A similar comparison of normalised velocities for different flow rates and varying $\frac{L}{D}$ for a 5.0 mm ID capillary tube also revealed no significant change. However inspection of the magnitude of slip for these flow profiles compared to the 2.6 mm ID capillary tube did show subtle differences. Figure 5.15 shows a smaller fractional slip velocity of 0.5 is found for a smaller reservoir contraction of 8 (ie. $\frac{W}{D}$=8). As the velocity profiles are independent of $\frac{L}{D}$, it is not important where along the 2.6 and 5.0 mm pipes the normalised velocity comparisons are made. However to complicate matters less, similar $\frac{L}{D}$ ratios have been compared.

With change to a smaller diameter reservoir, which could now fit *inside* the gradient coils, a velocity profile could be obtained closer to the entrance of the tube. Thus a closer inspection could be made of entrance effects, if any. With the new reservoir, an $\frac{L}{D}$ ratio as small as 16 was now possible. The dimensions of the reservoir (30 mm OD, 20 mm ID) also gave a smaller contraction ratio of $\frac{W}{D} = 4$. As in the case when $\frac{W}{D} = 15.4$ and $\frac{W}{D} = 8$, varying both the flow rate and $\frac{L}{D}$ again showed no change in the normalised velocities. In contrast a comparison of flow profiles obtained with the new and previous $\frac{W}{D}$ ratios again gave significant differences. These differences were apparent in the amount of slip *and* in the shape

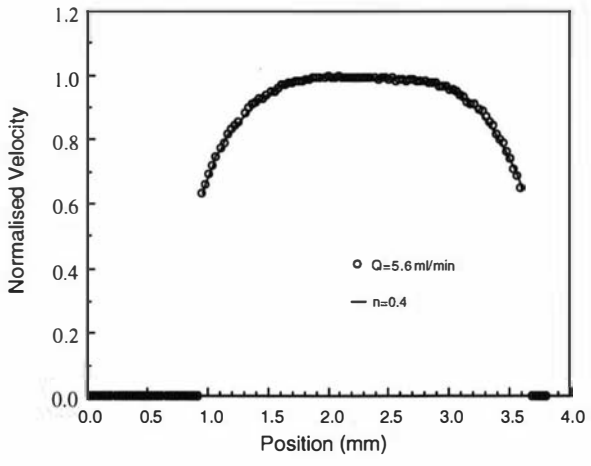

Figure 5.13: The power law behavior of Xanthan gum, consistent with other findings in section 5.2 and 5.3, is observed when the capillary normalised velocity distribution is fitted with the analytical data, which includes slip. Again a consistent power law exponent of 0.40 is obtained.

of the flow profile. As seen in figure 5.15 a lower slip velocity of around 0.3 of the maximum velocity was observed for the smallest contraction. A direct comparison of the shape of the velocity profile obtained for the smallest $\frac{W}{D}$ cannot be made in figure 5.15 as the diameters of the different pipes used, have not been normalised. This problem was overcome by fitting the velocity profile with a generated power law velocity profile. A lower power law exponent of 0.25 (Fig. 5.16) was obtained. The difference in this profile shape has been attributed to the late attainment of the data. Eight weeks elapsed between the collection of the previous data and the data collected for $\frac{W}{D} = 4$.

To increase the flow rate a Gilson peristaltic pump was used to pump the previously gravitated Xanthan solution. As figure 5.17 shows the use of this pumping system abolished the slip. A possible cause for the slip absence may be due to the mastication action of the pumps feeder head or the shearing caused by the pipe at larger flow rates.

0.2 % (w/v) solutions of the 'Kelsan' and 'Aldrich' produced Xanthan were also prepared and pumped through the same capillaries as the Unam gum experiments. Under the same conditions no slip was found at any flow rate, $\frac{W}{D}$ and $\frac{L}{D}$ combination (refer to Fig. 5.18).

The principal findings of rheometric capillary experiments, based on the Mooney

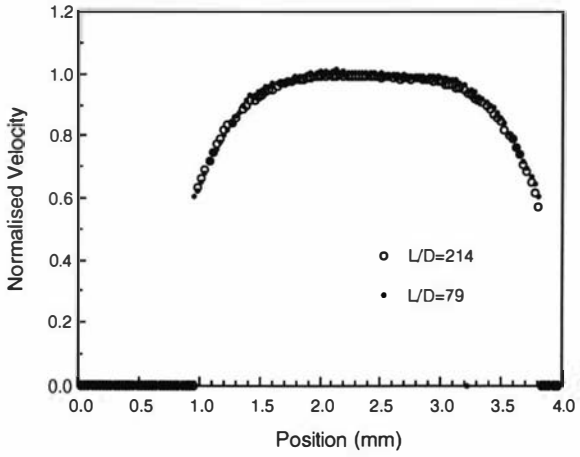

Figure 5.14: A comparison of the normalised velocity profiles obtained at different positions along the pipe, for the same flow rate, do not reveal any appreciable difference. This similarity is true for both magnitude of slippage and overall profile shape.

analysis, are shown in figure 5.19 where the slip velocity is plotted as a function of wall stress. Estimated slip data obtained from the imaging experiments have been added by Rod Lambert[6]. The wall stress was determined by assuming a power law constitutive relation, using the results of viscometry and flow profile fitting, and assuming the wall stress was the same as when the fluid was not slipping.

[6]Massey University, Palmerston North, New Zealand.

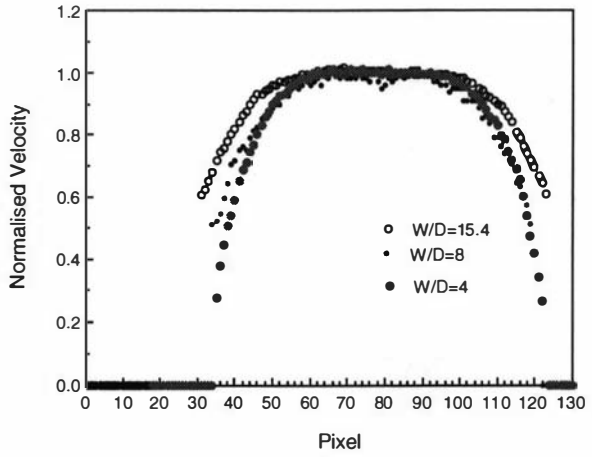

Figure 5.15: In comparing the normalised velocities of different $\frac{W}{D}$ contraction ratios a difference in the magnitude of the slippage is found. Comparison of the profile's shape cannot be made in this plot as the diameters of the profiles have not been normalised.

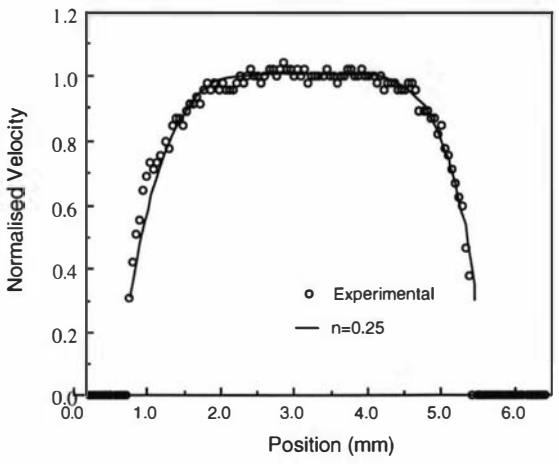

Figure 5.16: A lower powerlaw number of 0.25 and a smaller degree of slip is found for the flow profile with the lowest contraction ratio of $\frac{W}{D} = 4$.

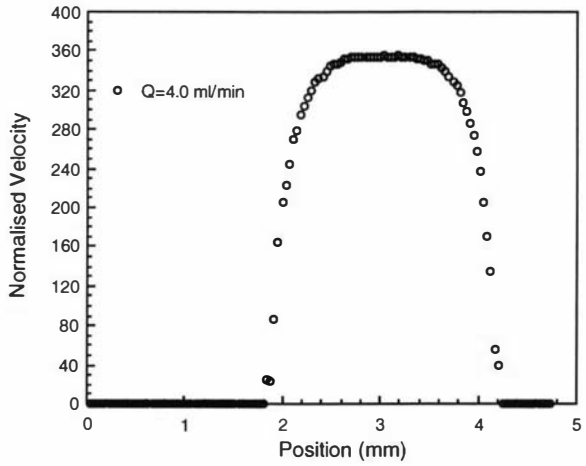

Figure 5.17: To achieve higher shear rates the Unam solutions were pumped using a peristaltic pump. In doing so the slip behavior was abolished.

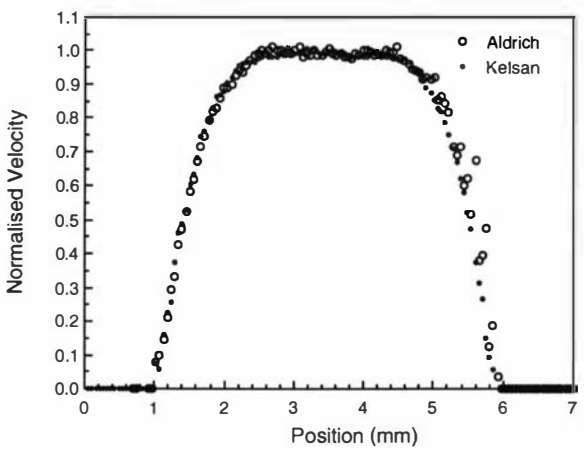

Figure 5.18: Both of the lower molecular weight fraction Xanthan polymer solutions did not exhibit slip when pump through the same pipe conditions.

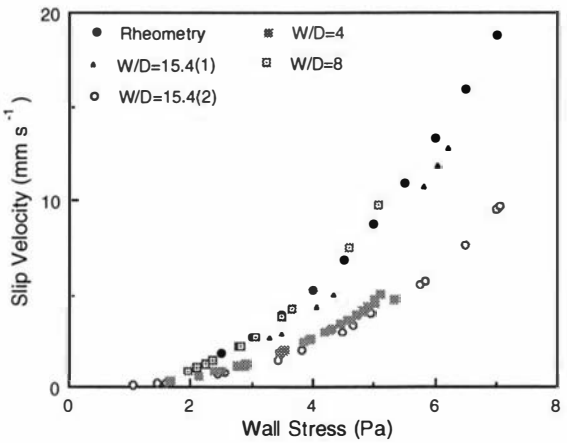

Figure 5.19: A summary of both the rheometric and imaging capillary experiments suggest the slip velocity is not dependent only on the wall stress.

5.4.3 Discussion

In summary, the data presented here show substantial slip for dilute Unam Xanthan solutions. Comparison with previous studies by de Vargas et al show a sharp contrast as no flow development along any of the capillary tubes for any flow rate was found. This lack of change is consistent even when the position of the velocity profile is selected at a distance from the entrance as low as $\frac{L}{D} = 16$. Clearly the major influence, according to figures 5.15 and 5.16, to the velocity profile is the contraction ratio to the entrance to the capillary. For contraction ratios of 4, 8 and 16, the fractional slip velocities are approximately 0.3, 0.45 and 0.6 respectively. It appears that as the contraction ratio of the reservoir increases, more slip is evident. Another equivalent explanation for this observation could be that as the pipe diameter increases, as is the case when changing from $\frac{W}{D} = 15.4$ to $\frac{L}{D} = 8$, the stress experienced at the tube wall is smaller. This trend in capillary diameter cannot be observed with the lowest contraction ratio but the lower slip velocity could be attributed to the different Xanthan solution used. This is in line with the Mooney assumption that the slip velocity depends only on the wall stress and thus could be seen as justification of the Mooney assumption. In support of this interpretation, figure 5.19 shows an agreement of the slip velocities obtained for $\frac{W}{D} = 15.4(1)$, $\frac{W}{D} = 8$ and the capillary rheometer data. The NMR data was collected on the same day using the same solution but two different capillaries. In contrast data is in disagreement using the same tube but different reservoirs ($\frac{W}{D} = 8$, $\frac{W}{D} = 4$). According to Mooney one would expect similar wall stresses for the different reservoir contractions and thus comparable slip velocities. It is noted that one solution was used to obtain the larger contraction data and another two solutions, prepared weeks apart, were used for the smaller contractions. In addition, another data set collected at the largest reservoir contraction ($\frac{W}{D} = 15.4(2)$) does not agree with any previous data. Thus in terms of the Mooney theory the interpretation of our results remains unclear.

The accuracy of the determination of the slip velocity must be highlighted. As other authors have suggested, the thickness of the depletion layer is on the order of 300 nm[31]. Some doubt as to the magnitude of the slip velocity arises since the imaging resolution used in this work was 30 μm. Thus the pixel of the velocity profile closest to the edge of the wall is determined by the signal obtained from the depletion layer, bulk fluid and the lack of signal from the glass capillary. The data processing technique chooses the highest velocity signal within the pixel. Thus if any bulk fluid signal is present within the pixel, a higher slip velocity will be obtained. Noise from signal-free regions will also add further complication to the velocity profile. Whether these anomalies are the cause for the varying slip

velocities found in figure 5.19 is doubtful. Such errors would manifest themselves as random occurences and not systematic.

GPC data suggest that the slip phenomena may depend upon the majority of the polymer being at a high molecular mass since peristaltic pumping of the solutions resulted in slip being abolished. This high mass dependence is supported by Aldrich and Kelsan Xanthan, which did not exhibit slip, having a larger percentage of their mass in the low molecular mass regime. The Xanthan polymers which did not exhibit slip had a slightly lower power law index of 0.36 but revealed a markedly different dynamic response when compared to the Unam polymer. Both the storage and loss modulus was half of the slipping Xanthan. The phase difference is the same for all Xanthan polymers at around 20°.

Another possible explanation in determining slip, associated with molecular properties, could be flow-induced molecular alignment. This process could be caused by extensional flow and elastic effects at the entrance contraction. As the extensional strain rates are larger in the center of the pipe, one would expect a high degree of molecular order in the bulk of the fluid. Whereas closer to the tube walls a more random molecular orientation might be expected. As a consequence the shear viscosity might be comparatively low near the wall surface leading to a high shear rate-slip regime.

To investigate whether molecular orientation effects are dominant in our measurements, it is helpful to calculate the magnitude of the Péclet number, $\dot{\epsilon}\tau_r$. $\dot{\epsilon}$ is the local extensional strain rate and τ_r is molecular rotational correlation time for a Xanthan rigid rod. Where extensional strain rates exceed the time for the rod to re-orientate itself, ie. $\dot{\epsilon}\tau_r \geq 1$, molecular alignment might be expected to occur. Estimates of $\dot{\epsilon}$ for the largest contraction ratio and larger flow rates are of the order of 10 s^{-1}. The molecular rotational correlation time can be estimated with the knowledge of the translational diffusion coefficient, D_s, for a known rod length, L, at infinite dilution[38]. This result leads to:

$$\tau_r \simeq \frac{L^2}{18D_s} \tag{5.1}$$

The length and diffusion coefficient of the Xanthan solution used here can be calculated by the data of Coviello et al[94]. 3×10^6 da Xanthan in water gives a correlation time of around 0.1 s. Thus the Péclet number would appear to approach, if not exceed, unity for the flow rates where slip is observed. Further, we note as $\dot{\epsilon}$ increases, a process which occurs as the contraction ratio is increased, the degree of slip increases. Furthermore, as previous data suggest slip is sensitive to molecular size, a fact not surprising given that $\tau_r \sim \frac{L^3}{\ln(L)}$[38].

It must be emphasised the above molecular alignment postulate is highly spec-

ulative. The exact nature of slip is very dependent on the nature of sample preparation, even when the sample has been obtained from the same batch. Further experiments were tried investigating the contraction ratio hypothesis by constructing a 1.0 mm capillary insert. Not only did the arrangement give a larger contraction ratio but larger $\frac{L}{D}$ ratios were also possible. However, the next solution of Xanthan did not slip and had dynamic rheometric properties similar to that of the Xanthan destroyed by peristaltic pumping.

Although the relationship of slip velocity and wall stress is similar (Fig. 5.19) for the two capillary techniques, a substantial variability in the imaging data is unrelated to contraction ratio. Although these differences cannot be explained satisfactorily, possible causes such as sample preparation, temperature, rheometer calibration and imaging calibration are mentioned. Care was taken to standardise the samples between the collaborative groups, nonetheless it is possible that the preparations were sufficiently different to not warrant a comparison. Estimates of the wall stress for the imaging experiments were calculated using earlier rheometric data and not the data included in figure 5.19. Previous data supports the inclusion of Xanthan as being described as a power law fluid, however it may be possible the absolute viscosity values used were not those of the solutions in figure 5.19. Although the experiments were completed at different temperatures; 25°C for the Mexican group and 22°C for the New Zealand group, there is evidence that temperature effects, if any, are small[95].

The appearance of slip in the cylindrical-Couette images is of some concern for the viscometric data. Cohen and Metzner[96] suggest that slip in dilute solutions is a product of an inhomogeneous stress field. In the usual Couette rheometric devices the sample gap is small, resulting in a small stress gradient. However this is not the case with the Couette imaging rheometer we have designed, perhaps a reason why slip is so apparent in this system.

It has been suggested by Walters[97] that inconsistent results are obtained for a capillary geometry if the contraction ratio is less than 18. In contrast consistent repeatable measurements have been found below this value.

5.5 Conclusions

Dilute solutions of Xanthan gum can exhibit slip which appears to be molecular weight dependent. The fractional slip velocity appears dependent upon the contraction ratio at the capillary entrance and is independent of $\frac{L}{D}$ values in excess of 16. The magnitude of the capillary slip velocities are in line with the measurements inferred from a Mooney analysis of capillary rheometric data. Slip was also

observed in a cylindrical-Couette cell. We suggest a possible mechanism for slip may be the effect of molecular alignment caused by the extensional strain at the entrance to the capillary, but note sample preparation and other effects can also play an important role.

Chapter 6

The Spurt Effect of Wormlike Micelles

As mentioned in chapter 2, with both polymer melts and semi-dilute solutions, an explanation of spurt has been advanced by McLeish and Ball[29] based on the Doi-Edwards[38] model. In their picture the Rouse time, τ_R, and tube disengagement time, τ_d, provide two inflexions in the shear stress versus shear rate curve. Thus after a critical shear stress, σ_c, the shear rate will be multi-valued. Both of the characteristic times τ_R and τ_d are strongly dependent on molecular mass (M^3 and M^2 respectively). Any polydispersity will smooth out the constitutive relation, masking the underlying double valued-ness. This reason may be why such observations have been somewhat elusive with high molecular weight polymers.

'Wormlike micelles' provide an alternative candidate for investigation into spurt phenomena. The micelles are known to exhibit strong non-linear behavior (refer to Sec. 2.4.4) but with a narrow distribution of relaxation times. The narrowness of this distribution suggests that the spurt effect might be more easily observed in these systems than in high molecular weight polymers where polydispersity is unavoidable.

6.1 Cetyl Pyridinium Chloride/Sodium Salicylate Micelle

6.1.1 Structure

The structure of both components contained in the Cetyl Pyridinium Chloride (CPyCl)-Sodium Salicylate (NaSal) wormlike micelle are shown in figure 6.1. The solutions used comprise 60 mM/100 mM concentrations respectively in pure water. The CPyCl molecules are amphiphilic, having both hydrophilic and hydrophobic

character. This property causes the molecules to aggregate in micelle structure when in an aqueous solvent. The effect of the NaSal ion is to subtly modify the surface energy so as to favor aggregation in the form of long, random-coil wormlike assemblies. At the concentrations used in this work, these assemblies are entangled in the same manner as covalently bonded random-coil macromolecules above the entangled concentration, c^*. There is, however, one major difference. The wormlike surfactant assembly is a 'living' polymer and is subject to rapid breakage and reformation. This property has the effect of internally averaging chain length polydispersity, thus leading to a mono-exponential stress relaxation behavior characterised by the geometric mean, $(\tau_b \tau_d)^{\frac{1}{2}}$ where τ_b is the breakage/reformation time.

Above 19 °C the solution is transparent and homogeneous. Below this temper-

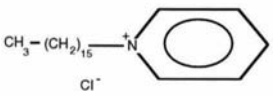

Cetyl Pyridinium Chloride

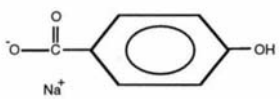

Sodium Salicilate

Figure 6.1: The wormlike micelle used in this work is comprised of two surfactants, namely Cetyl Pyridinium Chloride and Sodium Salicylate. The hydrophobic and hydrophilic ends of the molecule arrange themselves to form complex polymer-like aggregates.

ature it is a 'milky' white and inhomogeneous. This change has been associated with an apparent phase change for which light is strongly scattered in the lower temperature phase.

6.1.2 Rheology

6.1.2.1 Strain-Controlled Experiments

An investigation of the rheological behavior of the CPyCl/NaSal micelle was carried out at Cambridge University[1] by Dr Bas Smeulders using a 25.0 mm OD Rheometrics RDSII cone-and-plate *strain*-controlled rheometer. All experiments were performed at 25.0 °C, above the micelle's phase change temperature.

[1] Department of Chemical Engineering, University of Cambridge, England.

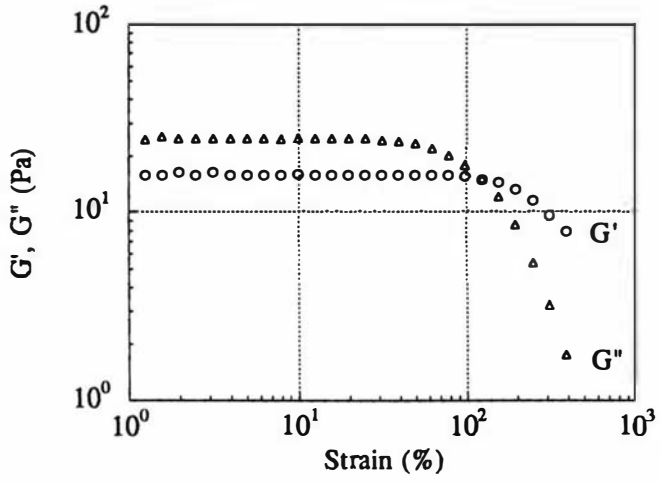

Figure 6.2: The linear-strain behavior of the wormlike surfactant revealed a 30% strain could be achieved before entering a regime of non-linearity.

To investigate the extent of the linear strain region of the micelle, dynamic strain sweep experiments were conducted at a fixed frequency of 1.0 rad s^{-1}. From figure 6.2 it can be seen that up to strain amplitudes of 30 %, the fluid has a linear behavior.

A frequency sweep experiment (Fig. 6.3) was also carried out at 20 % strain amplitude. The fluid shows typical Maxwell fluid behavior with dominant viscous behavior at low frequencies and G' having a constant value after the G'-G'' crossover frequency of 0.1 Hz. The frequency sweep data was fitted with a generalised Maxwell model (Eqns. (2.12) & (2.13)). Optimal fitting was achieved with six G relaxation times. The linear viscoelastic behavior is dominated by a relaxation time of 2 s. No other times above this relaxation time were found but a series of important times were found between 1-10 ms. An effect of the second group of relaxation times can also be seen in the frequency sweep data where an up turn of G'' can be seen (Fig. 6.3).

The non-linear behavior was investigated by stress relaxation experiments for

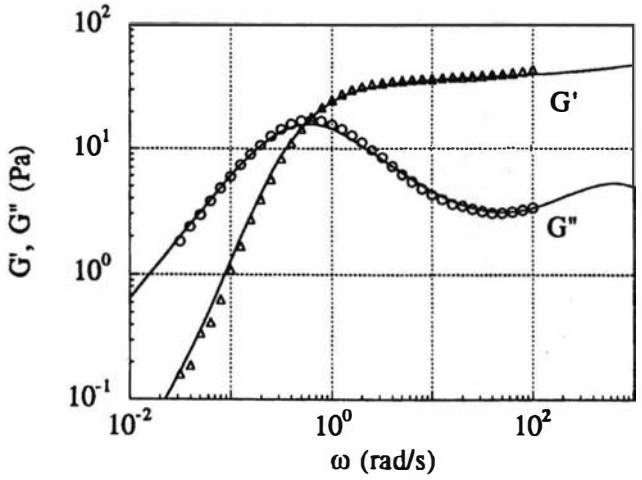

Figure 6.3: A typical Maxwell type fluid shows the characteristic 'flattening' of G' at high shear rates with dominant viscous behavior at the low strain rate spectrum.

strains ranging between 20 and 500 %. This data can be seen in figure 6.4 where at strains of 20 %, a linear response of the relaxation modulus is observed. An increase in strain shifts $G(t)$ progressively downwards. Below 0.5 s, $G(t)$ does not maintain the shape of the curve fully, so separability of strain with time is not entirely obeyed. The plot of Ln$[G(t)]$ versus strain, at t=2.0 s, has a slope of k=0.33±0.01. The straight line nature of this plot shows that k is not strain dependent, as required by the Wagner model.

Steady shear experiments (Fig. 6.5) reveal a near-Newtonian behavior at shear rates below 0.1 s^{-1}. The material is in fact characterised by a power law exponent of around 0.85 but this region will be referred to as the near-Newtonian region. Above a critical shear rate the shear stress became roughly independent of shear rate. This behavior is very reproducible but investigation at shear rates above 50 s^{-1} proved difficult as the sample was expelled from the rheometer. Using the Maxwell-Wagner constitutive equation (Eqn. (2.17)) the Newtonian behavior observed at low shear rates agrees well with the limiting case of $k = 0$. With a

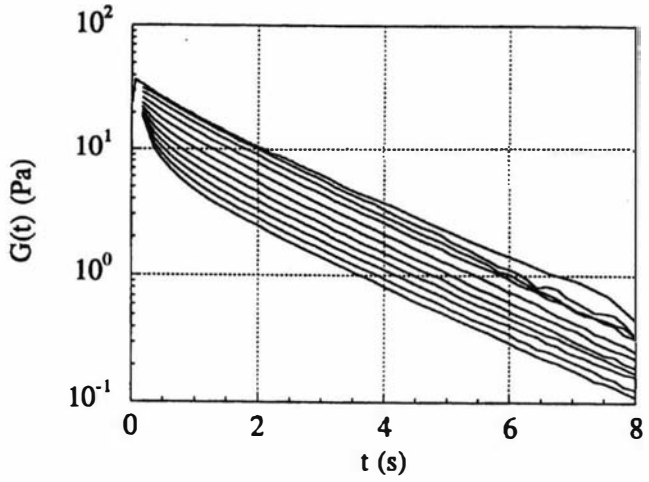

Figure 6.4: Care must be taken while measuring damping coefficients to avoid regions where the strain is time dependent. To ensure this criterion was met, measurements were taken at t=2.0 s.

Wagner damping coefficient of $k = 0.32$ the calculation predicts a maximum shear stress but only agrees with the experiment quantitatively. An unstable flow would result at the corresponding shear rate with a resulting discontinuity as seen in Fig. 6.5.

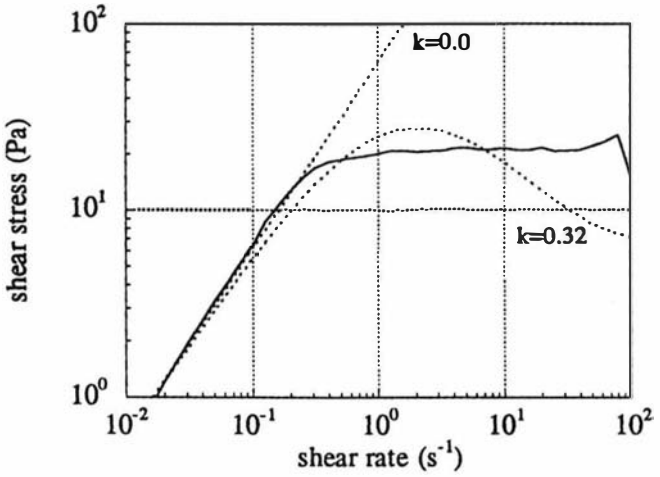

Figure 6.5: At a critical shear rate the shear stress of the material seems independent of shear rate. Before this regime a short 'shear thinning' period is observed characterised by the non-linear nature of the flow curve.

6.1.2.2 Stress-Controlled Experiments

As in the previous section, stress experiments were also carried out at Cambridge University with a Rheometrics DSR *stress*-controlled rheometer. Shown in figure 6.6 is the comparison of the stress and strain constant shear experiments. At low shear rates the agreement is good with the stress-controlled experiments showing a slightly larger stress value at high shear rates. Again at low shear stresses a Newtonian region is seen with a zero-shear viscosity of 70±5 Pa s. A short shear thinning region is also established before a critical shear stress (26±1 Pa) is reached after which there is a multi-valued shear rate. The lower shear rate is on the order of 1 s^{-1} (0.8±0.2 s^{-1}) and the higher 50 s^{-1} (40±20 s^{-1}). The reproducibility of the fast increasing shear rates after 26 Pa is consistently between 1 and 10 s^{-1}. Further increase in the shear stress produces an increase in the shear rate. Finally there is a small decrease around 80 s^{-1}. However there is some doubt with this last region as the sample was expelled at the corresponding shear rate.

The disagreement between strain and stress experiments at larger shear stresses demonstrates the instability in the flow after exceeding the critical shear stress of 26 Pa. This instability was even more evident when the same experiment was carried out at 20 °C as shown in figure 6.7. The strain-controlled experiment shows a pronounced maximum whereas the stress-controlled experiment only shows a fast increase in shear rate. Shown also is the Maxwell-Wagner constitutive relationship with $k = 0.32$.

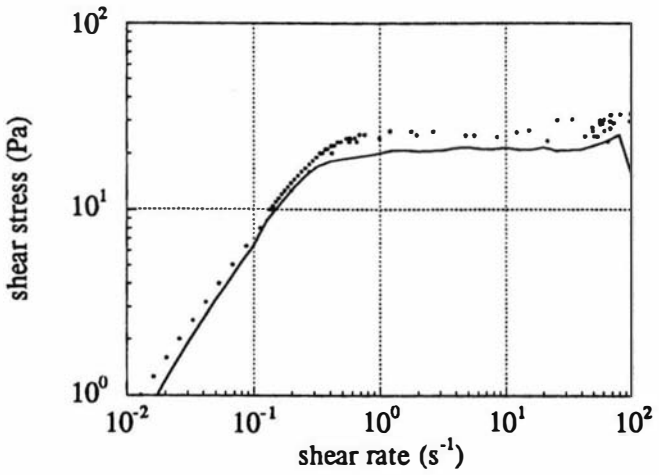

Figure 6.6: The compliance between the stress (dots) and strain-controlled (line) data is good at low strain rates. The intrinsic instability of the flow is evident with the disagreement of the data at higher shear rates.

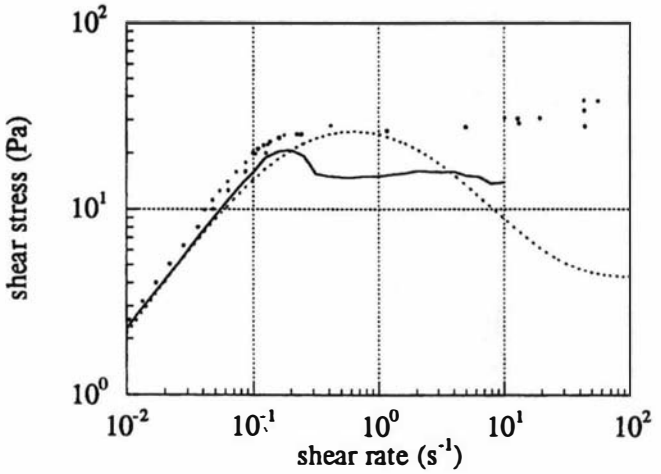

Figure 6.7: Instability in the flow behavior is even more pronounced when stress-controlled (dots) and strain-controlled (line) experiments are compared at 20 °C. Again agreement of the two data sets is good at low shear rates.

6.2 Determination of Flow Curve Using MRI

The relationship between shear stress, σ, and shear rate, $\dot{\gamma}$, can be expressed as some function of shear rate as follows:

$$\sigma = f[\dot{\gamma}] \tag{6.1}$$

Hence we may write the shear rate as some inverse function of shear stress (Eqn. (6.2)). For a capillary of length, l, and pressure difference, ΔP, between its ends, the shear stress has a linear relationship with tube radius, r, namely $\sigma = \frac{\Delta P r}{2l}$.

$$\dot{\gamma} = f^{-1}[\sigma] \tag{6.2}$$

$$\Rightarrow \quad \frac{\partial v}{\partial r} = f^{-1}\left[\frac{\Delta P r}{2l}\right] \tag{6.3}$$

The linear dependence of shear stress on radius for capillary flow is of particular importance as it enables the flow curve across the tube to be calculated from the velocity profile across the tube. If $\frac{\Delta P r}{2l}$ is measured in the experiment then the flow curve will be absolute in both σ and $\dot{\gamma}$. If the pressure gradient is unknown then σ will be arbitrarily scaled.

The velocity profile can also be obtained (refer to Callaghan et al[98]) from equation (6.3) by integrating it with respect to r as seen in equation (6.4).

$$v(r) = \left[\frac{\Delta P}{2l}\right]^{-1} \left\{ \int_0^{\frac{\Delta P}{2l} R} f^{-1}[\sigma] d\sigma - \int_0^{\frac{\Delta P}{2l} r} f^{-1}[\sigma] d\sigma \right\} \tag{6.4}$$

Thus by calculating the area under the scaled flow curve, the velocity profile can be calculated. Equation (6.4) implies knowledge of the constitutive relationship of σ with $\dot{\gamma}$ will lead to the calculated velocity profile.

6.3 Velocity Measurements

6.3.1 Setup

A sample of wormlike surfactant was prepared by mixing 100 mM Cetyl Pyridinium Chloride (CPyCl) and 60 mM Sodium Salicylate (NaSal) with distilled water. The mixture was allowed to stand for a few days to enable the air bubbles to escape.

All NMR work reported here was conducted at 25 °C, well above the CPyCl/NaSal micelle phase transition temperature of 19 °C.

The solution was passed through a 5.0 mm ID capillary tube attached to a 40.0 mm ID reservoir. Further detail of this capillary system can be found in section 3.4.1. The solutions were contained in a closed loop system and driven by a Gilson

Minipuls 3 peristaltic pump. This type of pump was used as it enabled sufficiently large flow rates. The eight rollers in the pump's drive head kept flow pulsation to a minimum. An air gap of approximately 2.0 cm at the top of the reservoir dampened whatever small pulsation might have remained. Because of the nature of the peristaltic roller action, the fluid was not swept at a constant volume rate but allowed a certain amount of 'slippage' and backflow. Instead the flow rate was controlled by the amount of pressure which the pump could obtain in the reservoir head. Thus the experiment was stress-controlled not strain-controlled.

To minimise end effects in the capillary, velocity measurements were obtained between 0.5 and 0.6 m from the entrance of the 5.0 mm ID tube. Volume flow rates were determined from a knowledge of the cross-sectional area of the tube and the velocity profile obtained by NMR.

The full details of the method in which the velocity profile was obtained can be found in section 3.2.3.1. The **q**-gradient was stepped and 8 **q**-slices used to obtain the phase evolution of the spins. In the work reported here the **q** gradient had a duration around 1 ms and magnitude approximately 0.5 T m^{-1}. These gradient values were changed frequently throughout the experiment to optimise the sensitivity to velocity and diffusion. A field of view of 6.0 mm ensured the complete cross section of the capillary tube was imaged.

It should be noted that the NMR signal is obtained from the protons in the water solvent. Because these protons have a long spin-lattice relaxation time, sufficient spin recovery time had to be allowed. Even with a long repetition time, signal-loss is unavoidable. To enhance the signal-to-noise ratio of the images we employed azimuthal averaging of the pixels. This required careful alignment of the edges of the tube within the image so pixel smearing was avoided. This process was achieved by the computer software *Image Show* (refer to section 3.3.1).

To ensure our confidence in the accuracy of the velocity measurements a *Pharmacia 500* twin syringe pump was also used. The flow rate of this system was not as large as with the peristaltic pump but, because of the syringe action, accurate low flow rates were possible. Thus comparison of the calculated flow rates from NMR measurements with a flow rate set by the syringe pump can be achieved. Also the accuracy and effect of pulsation of the peristaltic pump can be tested by comparing set flow rates, with NMR measurements, from both systems.

6.3.2 Results

A set of six diametral velocity profiles, $v(r)$, are shown in figure 6.8. The flow rates, achieved by both the Pharmacia and Gilson pumps, range from a minimum of 0.22 ml min^{-1} to a maximum of 2.10 ml min^{-1}. At the lowest flow rate the

velocity profile is parabolic, a characteristic of Poiseuille tube flow for a Newtonian fluid. At a flow rate of around 0.4 ml min^{-1} a deviation of the velocity's parabolic shape next to the tube walls is seen resulting in an enhanced wall shear rate. For example, at a flow rate of 0.45 ml min^{-1} a shear rate of around 0.7 s^{-1} is found. This behavior is consistent with the formation of a weak 'shear band' as the effect is confined to a well defined band of radius within the tube.

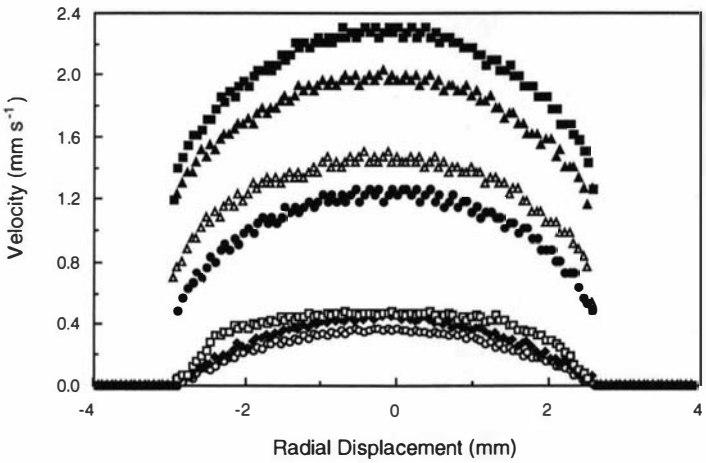

Figure 6.8: Seven flow rates: 0.22, 0.30, 0.38, 0.99, 1.2, 1.5, 2.1 ml min^{-1} were measured across the 5.0 mm ID capillary tube. For low flow rates, a near-Newtonian behavior is noticed in which a Poiseuille velocity distribution spans the capillary tube. At a critical flow rate regime the flow profile reveals a characteristic discontinuity where an enhanced shear rate is observed close to the capillary wall, a phenomenon termed 'the spurt effect'.

To investigate closely the transition from the Newtonian flow to 'spurt' flow, figure 6.9 contains a set of four normalised velocities. The azimuthal averaging technique mentioned before has been employed with these velocities. Also included in the plot is a Poiseuille velocity profile. The agreement of the calculated Newtonian profile with the low Q data is good. A maximum local shear rate of approximately 0.2 s^{-1}, next to the tube walls, is found at these low flow rates. As the flow rate is increased a delicate transition is apparent in the velocity profile. The change suddenly occurs between 0.36 and 0.40 ml min^{-1} and unstable flow is seen at an intermediate value where again a Newtonian profile best describes the distribution. This unstable flow is better demonstrated when the **q** data for this flow rate is studied, revealing a displacement spectrum whose shape is not well defined. For flow rates above 0.40 ml min^{-1} a large velocity gradient is evident next to the tube wall. This large shear rate spans only one pixel width and is not

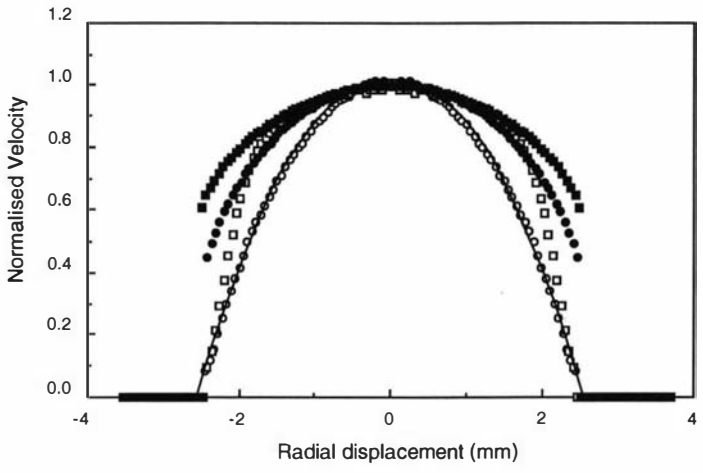

Figure 6.9: A closer investigation of the flow profiles close to the critical spurt flow rate displays changes when the velocity gradient approaches 0.2 s^{-1}. The selected flow profiles are Q=0.22 (open circles), 0.38 (open squares), 0.99 (solid circles) and 2.1 ml min^{-1} (solid squares).

distinguishable from the similar characteristic flow profile found in studying slip phenomena. A shear rate of 10 s^{-1} is found in this second flow transition and has been attributed to the discontinuity in the shear stress vs. shear rate curve.

As a further investigation into the spurt effect a glass cylindrical Couette cell was also used with the 100mM/60mM CPyCl/NaSal. A detailed description of this rheometer is given in section 3.4.2. A 2.0 mm gap between a 9.0 mm OD outer fixed tube and a 5.0 mm OD inner rotating rod was available for the sample shearing. Sample placed inside the rotating rod was not to be sheared but experience a rigid body rotation. The velocities were determined by the same **q**-slice-FFT method described earlier, with the addition of a second slice selective pulse to avoid 'fold back' when increasing the resolution. The details of this method are further described on page 73. To ascertain the precise velocity of the inner cylinder surface, an extrapolation was made from the region of rigid body rotation to the sheared region. This process is shown in figure 6.10 where a high shear region in the vicinity of 20 s^{-1} can be seen 0.15 mm from the inner rod. The other velocities beyond the boundary layer and out towards the stationary wall, all falling below 1 s^{-1}.

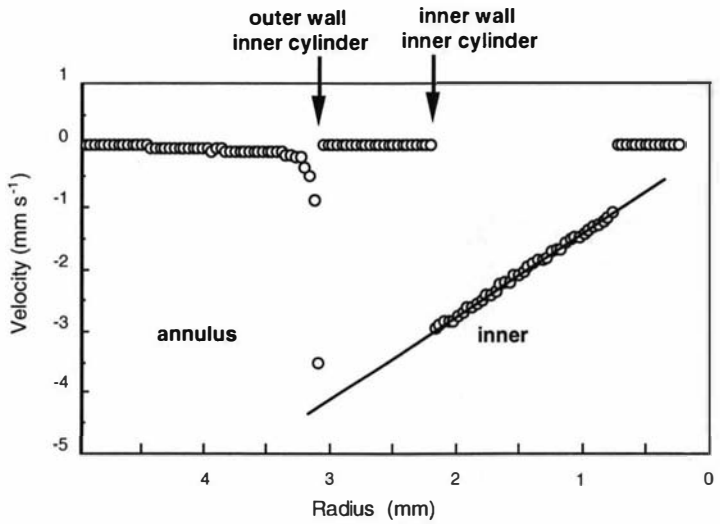

Figure 6.10: As with capillary flow studies, a high shear band is also found close to the inner rotating rod of the cylindrical Couette cell. An extrapolation from the non-sheared region, inside the inner cylinder, to the sheared region suggests the material next to the rotating surface has a common velocity with that surface.

6.3.3 Discussion

Our rheological measurements agree well with the calculations of Spenley et al[99] who suggest the critical shear stress, σ_c, is equal to 0.67 of the storage modulus plateau $G'(\infty)$. The value found for this asymptote is 37±1 Pa, implying $\sigma_c \approx$ 25±1 Pa. This value agrees very well with our observed value of 26±1 Pa. In addition the predicted shear rate for which the constant shear stress is detected is $2.6/\lambda_M$, where λ_M is the Maxwell time associated with chain breakage introduced in Sec. 2.1.1.1. If this constant is characterised by the most dominant relaxation time of 2 s, a corresponding shear rate of 1.3 s^{-1} is expected. This predicted strain rate agrees closely with that obtained from figure 6.6 and is the same order of magnitude as that found with MRI measurements (Fig. 6.8), which imply a critical shear rate of approximately 1 s^{-1}. Thus the Maxwell model and Wagner-type damping function also predicts unstable type flow is observed around 1 s^{-1}.

The agreement between stress-controlled and strain-controlled experiments can be seen at low shear rates, with differences evolving after 0.2 s^{-1} where non-Newtonian type flow is evident. Both classes of experiments show the spurt region occurring at shear rates larger than 1 s^{-1} which can be clearly observed with NMR imaging measurements.

Shown earlier in figure 6.9 is a set of four diametral velocity profiles with Q = 0.22, 0.38, 0.99 and 2.1 ml min^{-1}. The corresponding local shear rate has also been calculated by a five point velocity gradient fit algorithm and summarised in figure 6.11. Newtonian behavior is observed for these plots as a linear dependence over the capillary radius. As expected all flow rates exhibit a linear dependence below $\dot{\gamma} = 0.2\ s^{-1}$. For the lowest flow rate this dependence is observed all the way across the capillary tube. At Q = 0.38 ml min^{-1}, the local shear rate exceeds 0.2 s^{-1} and discloses a strong non-linear dependence while approaching the critical spurt strain rate of 0.8 s^{-1}. This shear rate reliance is clearly evident with the corresponding velocity profile showing the development of a Newtonian to non-Newtonian distribution. The absence of wall slip in this profile is due to $\dot{\gamma} < 0.8$ s^{-1}. For flow rates of 0.99 and 2.1 ml min^{-1}, the shear rate does exceed 0.8 s^{-1} close to the walls and slip is visible for which a strain rate of 10 s^{-1} is found. This high Q data also reveals a transitional range between 0.2 and 0.8 s^{-1} where a regime between Newtonian and slip behavior exists.

To illustrate the good agreement of flow curves obtained from rheology and MRI measurements, we superimpose in figure 6.12 the directly measured σ versus $\dot{\gamma}$ curve and that obtained indirectly from the MRI data. Apart from Q=0.38 ml min^{-1} the data agrees very well. This disagreement has been attributed to unstable flow conditions associated with the spurt effect. An apparent pressure variation

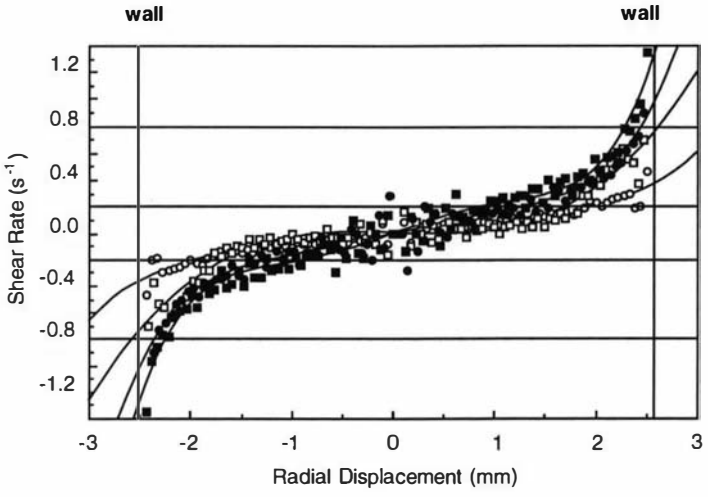

Figure 6.11: The calculated local shear rate across the capillary tube again quantitatively demonstrates the development of the flow profile as the flow rate is increased. The lowest flow reveals a strain rate lower than 0.2 s^{-1} as expected to have Newtonian behavior. The following higher Q's exhibit shear rates both above and below 0.8 s^{-1}, the former leading to spurt type flow. The order of the profiles from lowest to highest flow is 0.22 (open circles), 0.38 (open squares), 0.99 (solid circles) and 2.1 (solid squares) ml min^{-1}. The solid lines are interpolating fits for each successive flow rate.

at a specific radius has occurred and could be invoked by pressure fluctuations associated with an instability caused by differences between stress-controlled and strain-controlled conditions. Such a system exists with the peristaltic pump used here as the exact category of flow is unknown.

The velocity data, calculated from equation (6.4) and incorporating the flow curve of figure 6.12, show good agreement with the velocity profile measured by NMR (Fig. 6.13). Because the flow rates correspond to experimental and theoretical flow rates we choose to express the velocities normalised to enhance the comparison. All except Q=0.38 ml min^{-1} show quite good agreement.

It is clear that the narrow shear bands measured by NMR velocity imaging are consistent with rheological measurements. It is also evident that the spurt effect studied here is very different from conventional slip described in the previous chapter. For example, spurt requires a characteristic critical stress behavior, while the high shear rate exists over a finite region. A demonstration of the narrowness of the band can be seen in figure 6.9 where a one pixel spread of the shear band,

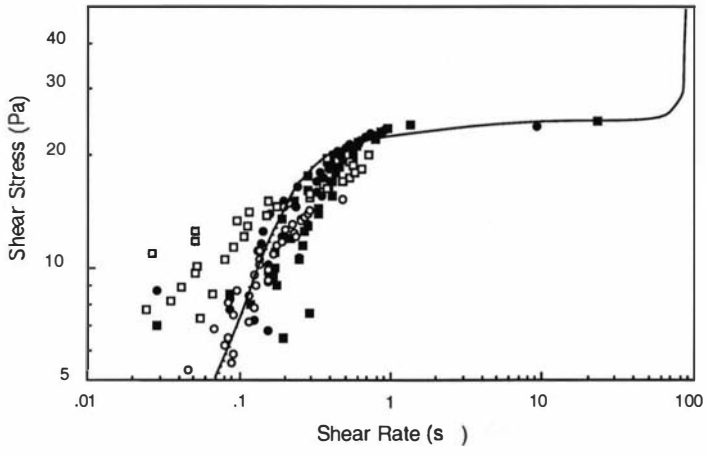

Figure 6.12: The agreement with measured rheological flow curves (Fig. 6.5, solid line) and flow curves calculated by velocity measurements are good. The stress data has been scaled arbitrarily, so as to make a realistic comparison. Q=0.22 (open circles), 0.38 (open squares), 0.99 (solid circles) and 2.1 (solid squares) ml min^{-1}.

or roughly 2 % of the tube radius, can be seen. A similar percentage width is observed with the cylindrical-Couette measurements. These latter measurements clearly show that the behavior is very different from slip, as the material next to the inner rotating rod is moving with the same speed as the rod itself.

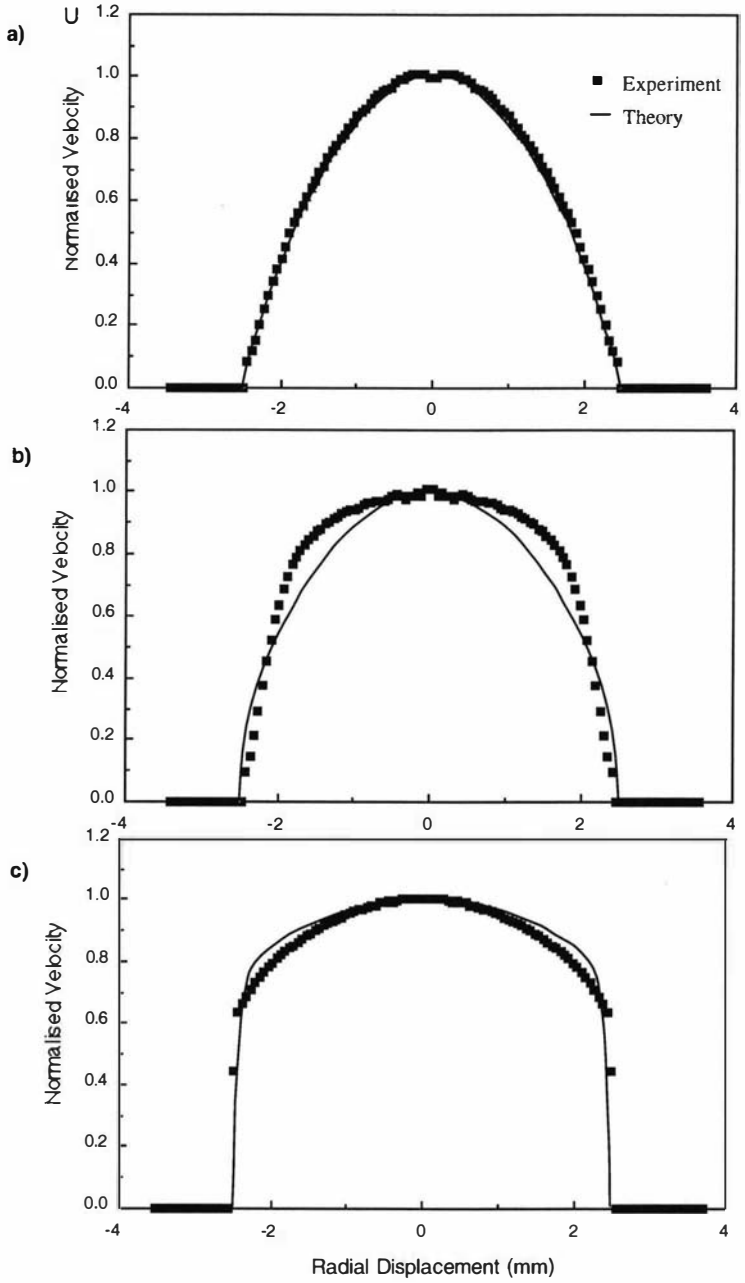

Figure 6.13: The fitted velocity profiles were calculated from Eqn. (6.4) using figures 6.2 through 6.6. The agreement is quite good remembering the flow profile obtained for 0.38 ml min^{-1} is measured around the unstable transition shear rate of 0.8 s^{-1}. Again the order of the three flow rates, from lowest to highest flow rate is (a) 0.22, (b) 0.38, and (c) 2.1 ml min^{-1}.

6.4 Conclusions

We have demonstrated the spurt effect for wormlike micelles using NMR imaging methods. To date this type of investigation is the first of its kind. A clear link has been suggested between conventional rheology methods and new methodologies based on velocity profiling. This type of association has been supported in two ways. Firstly, the agreement of the scaled stress vs. strain rate data, calculated from velocity profiles, and rheometry data. Secondly, the quantitative agreement of the velocity profile data calculated from previous rheometry measurements. The collection of *absolute* stress vs. strain data would be ideal but as yet has eluded our investigation here because of the difficulty in obtaining pressure data while measuring the velocity profiles.

The small anomalies presented in this work, for example the comparison of the calculated and measured velocity profiles, could be explained by the experiment possibly being both stress *and* strain controlled. This effect is thought to arise from the unique pumping action of the roller head.

Finally we have shown here that a comparison of results obtained from Couette and pipe geometries can be very helpful. In particular, the Couette data here demonstrates clearly the difference between apparent wall slip and shear banding in the bulk of the fluid. For the wormlike surfactant system it is the latter phenomenon which is observed. This is in sharp contrast to the Xanthan gum solutions where the Couette experiment clearly indicated apparent slip.

Chapter 7

Mobility of Polyolefins

The larger fraction of polyolefins (C_{10} to C_{18}) produced by Shell, known as *Carishop*[1] polymers, represent a new and exciting area of polymer engineering, posing typical problems of linearity, dispersity and stereospecificity. Factors important in their design include length, dispersity and stereospecificity. The side chain branches in these polymers result in desirable physical properties, in particular viscosity and melting point characteristics. Their viscous properties are however not well understood in terms of macromolecular structure and more information is needed at a molecular level, for which NMR offers a possible key. More specifically a variable temperature rheometric cell has been designed with both cylindrical Couette and cone-and-plate capabilities for operation in a 200 MHz magnet. T_2 and T_2^* relaxation times offer information concerning mobility of Carishop samples in order to explain various scaling laws of viscosity under shear. A *power law* fit is used to describe this scaling and experimental comparisons are made with previous studies at K.S.L.A.[2]

7.1 Polymerisation of Carishop Polymers

The polymerisation of polypropylene is well understood in both stereochemistry and physical properties. A Ziegler-Natta catalyst system consisting of di-ethyl aluminum chloride (DEAC) , tri-ethyl aluminum (TEA) as a co-catalyst and para-ethoxy ethyl benzoate (PEEB) as a soluble control agent are used. The differing molecular weights are controlled by TEA concentrations although similar dispersities are achieved with this method.

A similar approach has been taken with the production of Carishop polymers.

[1] Carishop ≡ Cari(Shell)(Higher)(Olefin)(Production).

[2] K.S.L.A. ≡ Koninklijke Shell Laboratorium Amsterdam.

The insertion polymerisation utilising a reactive transition metal M and growing chain P of these higher monomers produces side branches whose length is equal to the monomer length minus two. Two typical reactions are shown in Fig. 7.1 for C_{10} olefins, known as primary insertion and secondary insertion. The tac-

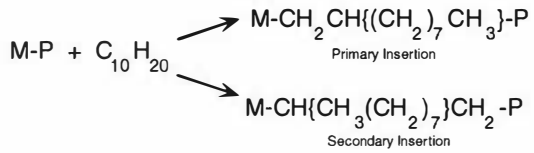

Figure 7.1: Primary and secondary insertion reaction for C_{10} Carishop polymer can lead to isotactic and syndiotactic polymer formation respectively.

ticity or stereochemistry of the backbone of these polymers can be characterised into three main types: isotactic, syndiotactic and atactic. The steric control of tacticity (isotactic or syndiotactic) is controlled partially by the chirality of the transition metal complex and partly by the approach of the monomer (primary or secondary). The four-membered ring complex active site shown in Fig. 7.2, along with the (non)hindrance observed from the substituents of the metal give rise to isotactic and syndiotactic formations respectively. The secondary reaction shown in Fig. 7.1 favors a trans (syndiotactic) formation as the opposing methyl, or R for Carishop, group on the existing chain forces the incoming R group below the plane. In contrast if the substituents of the transition metal were altered to produce a larger 'bulk' below the plane than above, the incoming R group would then be forced above the plane in a cis formation (isotactic). The physical properties of polyolefins change dramatically with varying degrees of tacticity and the length of side branches. For example, crystalline properties are favored by an isotactic formation and shorter side branch length. The viscosity of polyolefins is another physical property related to tacticity and is equally dependent on branching. The reason for viscosity scaling with tacticity and degree of branching is still not clearly understood.

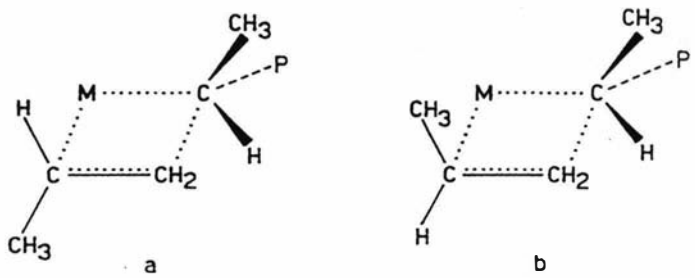

Figure 7.2: Secondary Insertion, four membered ring complex reaction for polymerisation of polyolefins produces a, (a) trans (syndiotactic), (b) cis formation, as methyl groups align to occupy maximum inhibited space.

7.2 Setup

7.2.1 Previous Results

7.2.1.1 Polyolefin Characterisation

Laboratory mini-extruder reactions of C_{12} olefins were previously completed at KSLA department (PRP/431) to give a variety of Carishop polymers with molecular weights ranging from 390 000 to 545 000 da. This was measured by conventional *gel permeatation chromatography* (GPC) in a cyclohexane solvent. Branched polymers which have the same molecular weight as a linear polymer will be of a smaller dimension, thus will pass through a GPC column slower than a linear polymer. This results in an apparent molecular weight lower than its true weight. As poly-isoprene was used as a reference standard the polyolefins' molecular weights shown in Tab. 7.1 are strictly apparent values due to their high branching content. Dynamic light scattering in conjunction with GPC provides a method of determining *absolute* molecular weights as well as normal dispersity information obtained from GPC alone. Poly-isoprene is also used in this method as a calibration standard. The GPC-light scattering molecular weights shown in table 7.1 show a large discrepancy with molecular weights obtained from GPC alone. In general the molecular weights obtained from this light scattering method show a higher molecular weight, an effect which can be attributed to the increase of entanglements with the gel in the GPC column because of high branching content in the samples, thus giving a slower flow rate. As the monomer weight for C_{10} is 140 da., the average number of carbon atoms in the backbone are also shown.

Similar molecular weights, backbone lengths and dispersities were determined

Carishop Polymer	Monomer M_w (da.)	GPC M_w (kda.)	Backbone Length (GPC)	GPC-light M_w (kda.)	Backbone Length (GPC-light)
C_{10}	140	510	7286 3642	985	7036
C_{12}^1	168	155	922	390	2321
C_{12}^2	168	298	1773	545	3244
C_{18}	252	1000	7937 3968	1550	6150

Table 7.1: Molecular weights measured by GPC-light scattering show higher values than GPC measurements alone. This can be attributed to branched polymers passing through GPC columns slower than linear polymers.

for other polyolefins (C_{18} and two different backbone length C_{12}) produced in an

industrial extruder from the PX/1 dept. Typical values of dispersity range from 4.9 to 6.5.

The polymers can be characterised as semi-crystalline rubbers with melting points ranging from -10°C to +65°C. An increase in the side branch length increases the melting point of the polymer but is a secondary effect to backbone length. All Carishop polymers have shown a 60% isotactic formation with previous chemical shift investigations completed by the AG/32 department at K.S.L.A..

7.2.1.2 Viscosity Anomaly

Rheometric measurements by the PRP/431 department at K.S.L.A. were completed on the C_{10}, C_{12} and C_{18} industrial extruded Carishop polymers with respective molecular weights mentioned in the previous section. Specifically, viscosity measurements were obtained for shear rates between 10^{-3} s^{-1} to 5000 s^{-1}. To cover such a large shear rate range and to minimise errors at small shear rates, two instruments were used. Firstly, for the lower shear rates (10^{-3} s^{-1} to 1 s^{-1}), a *Rheometrics System IV* cone and plate rheometer, with a 50 mm cone, was used. For higher shear rates (0.5 s^{-1} to 5000 s^{-1}) an *Instron-Instrumat* capillary rheometer was used, with measurements taken for two different length to diameter ($\frac{L}{D}$) ratios of 20 and 81, to correct for capillary entrance and exit effects (Bagley correction). Capillary diameters were approximately 1.3 mm, with all measurements obtained at 80°C. In figure 7.3 the decrease in apparent viscosity as a function of applied shear stress can be seen for the various Carishop polymers. All measurements have been Bagley corrected from C_{12} capillary flows. The noteworthy features of these samples are three fold: firstly, relatively large zero shear viscosities ranging from 1 000 Pa s to 50 000 Pa s, secondly the different viscosity scaling dependence with shear rate of each different branched polymer and finally and most importantly, the order of the zero shear viscosity (η_o) for each curve.

It is thought the dominant feature of zero shear viscosity scaling for linear polymers is the proportionality: $\eta_o \sim {L_o}^3$ where L_o is the backbone length [75]. One would expect, for branched polymers, at least an increase in viscosity with backbone length, if not a similar scaling dependence, since the backbone length is greater than the branch length by two orders of magnitude. However an unclear trend is observed for zero shear viscosity scaling with backbone lengths, calculated by GPC alone (see table 7.2). In contrast a comparison of selected viscosities (C_{10} and C_{18}) with backbone lengths calculated from GPC-light scattering, show the predicted increase in viscosity as L_o increases, but this increase does not obey the ${L_o}^3$ scaling. A larger decrease in viscosity with shear rate for C_{10}, C_{12} and C_{14} by comparison with that observed for C_{18} is noted in Fig. 7.3. This suggests that

Carishop Polymer	Backbone Length (GPC)	Backbone Length (GPC-light scatt.)	η_o (kPa s)
C_{10}	7286 3642	7036	40.1
C_{12}	7976	-	14.2
C_{14}	8776	-	12.6
C_{18}	7937 3968	6150	2.0

Table 7.2: The zero-shear viscosity scaling dependence with backbone length is unclear if calculated from GPC data. In contrast selected GPC-light scattering measurements show an increase of zero-shear viscosity with backbone length but is far from conclusive.

the shorter branched polymers experience a stronger shear thinning dependence.

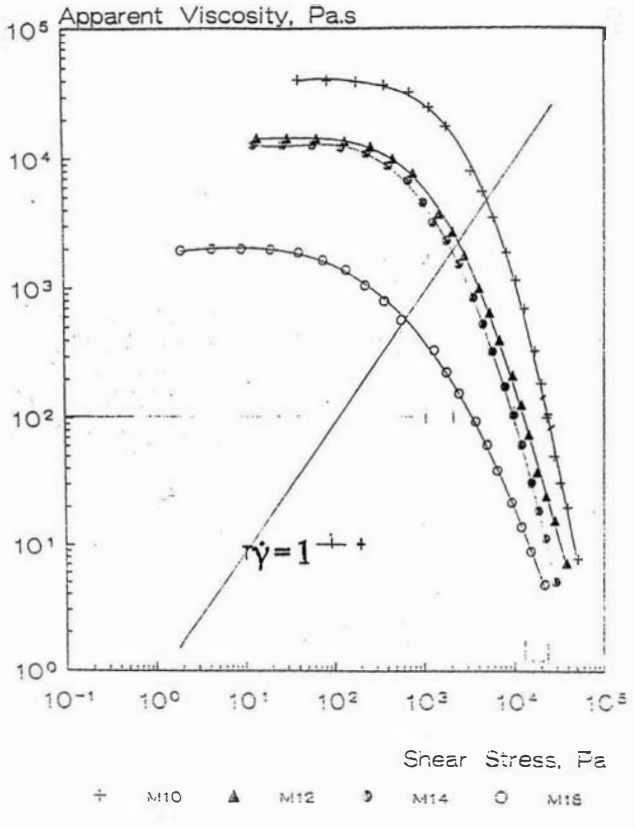

Figure 7.3: Previous viscosity measurements obtained by PRP/431 using cone-and-plate and capillary rheometers show a decrease in zero shear viscosity with increasing backbone length.

7.3 Results

7.3.1 Viscosity Measurements

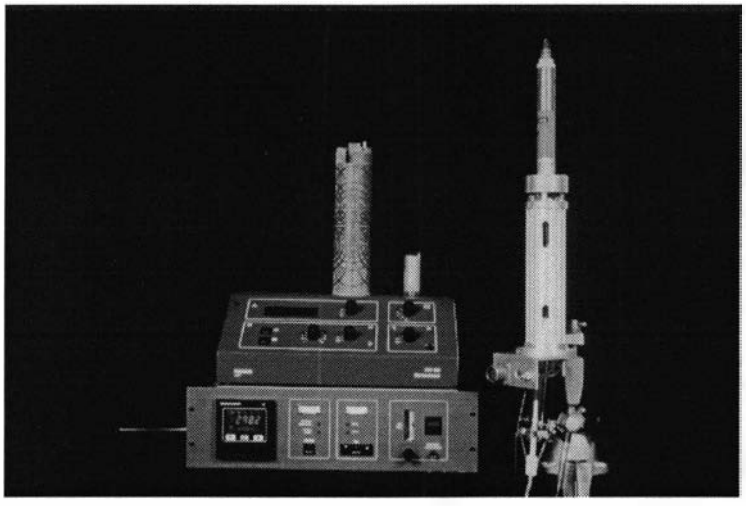

Figure 7.4: The heating of the Carishop polymers was completed outside the magnet to ensure no air bubbles were present in the melt. The heating was performed with the rheometer cell positioned inside the *Massey PGSE* probe.

The details of the combined cylindrical-Couette-cone-and-plate rheometer cell that was used for Carishop viscosity measurements are given in section 3.4.3. The C_{10} to C_{18} Carishop polymers previously used in rheometric studies had viscosities on the order of 1 000 to 40 000 Pa s. Thus use of the shear rates mentioned in the previous section, led to shear stresses of up to 50 000 Pa.

Approximately 800 mg of the elastic solids: C_{10}, C_{12} and C_{18}, in turn, were added to the rheometer cell and heated to 80°C, well above each of the polymer's melting point (~50°C). This preliminary heating was completed outside the magnet to ensure air bubbles were absent in the melt and to check the inner cylinder was in its correct position after being inserted. The rheometer cell was then attached inside a *Massey*[3] *PGSE*[4] gradient coil which in turn was placed inside the Bruker 200 MHz magnet (see Fig. 7.4). Fig. 7.5 shows a plot of the log of the apparent viscosity versus the log of the shear rate for the three Carishop materials. Immediately one can see that all the polymers measured have a different viscosity dependence on shear rate. This difference is quantified in the relative power law slope fittings, with C_{10}, C_{12} having $n \sim 0.5$ and C_{18}, $n \sim 0.1$ (refer Eqn. (2.19)).

With the shear rates covered, a Newtonian plateau, usually seen at low shear

[3] Massey University, Palmerston North, New Zealand.

[4] Pulsed Gradient Spin Echo

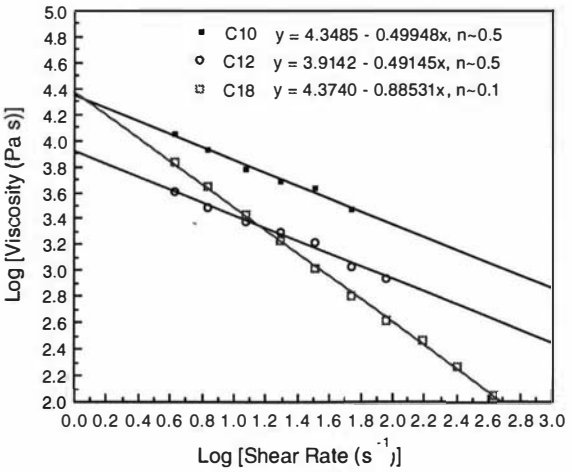

Figure 7.5: Viscosity measurements obtained from combined rheometer system for C_{10}, C_{12} and C_{18} polyolefins show a larger shear thinning dependence on shear rate for the C_{18} Carishop polymer.

rates, is absent. Because of this absence, an extrapolation to obtain the zero shear viscosity would not be correct. A more important emphasis here is placed on the relative scaling of viscosity with shear rate and the trend this scaling has with previous viscosity measurements (Fig. 7.3). To illustrate Carishop apparent viscosity scaling with different backbone lengths, viscosity results for two different C_{12} polymers are shown in Fig. 7.6. The obvious increase in viscosity with increasing backbone length supports the idea of viscosity scaling being a backbone length dominated effect, rather than a side branch length effect. Again power law values around 0.5 were obtained. It is noted that repeated measurements did not yield the same torque values, for apparently identical experimental conditions. This can be attributed to a bearing friction coefficient which is varying as each sample is loaded into the rheometer cell. A possible reason for the change could be unwanted material on the bearing itself. This change in friction should result in a simple displacement of shear stress, thus a displacement in apparent viscosity. As the friction coefficient should not change as a function of shear rate, the scaling of apparent viscosity should be correct.

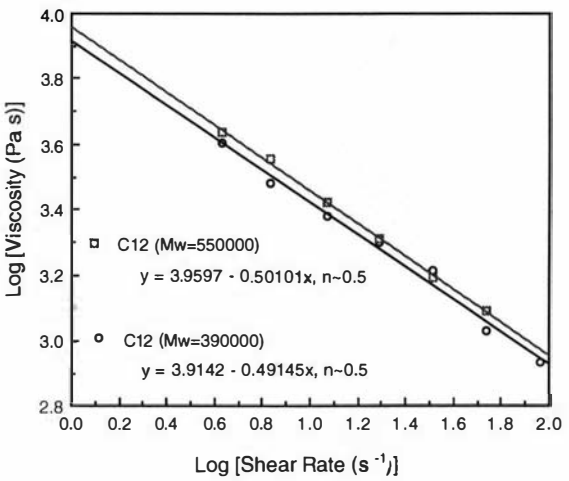

Figure 7.6: C_{12} viscosity measurements for different backbone lengths reveal similar shear thinning characteristics and, as predicted, an increase in viscosity for the larger backbone length.

7.3.2 Relaxation Measurements

7.3.2.1 T_2 Zero Shear

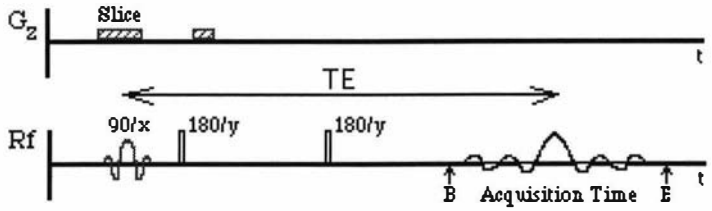

Figure 7.7: The spin echo pulse sequence enabled a measurement of the echo height (or alternatively spectrum area) as a function of TE.

As rheometric data was collected for the Carishop melts, T_2 measurements were also studied using the *spin echo* pulse sequence shown in Fig. 7.7. To achieve this a broadband, high power decoupled, Bruker MSL spectrometer was used. This spectrometer along with a *Techron* 270 amplifier, providing current to the z gradient coil, enabled a slice selection of 1 mm to be chosen in the cylindrical Couette region. To ensure all relaxation measurements could be regarded as applying to

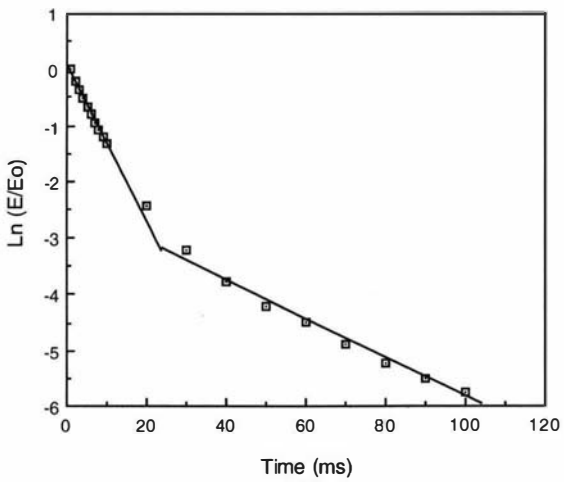

Figure 7.8: T_2 measurements at zero shear rate for the C_{12} Carishop shows bi- exponential relaxation behavior. This relaxation behavior could be attributed to larger mobility of the ends of the side branches of the polymer.

motionally-narrowed spins (see Fig. 3.4), T_1 values for all Carishop samples were taken at 80 and 100°C. All samples showed an increase in T_1 times with an increase in temperature.

Plotted in Fig. 7.8, at zero shear rate, is the natural logarithm of the echo height, expressed as a ratio of the initial echo height, versus half of the echo time (TE). Clearly two relaxation regimes are evident with a fast relaxing component having a time constant on the order of 19 ms and a slow relaxing component having a time constant of around 89 ms. Such bi-exponential plots measured in the melt for linear polymers [100], also using T_2, suggest that such regimes can be attributed to either polydispersity within a sample or detection of differences of mobility at different locations along the polymer chain.

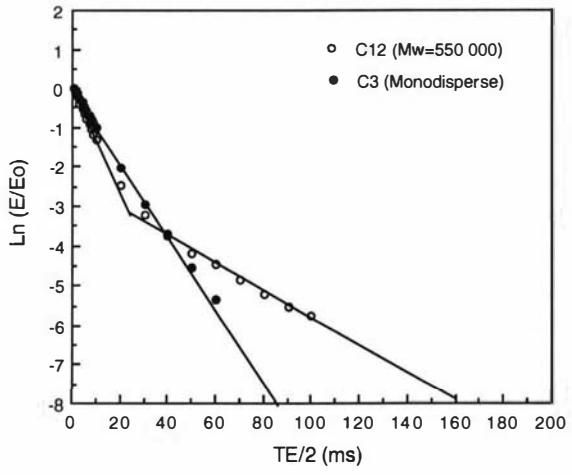

Figure 7.9: Comparison of T_2 measurements for poly and mono-disperse polyolefins show an absence of a slow relaxation component. This absence may be due to either mono dispersity or less mobile branches in the polypropylene.

To investigate whether dispersity has a strong effect on bi-exponential behavior, relaxation measurements were also performed on monodisperse ($\frac{M_w}{M_n} = 1.1$) polypropylene C_3 (Fig. 7.9). Although the resulting curve is not single exponential, a clear slow component cannot be determined. This slow component's absence suggests that the previous slow component for the C_{12} may well indeed be a result of dispersity. Alternatively the slow component (large mobility) may be absent because of the smaller side branching of C_3. Strong evidence that T_2 variation arises from mobility within the chain rather than polydispersity is apparent in Fig. 7.10, where a typical data set for the echo decay as a function of the increase

in echo time for C_{12}, is shown. Close inspection of this relaxation figure shows poorly resolved spectra, in which at least two chemical shifted species can be seen. One can clearly identify the left and right components of these spectra in Fig. 7.8 as being the fast and slow relaxation components respectively. Interestingly these two components, again in the same order, are centred at 1.2 and 0.9 ppm respectively. These chemical shift reference points coincide with chemical shift points for methylene and methyl moieties respectively as indicated by previous chemical shift analysis on Carishop polymers [101]. Thus the two relaxation components have been identified as the methylene and methyl groups found in the Carishop polymer's side branches. Ambiguity may rise over the placement within the chain of the methylene relaxation measurement, but this can be quickly dispelled if one compares relative magnitudes, or areas of the spectra, of the methylene group in the side branches and the methylene groups in the backbone, compared to the methyl group.

To obtain a comparison of the magnitude of the two components within the spectrum, a four component deconvolution algorithm was applied (Fig. 7.11) to the C_{12} spectrum, collected at an echo time of 2 ms. The broad spectrum shown in this figure can be attributed to background broadening thus leaving two peaks centred around the previously predicted ppm values. The data in table 7.3 reveals

Peak N°	Associated Group	Predicted Freq.(ppm)	Predicted Mag. (%)	Deconvol. Freq.(ppm)	Deconvol. Mag. (%)
1.	CH	1.5	4.2	-	-
2.	$CH_2^{backbone}$	1.4	8.3	-	-
3.	CH_2^{branch}	1.2	75.0	1.2	69.2
4.	CH_3	0.9	12.5	0.9	17.8

Table 7.3: Comparisons of C_{12} protons, localised at the ends and within the branches of the polymer, show predicted and experimental magnitudes, calculated from deconvolution of the spectra, are similar.

a larger signal magnitude in the methylene group, centred around 1.2 ppm, compared to the methyl group, but, overall, show a disagreement with the predicted magnitudes. This disagreement has been attributed to the different relaxation mechanisms of each component and the overall poor resolution of original spectrum. Nevertheless the methylene magnitude, being a lot larger than the methyl magnitude, provides considerable support that this species is located in the side branches of the polymer.

When relaxation behavior is compared between different types of Carishop polymers as in figure 7.12, an illustration of different mobility according to polymer section length can be seen. The backbone length of the polymers increases in the order of C_{18}, C_{12} followed by C_{10}. The methylene relaxation times, as expected, decreases in this order. Similar relaxation times for the methyl groups for C_{10} and C_{12} could be expected, because of the similar side branch length, but an increase in mobility of a larger side branch length for C_{18} is not expected. Alternatively an increase in length of the side branch for C_{18} could inhibit entanglements of the main backbone within the melt, causing an increase in mobility to be seen not only in the ends of the branch chain but in the branch overall, ie. methylene *and* methyl groups. This process of increase in mobility could be the effect causing a longer relaxation component than expected for the methylene group in C_{18}, which has a backbone length (table 7.1) similar to that of C_{10}.

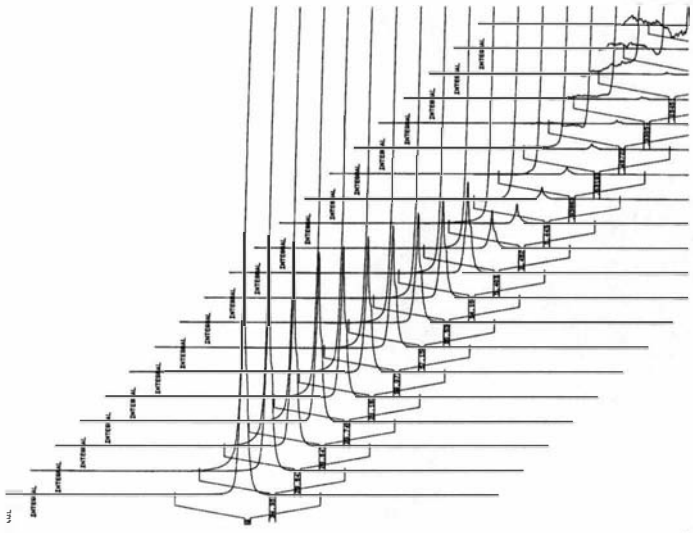

Figure 7.10: In a typical echo decay data set, two T_2 components can be seen in the poorly resolved proton spectra. Note the poorly resolved, slow relaxing, second peak.

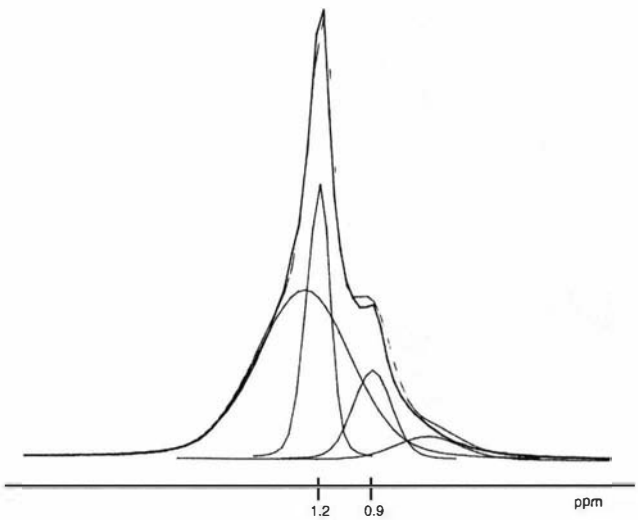

Figure 7.11: A four component deconvolution of the spectrum reveals slow and fast T_2 components are centred around 0.9 and 1.2 ppm respectively. The broad background spectrum can be ignored as inhomogeneous broadening.

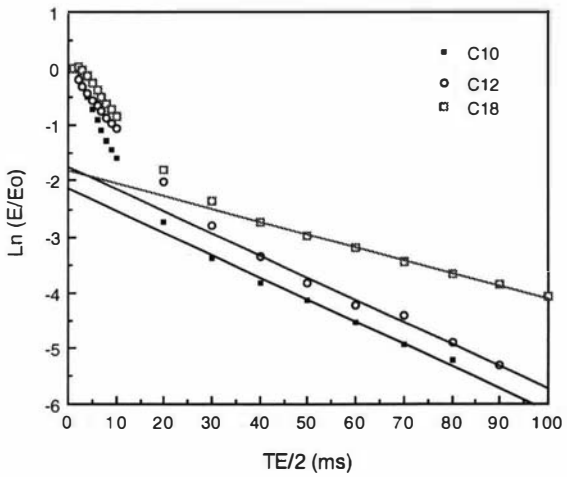

Figure 7.12: Relaxation data for various Carishop polymers show more mobile side branch ends for C_{18} as the polymers slow relaxation component is slower than the other Carishop polymers.

7.3.2.2 T_2^* Influence of Shear

Relaxation measurements were carried out on Carishop polymers undergoing shear rates between 0 and ~91 s^{-1}. The relaxation data for C_{12} is seen in figure 7.13 (a). Similar bi-exponential decays are observed for zero shear rate but as the shear rate is increased the longer relaxation time component is more attenuated. This reduction has been attributed to a decrease in mobility or alignment of the ends of the side branches as the shear rate is increased. A comparison of loss of mobility between C_{12} and C_{18}, under shear (Fig. 7.13 (b)), suggests the C_{18} polymer aligns and disentangles more easily than that of the C_{12} polymer.

Because of sample rotation the refocussing of the spins occurs in a different position within the magnet to that at which dephasing takes place. Consequently the signal is further attenuated due to inhomogeneous broadening. This inhomogeneous refocussing means that the relaxation time being measured is partly T_2 and partly T_2^*. To ensure that the more attenuated signal was not a result of inhomogeneous broadening alone, a 95% ethanol sample was used under the same shear conditions. Relaxation measurements revealed an absence of extra attenuation.

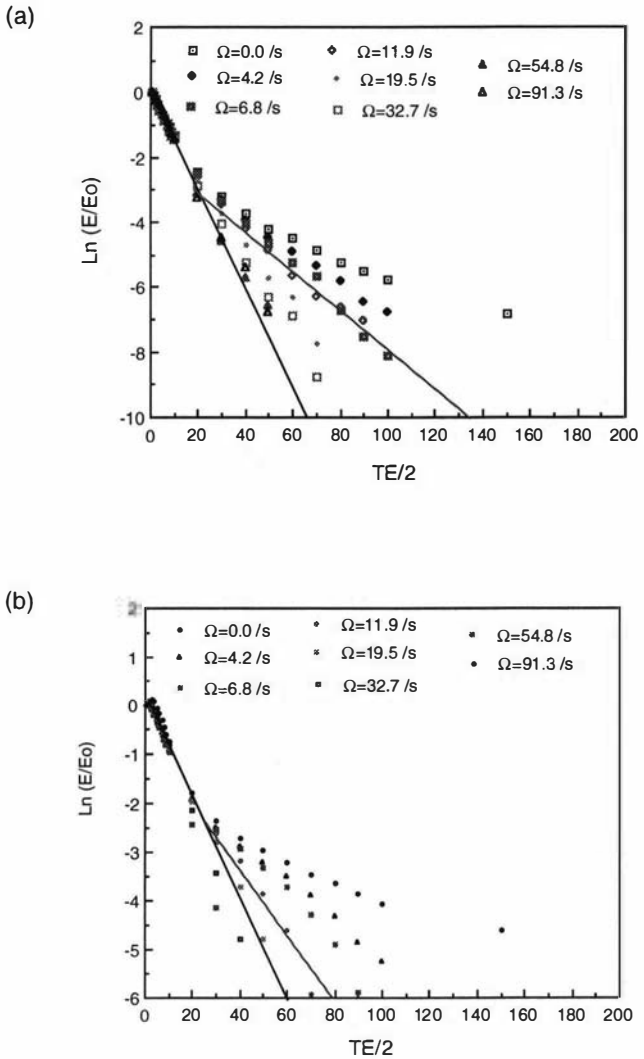

Figure 7.13: (a) A decrease in mobility is noted, via T_2^* scaling, for C_{12} polyolefins as the shear rate is increased. (b) Comparison of the rate of decrease in mobility between C_{12} and C_{18} reveals that C_{18} is more easily aligned.

7.4 Conclusions

Previous results measuring the zero shear viscosity of varying branched Carishop polymers, in which the zero shear viscosity increased as side branch length decreased, can be explained in terms of erroneously determined molecular weight using GPC. A more accurate molecular weight measurement of the Carishop polymers using GPC-light scattering, shows that the ordering of zero shear viscosity follows the ordering of the backbone lengths, but not as $\eta_o \sim {L_o}^3$.

Viscosity measurements obtained from the combined cylindrical Couette-cone -and-plate rheometer show a higher degree of shear thinning behavior for the higher branched Carishop polymers. This apparent contradiction with previous rheometric data can be explained as the shear rates were measured in capillary rheometers for short $\frac{L}{D}$ ratios. Although Bagley corrections were obtained for C_{12} this should have been done for all different branched Carishop polymers.

Proton T_2 relaxation experiments on the Carishop polymers reveal two main components identified respectively as signals arising from protons at the ends of the side branch chain and in the side branch itself. Relative scaling of relaxation times between different branched Carishop polymers suggest a higher mobility at the ends of the branches for higher order polyolefins.

$T_2{}^*$ measurements carried out under shear suggest a loss of mobility at the ends of the chains as the shear rate is increased. The rate of this loss of mobility for different branched Carishop polymers suggest C_{18} is easier to align and disentangle.

The low power law behavior of C_{18} could be explained by the polymer's easier alignment under shear as shown by $T_2{}^*$ measurements.

Chapter 8

Large Magnetic Field Gradients

8.1 The Need for Large Magnetic Field Gradients

Throughout this thesis the predominant NMR measurement has been of proton translational velocities, achieved in a variety of different geometries. Also, previous work (Ch. 4) has utilised the measurement of slow polymer self diffusion, again detecting the proton signal. Both of the above methods of measurement rely on the PGSE pulse sequence. A unifying requirement for both methods is the need for use of homogeneous applied gradients that will produce a minimum amount of eddy currents. These currents, if produced, will create a magnetic field that may perturb the original gradient, an effect which is undesirable, but avoidable as explored later in this chapter.

With the previous studies in this thesis the value of higher available gradient strength has become apparent. For example in chapter 4, to obtain a measurement of a slower self diffusion coefficient or investigate the internal reptating dynamics (see Sec. 2.4.3) of the PEO polymer, a larger gradient is necessary. Likewise to clarify the slip phenomena behavior of Xanthan gum, a higher resolution image of the wall boundary is required (see Ch. 5). This change in the 'field of view' also requires the application of larger gradients. A similar resolution change is essential if larger shear rates are sought after with smaller rheometer cells, again demanding larger gradients.

If Rheo-NMR is to be extended to order parameter measurement, using for example the 'quadrupole line splitting'[54], deuterium-NMR studies would have to be implemented. Such a nucleus change would have dramatic effects on the required gradient magnitude if the study included spatial localisation. The gyromagnetic ratio for deuterium is seven times smaller than that of protons, thus the magnitude of the gradients would scale accordingly.

It must be noted that the resolution in NMR microscopy is limited both by susceptibility artifacts and by molecular diffusion itself. These limitations, as discussed later in this chapter (see Sec. 8.3), can be extended if certain pulse sequences, utilising large gradients, are adopted.

As part of this thesis a large-gradient coil set was developed, tested and used for high spatial resolution experiments.

8.2 Probe Development

8.2.1 The Quadrupole Gradient Coil

When pulsed gradient dependent measurements are made in nuclear magnetic resonance, care must be taken to avoid perturbation of the signal by transient fields due to eddy currents induced in the surrounding metal of the superconducting magnet cryostat. It will be shown that quadrupole coils have some advantages in this respect when used in conjunction with superconducting polarizing magnets. Measurement of slow diffusion, where large gradients are required, is also an experimental area for which the use of quadrupole coils can be advantageous. Another advantage is the quadrupole coil's high ratio of gradient strength to driving current and coil inductance.

The orientation of the quadrupole coil (Fig. 8.1), axis transverse to the direction of the main field B_o, has the advantage of minimising eddy currents produced by pulsation of the gradients. This minimisation is achieved by the absence of conductive material above and below the gradient coil. Modern NMR magnets are either vertical or horizontal superconducting solenoids. In each case the polarizing field is parallel to the bore axis. Because the axis of a quadrupole gradient coil is required to be normal to the polarizing field, this results in the need for horizontal loading. This disadvantage is small compared to the advantages mentioned above.

The exact current configuration of the quadrupole coil is shown in figure 8.2, where four main current paths[1] can be seen moving into and out of the page. This configuration results in linear magnetic field gradients $\frac{\partial B_z}{\partial x}$ and $\frac{\partial B_x}{\partial z}$. Because the polarizing field, B_o, is much larger than the local fields produced by the gradient coil, all orthogonal fields produce only second order effects and can therefore be neglected. Hence only $\frac{\partial B_z}{\partial x}$ is important. In particular, as shown in Fig. 8.2, there is a diagonal (45°) field variation, which can be used to create a $\frac{\partial B_z}{\partial z}$ gradient by rotating the current configuration by 45°. Thus a dual current distribution is obtained, creating field gradients in the x and z directions (G_x and G_z). These

[1] Hence the name 'quadrupole'.

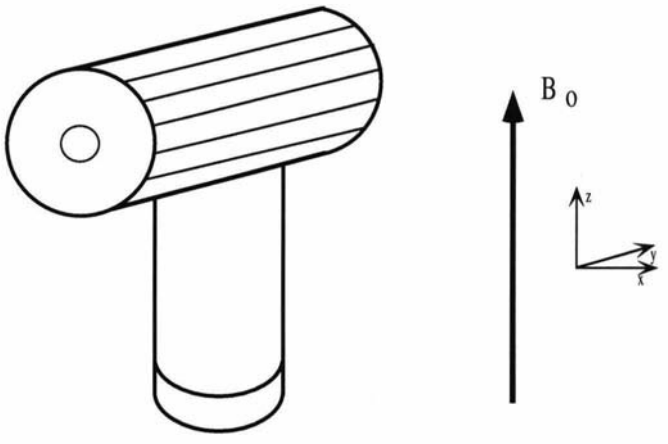

Figure 8.1: The transverse orientation of the quadrupole coil, to the main polarising field B_o, provides minimal eddy currents because of the absence of conductive material above and below the gradient coil.

gradients have an improved homogeneity if the currents approximate the distribution $I = I_o \cos 2\phi$. I_o is the current located at the main current path and I the current at angle ϕ, from that path. This $\cos 2\phi$ variation can be achieved by having a discrete wire distribution of 10.14.10 or 7.10.7, at 45° separation. In a practical situation as shown, the G_x and G_z coils are wound at different depths. The smaller number of wires required for the gradient G_y is due to the currents being located at a smaller radius (closer to the axis of the system). The dual gradient system is seen in Fig. 8.3.

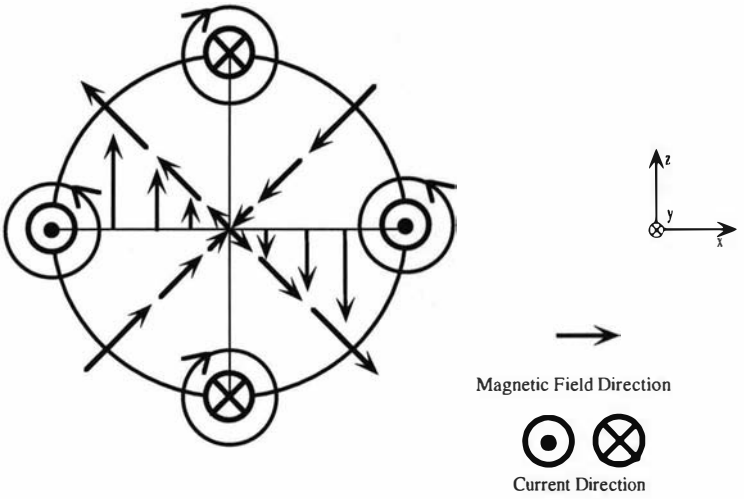

Figure 8.2: The magnitude of the diagonal magnetic fields produced by the quadrupole coil are second order compared to the main field B_o (collinear to the z direction). The four main current 'poles' give rise to the quadrupole coil's name.

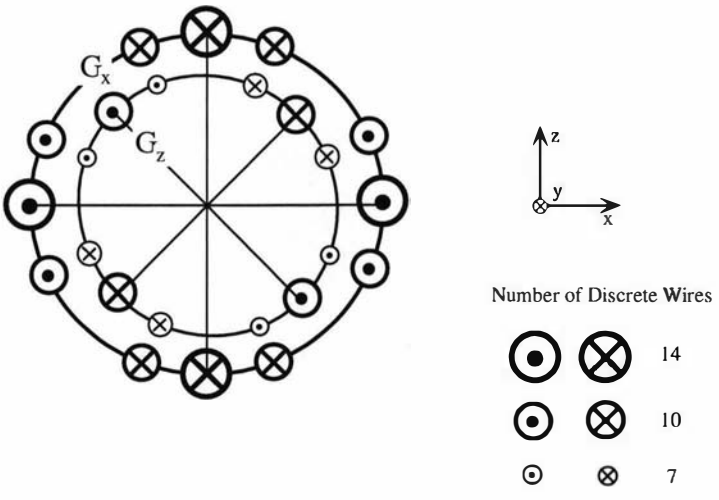

Figure 8.3: An improved gradient homogeneity is achieved for the quadrupole coil if a $\cos\phi$ current distribution is used. This is achieved with a 10.14.10 and 7.10.7 discrete wire distribution for the G_x and G_y gradients respectively.

8.2.1.1 Homogeneity and Gradient Calculations

The resolution of an image in NMR is limited by various parameters such as the diffusion of the molecules containing the nuclei, available bandwidth and gradient strength. The linearity or homogeneity of the gradient is important to avoid distortion of an image. A gradient strength of at least 0.20 T m^{-1} A^{-1} was sought for the quadrupole coil, with a 0.50 % field variation over a volume of 50.0 mm^3 (3.0 mm radius). The desired gradient strength allowed for the possibility of slow diffusion being measured, ($\leq 10^{-13}$ m^2 s^{-1}). The gradient amplifier to be used with the quadrupole coil is the Bruker B-AFPA 30. This amplifier provides a maximum of 1.80 kW of pulsed power with a rail voltage of approximately 60.0 V. Both constant current and constant voltage modes are available, with a selection of rise and fall times for different load impedances. Because of the power dissipation in the gradient coil, a limit of $\leq 2.0\ \Omega$ is required for the resistance for each gradient set (G_x and G_z).

For the above conditions, diameters for the current distributions of 16.0 mm and 20.0 mm were chosen for G_x and G_z respectively. A length of 50.0 mm was also chosen to optimise the homogeneity while maintaining the required gradient strength. The geometry and current were optimised using a integrative method, calculating both gradient strength and homogeneity. The Biot-Savart law was used to do this calculation. This law states that the magnetic field, **B**, is calculated at a point, **r**, as a contribution of current elements, $d\mathbf{l}$, along a discrete wire from L_o to L_{max}:

$$\mathbf{B}(\mathbf{r}) = \frac{\mu_o}{4\pi} \int_{L_o}^{L_{max}} \frac{d\mathbf{l} \times \mathbf{r}}{|\mathbf{r}|^3} \tag{8.1}$$

A plot of the calculated B_z field component as a function of x (Fig. 8.4), shows the required linear field variation, G_x. Linear regression reveals a gradient of approximately 0.20 T m^{-1} A^{-1}. The variation of this gradient in the y direction is 0.34 % for $\pm$ 5.0 mm. Similar results were obtained over lesser distances of $\pm$ 3.0 mm in the x and z directions. The G_z gradient is also calculated as approximately 0.20 T m^{-1} A^{-1}, but in this case a larger variation of 0.50 % is predicted along the y direction for $\pm$ 5.0 mm (Fig. 8.5). The variation in the x and z directions were similar to that of the G_x calculations with all results still lying within the homogeneity criteria mentioned earlier.

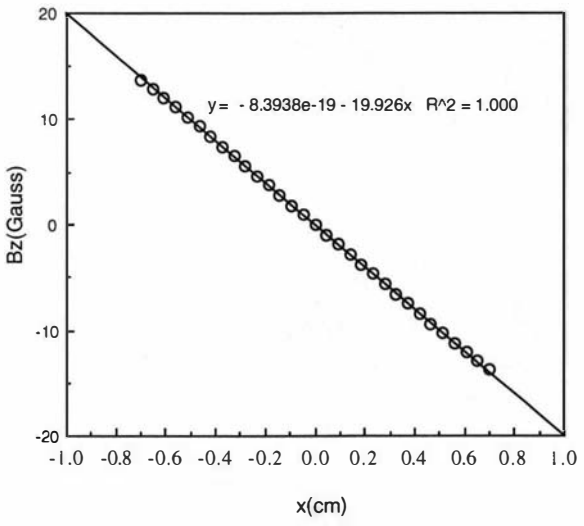

Figure 8.4: The linear variation of the G_x gradient shows a magnitude of 0.20 T m^{-1} A^{-1} is expected.

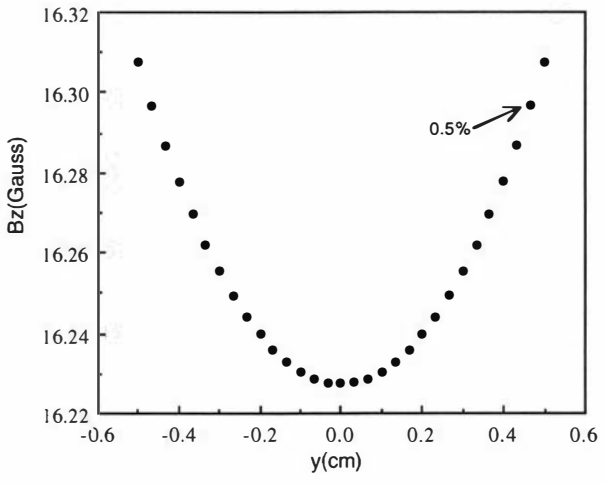

Figure 8.5: A 0.5% field variation is calculated for the G_z gradient for a $\pm$ 5.0 mm positional variation along the y direction.

8.2.1.2 Active Screening of the Quadrupole Coil's 'End Fields'

Active screening for coils wound on cylindrical formers involves a cancellation of all fields beyond a certain radius from the cylinder axis. Because the quadrupole axis is normal to the polarizing field in a superconducting magnet application, the normal screening consideration must be re-examined. Suppose we label the gradient coil axis z and the direction of the polarizing field y, then we need not concern ourselves with fields extending along the y direction beyond the radius mentioned above. Within this radius, fields may interact with the bore wall producing eddy currents. The distance from the gradient coil to the bore wall may be only a few centimeters, so stray field effects have to be considered. Active screening involves a superposition of two fields which will produce a linear magnetic field variation inside the coil and zero field outside. Adopting a cylindrical coordinate system, the screening conditions are found by first considering the relative current distributions ($J_\phi(\mathbf{r})$, $J_z(\mathbf{r})$) that will produce the desired magnetic field gradient inside the coil. In the case of the quadrupole coil, the current distributions are distributed on a cylindrical surface of radius, a (see Fig. 8.6). The theory of active screening has been developed by Turner and Bowley[102], the main points are summarized here. The vector potential ($\mathbf{A}$) of the current distribution is defined as:

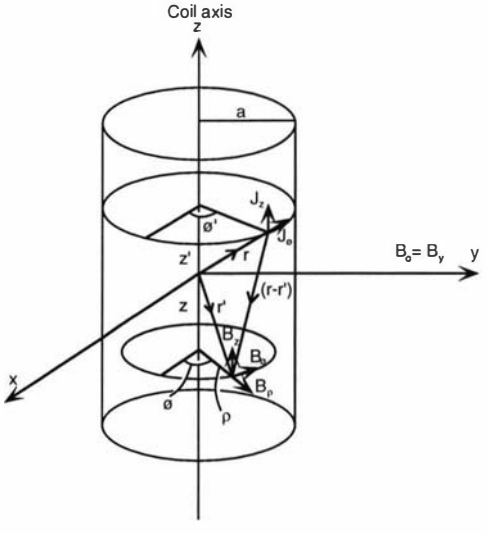

Figure 8.6: Current distributions $J_\phi(\mathbf{r})$ and $J_z(\mathbf{r})$ located on a cylinder of radius a, produce field components B_ρ, B_ϕ and B_z at radius ρ. Using an inverse space formalism, current distributions can be calculated for a desired magnetic field.

$$\mathbf{A} = \frac{\mu_o}{4\pi} \int \frac{\mathbf{J}(\mathbf{r}')dv'}{|\mathbf{r} - \mathbf{r}'|} \tag{8.2}$$

Each component of **A** can can be expressed in cylindrical coordinates as the following:

$$A_\rho = \frac{\mu_o}{4\pi} \int \frac{J_\phi(\mathbf{r}') \sin(\phi - \phi')dv'}{|\mathbf{r} - \mathbf{r}'|} \tag{8.3}$$

$$A_\phi = \frac{\mu_o}{4\pi} \int \frac{J_\phi(\mathbf{r}') \cos(\phi - \phi')dv'}{|\mathbf{r} - \mathbf{r}'|} \tag{8.4}$$

$$A_z = \frac{\mu_o}{4\pi} \int \frac{J_z(\mathbf{r}')dv'}{|\mathbf{r} - \mathbf{r}'|} \tag{8.5}$$

$$\tag{8.6}$$

The convolution of terms which defines the vector potential in real space, becomes a simpler product of terms in a reciprocal space. Using a Green's function[103] expression in reciprocal space (k), we transform the vector potential components into a cylindrical coordinate form:

$$\frac{1}{|\mathbf{r} - \mathbf{r}'|} = \frac{1}{\pi} \sum_{m=-\infty}^{\infty} \int_{-\infty}^{\infty} dk e^{im(\phi-\phi')} e^{ik(z-z')} I_m(k\rho^<) K_m(k\rho^>) \tag{8.7}$$

I_m and K_m are modified Bessel functions, with $\rho^>$ the greater of the pair ρ and a and $\rho^<$, the lesser. Fourier relationships for the current distributions are defined as:

$$J_z^m(k) = \frac{1}{2\pi} \int_{-\pi}^{\pi} \int_{-\infty}^{\infty} dz d\phi e^{-im\phi} e^{-ikz} J_z(\phi, z) \tag{8.8}$$

$$J_\phi^m(k) = \frac{1}{2\pi} \int_{-\pi}^{\pi} \int_{-\infty}^{\infty} dz d\phi e^{-im\phi} e^{-ikz} J_\phi(\phi, z) \tag{8.9}$$

$$\tag{8.10}$$

The vector potential components can now be expressed in a reciprocal space form:

$$A_\rho = -\frac{i}{2} \Gamma J_\phi^m(k) a [I_{m-1}(k\rho^<) K_{m-1}(k\rho^>) - I_{m+1}(k\rho^<) K_{m+1}(k\rho^>)] \tag{8.11}$$

$$A_\phi = \frac{1}{2} \Gamma J_\phi^m(k) a [I_{m-1}(k\rho^<) K_{m-1}(k\rho^>) + I_{m+1}(k\rho^<) K_{m+1}(k\rho^>)] \tag{8.12}$$

$$A_z = \Gamma J_\phi^m(k) a I_m(k\rho^<) K_m(k\rho^>) \tag{8.13}$$

$$\text{where} \quad \Gamma = \frac{\mu_o}{2\pi} \sum_{m=-\infty}^{\infty} \int_{-\infty}^{\infty} dk e^{im\phi} e^{ikz} \tag{8.14}$$

The magnetic field (**B**) is the curl of the vector potential. It is a trivial matter to rewrite each magnetic field component in terms of its inverse space, current

distribution:

$$\mathbf{B} = \nabla \times \mathbf{A} = \frac{1}{\rho}\begin{vmatrix} \rho_\rho & \rho_\phi & \mathbf{k} \\ \frac{\partial}{\partial\rho} & \frac{\partial}{\partial\phi} & \frac{\partial}{\partial z} \\ A_\rho & \rho A_\phi & A_z \end{vmatrix} \tag{8.15}$$

$$\Rightarrow B_\rho = \frac{1}{\rho}\left[\frac{\partial A_z}{\partial\phi} - \rho\frac{\partial A_\phi}{\partial z}\right] \tag{8.16}$$

$$= i\Gamma k a J_\phi^m(k) I'_m(k\rho^<) K'_m(k\rho^>) \tag{8.17}$$

$$\Rightarrow B_\phi = \left[\frac{\partial A_\phi}{\partial z} - \frac{\partial A_z}{\partial\rho}\right] \tag{8.18}$$

$$= -\Gamma\frac{ma}{\rho} J_\phi^m(k) I'_m(k\rho^<) K'_m(k\rho^>) \tag{8.19}$$

$$\Rightarrow B_z = \frac{1}{\rho}\left[A_\phi + \frac{\partial A_\phi}{\partial\rho} - \frac{\partial A_\rho}{\partial\rho}\right] \tag{8.20}$$

$$= \Gamma k a J_\phi^m(k) I'_m(k\rho^<) K'_m(k\rho^>) \tag{8.21}$$

The B_y field component is calculated from the vector addition of its coplanar components, namely B_ρ and B_ϕ:

$$B_y = B_\rho \sin\phi + B_\phi \cos\phi \tag{8.22}$$

$$= \frac{1}{2}\Gamma k a I_m(k\rho^<)\left[J_\phi^{m-1}(k) K'_{m-1}(k\rho^>) - J_\phi^{m+1}(k) K'_{m+1}(k\rho^>)\right] \tag{8.23}$$

The problem of screening the fields outside a quadrupole coil has been considered by Turner[104]. The most important pulsed field component to be screened, is that produced in the direction of the main field $\mathbf{B_o}$. In the calculations above this is the B_y field component. Other directed field perturbations will be second order to this, since B_o has a large magnitude compared to other directed field components.

New current distributions ($j_\phi(\mathbf{r})$, $j_z(\mathbf{r})$) are defined at a radius b which is greater than a. A convolution of two magnetic fields is now produced canceling the fields outside the coil while still maintaining the linear field inside. A similar expression for B_ρ without screening (Eqn. (8.17)) is obtained with each of the current distributions now defined at their relative radii of a and b as follows:

$$B_\rho = \Gamma k I'_m(k\rho^<) K'_m(k\rho^>) \times\left[a J_\phi^m(k) + b j_\phi^m(k)\right] \tag{8.24}$$

To cancel the field component from Eqn. (8.24) outside the radius b, an expression for the inverse space current distribution $j_\phi^m(k)$ is calculated given $J_\phi^m(k)$ as follows:

$$B_\rho = 0 \qquad \text{for} \qquad \rho > b \tag{8.25}$$

$$\Rightarrow \quad aJ_\phi^m(k)I'_m(ka) + bj_\phi^m(k)I'_m(kb) = 0 \tag{8.26}$$

$$\Rightarrow \quad j_\phi^m(k) = -\frac{a}{b}\frac{I'_m(ka)}{I'_m(kb)}J_\phi^m(k) \tag{8.27}$$

The same expressions are obtained when screening for B_ϕ and B_z field components outside the screening current radius, b. A direct result of this, is that the field component B_y is automatically screened when screening B_ρ, since its components are superpositions of B_ρ and B_ϕ (Eqn. (8.23)). Thus by calculating the current distribution $j_\phi^m(k)$ from equation (8.27) one automatically screens the B_y field component. With the transverse orientation of the quadrupole coil mentioned

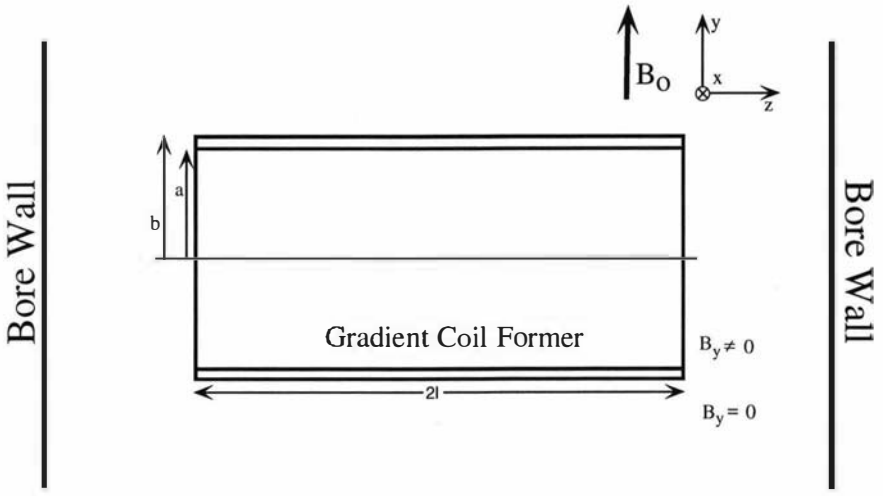

Figure 8.7: Active screening may propose a possible solution in screening magnetic fields in the volume defined outside of radius b. The 'end fields' produced inside radius b may not necessarily be screened when screening outside this radius.

earlier, a screening volume is now defined (Fig. 8.7) outside the radius b.

A major question not considered by Turner is how to screen any fields inside the coil radius, outside the length ($\pm l$). The question now arises as to whether the 'end fields' of the quadrupole coil can be actively screened in this second volume (inside the radius a and outside the length $\pm l$).

Re-calculation of the Bessel functions inside radius a for the B_ρ field component

reveals the following:

$$B_\rho = 0 \qquad \text{for} \qquad \rho < a \tag{8.28}$$

$$\Rightarrow \quad aJ_\phi^m(k)K_m'(ka) + bj_\phi^m(k)K_m'(kb) = 0 \tag{8.29}$$

$$\Rightarrow \quad j_\phi^m(k) = -\frac{a}{b}\frac{K_m'(ka)}{K_m'(kb)}J_\phi^m(k) \tag{8.30}$$

It is clear that simply using the condition for $B_\rho = 0$ for $\rho \leq a$ results in cancellation of the desired gradient at the coil centre. What is needed is the condition $B_\rho = 0$ for $z \geq l$ and $z \leq -l$. Such a condition requires either that the current distribution vary along the z axis or that some appropriate current distribution exists on disks normal to the coil axis and positioned at $z = \pm l$. The solution to this current distribution is a complex one and an alternative approach was taken to ask the question, do these fields need to be screened at all? In particular, is the magnitude of the end fields produced from the quadrupole coil sufficient to cause perturbing eddy currents?

8.2.1.3 Eddy Field Calculations

Field calculations of the quadrupole coil were completed to establish if eddy fields produced from the coil would perturb the produced gradient. As a guide to what magnitude of stray field would result in problems, pulsed gradient experiments were carried out at the Karlsruhe Laboratory of Bruker Analyitische Messtechnik. A 30.0 mm OD, unscreened saddle gradient coil was tested for eddy currents. Testing was performed in a vertical superwide bore (15.0 cm ID), super conducting magnet. A gradient ~~strength~~ pulse of 1.0 T m^{-1} was applied before a 90° rf excitation pulse and no perturbing ~~influenced~~ the collected FID was detected at the shortest delay time used (50 μs). This experiment gave a clear indication of what stray fields could be tolerated without suffering eddy current effects.

Using the integrative method described earlier (Eqn. (8.1)), parameters for a dummy saddle coil were chosen to produce the same gradient strength as the above reference experiment. These parameters included coil diameter, current supply and number of discrete wires. Figure 8.8 shows these parameters as well as the orientation within the magnet and the direction of each field component.

Figure 8.9 shows a plot of the B_z field component as a function of x for the saddle coil (note that by contrast with the quadrupole coil, the saddle coil's z-axis is collinear with the polarizing field). Hence it is the z-axis component which we must consider. The best fit line has a slope of 1.0 T m^{-1} within $\pm$ 1.0 cm of the coil's origin. To observe the nature of the B_z field outside the coil, a three

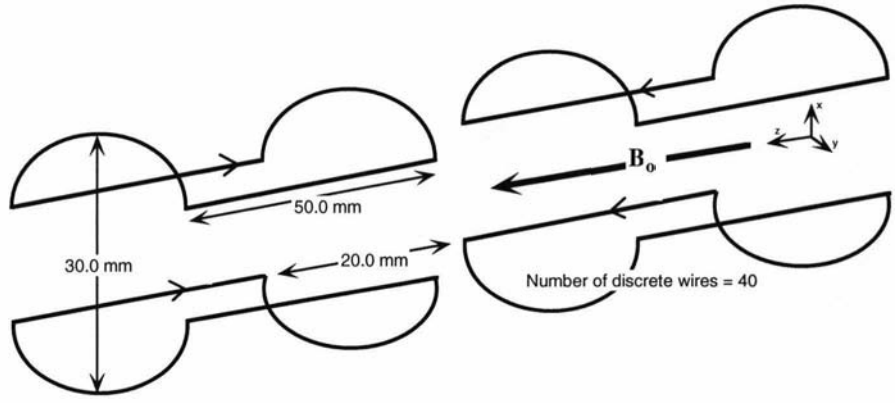

Figure 8.8: Field calculations for a dummy saddle coil were completed to estimate the criteria for whether eddy currents will be produced for a given pulsed gradient strength. The relevant parameters and orientation of the coil to the main field B_o are given.

dimensional plot (Fig. 8.10(a)) is shown. The B_z gradient can be seen at the origin of this plot, as well as four large 'field spikes' associated with the return current paths on the coil. Other return current paths can also be seen with smaller field spikes near the origin of the plot. The coil's diameter and length can be 'outlined' with the reversal of sign of the magnetic field. A similar three dimensional plot is also shown for the B_y field of a quadrupole coil operating at 1.0 T m^{-1} (Fig. 8.10(b)). Note again that the B_y field of the quadrupole coil is collinear with the polarizing field direction). Again the gradient and outline of the coil can clearly be seen. The relative magnitudes of each of the fields in the three dimensional plots (Fig. 8.11), show the fields decreasing rapidly as the distance from the coil is increased.

For superwide bore (7.50 cm) and wide bore (4.50 cm) distances from the coil respectively, the saddle coil's B_z field is ~~larger than~~ that of the quadrupole coil B_y field. Given our experience with the Karlsruhe' experiments this suggests that the quadrupole coil will not produce perturbing eddy currents when operating at 1.0 T m^{-1}. Indeed we might expect to be able to operate at much higher gradient strength without significant effects. It should be noted however that at standard bore diameters (2.50 cm), eddy current problems may arise and active screening for these fields may be needed.

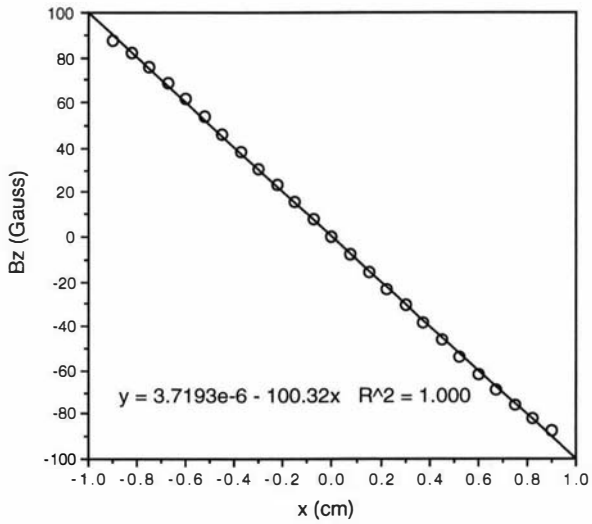

Figure 8.9: Regression calculations of the gradient strength of the dummy saddle coil reveal the required value of 1.0 T m^{-1} is achieved.

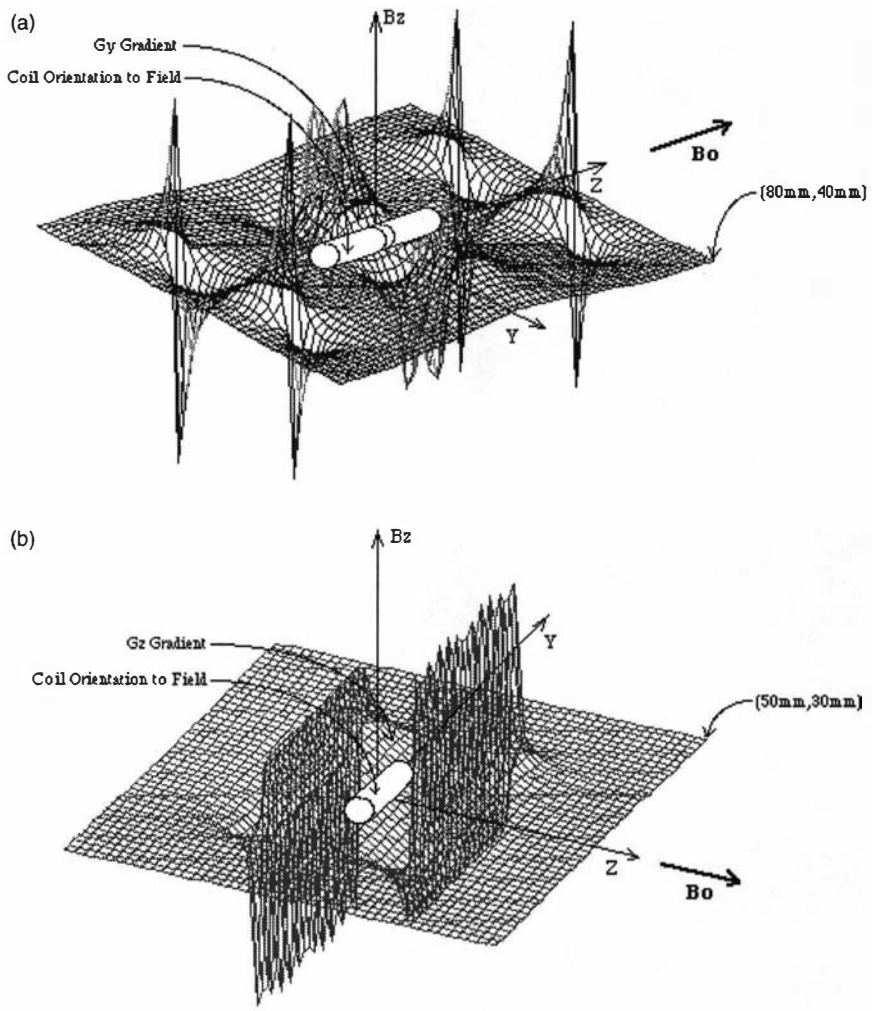

Figure 8.10: (a) The three dimensional field plot of the B_z field component for the dummy saddle coil shows the expected linear gradient at the center of the coil as well as the 'outline' of the coil itself. (b) A similar three dimensional plot to that of the saddle coil for the quadrupole coil, firstly shows the different orientation to the main field B_o and secondly the different current return paths.

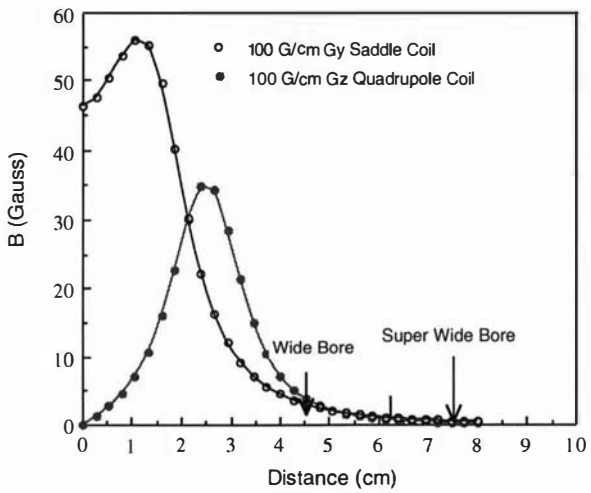

Figure 8.11: Comparative field profiles for saddle and quadrupole coils, operating at 1.0 T m^{-1}, predicts screening is not required for the quadrupole coil at wide bore and superwide bore diameters. At standard bore diameters eddy currents may cause F.I.D. perturbation problems.

8.2.2 The Target-Field Gradient Coil

The quadrupole coil is suitable for the generation of G_x and G_z gradients in the magnetic field[104]. The design of the third gradient (G_y) was undertaken using a target field approach. This involved starting with a desired magnetic field profile and calculating the current distribution that would produce it. Note that in designing G_y we are seeking a field component along the z axis of the polarizing magnet which varies linearly along the y axis. In the frame of reference of the quadrupole coil this is $\frac{\partial B_y}{\partial z}$. We desire our field component to be independent of ρ and azimuthal, ϕ.

From Eqn. (8.23) we can see that there is a direct relationship between the magnetic field component B_y and the current distribution ($J_\phi^m(k)$) at radius a. A less general solution to this equation results when the field component is considered at radius a:

$$\begin{aligned} B_y(\rho,\phi,z) &= \frac{1}{2}\Gamma k a I_m(k\rho)\Big[J_\phi^{m-1}(k)K'_{m-1}(ka) \\ &\quad -J_\phi^{m+1}(k)K'_{m+1}(ka)\Big] \end{aligned} \tag{8.31}$$

It is useful to define an inverse Fourier transform (Eqn. (8.32)) of the B_y field component at a radius c, where $c < a$. This arises from the simplicity with which the F.T. of the magnetic field can be expressed if independent of radius as seen later (Eqn. (8.41).

$$B_y(c,\phi,z) = \frac{1}{2\pi}\sum_{m=-\infty}^{\infty}\int_{-\infty}^{\infty} dk e^{im\phi}e^{ikz}B_y^m(c,k) \tag{8.32}$$

Equating equations (8.31) and (8.32) one obtains:

$$\begin{aligned} B_y^m(c,k) &= \frac{1}{2}\mu_o k a I_m(k)\Big[J_\phi^{m-1}(k)K'_{m-1}(ka) \\ &\quad -J_\phi^{m+1}(k)K'_{m+1}(ka)\Big] \end{aligned}$$

Because of the symmetry of the B_y field component with respect to angle ϕ ($B_y^m(c,k) = 0$ for $m \neq 0$ and $J_\phi^{-m}(k) = -J_\phi^m(k)$) a relationship can be obtained between the first order current density and higher terms:

$$J_\phi^1(k) = \left[\mu_o k a I_o(kc)K'_1(ka)\right]^{-1} B_y^o(c,k) \tag{8.33}$$

$$\Rightarrow J_\phi^m(k) = \frac{K'_1(ka)}{K'_m(ka)}J_\phi^1(k)\left[\sum_{n=-\infty}^{\infty}\delta_{m,2n+1}\right] \tag{8.34}$$

$$\text{using} \qquad B_y^m(\rho,k) = 0,\ m \neq 0 \tag{8.35}$$

It follows from Eqn. (8.34), that only odd 'm' ordered terms are used. Another consequence of the symmetry of the magnetic field, is that the target magnetic

field defined at radius c, is identical for *all* values of r[104]. Now that the $J_\phi^m(k)$ component current distribution can be calculated, the divergence theorem is used to calculate the other current component $J_z^m(k)$.

$$\nabla \cdot \mathbf{J} = 0 \tag{8.36}$$

$$\Rightarrow J_z^m(k) = -\frac{m}{ka} J_\phi^m(k) \tag{8.37}$$

Finally to obtain both current distributions in real space, ie. $J_z(z)$ and $J_\phi(z)$, the inverse Fourier transform of the above current distributions must be calculated:

$$J_z(z) = 2\pi \sum_{m=-\infty}^{\infty} \int_{-\infty}^{\infty} dk J_z^m(k) \tag{8.38}$$

$$J_\phi(z) = 2\pi \sum_{m=-\infty}^{\infty} \int_{-\infty}^{\infty} dk J_\phi^m(k) \tag{8.39}$$

8.2.2.1 The Target Function

From the calculations in the previous section the expressions below for B_y were chosen (see Eqn. (8.40)). The target field function shows a z^7 proportionality, defined at radius c. This type of function has a linear gradient when z is less than the parameter, d, but rapidly diminishes when greater. The parameter, G, is the required gradient strength.

$$B_y(z) = Gz\left[1 + \left(\frac{z}{d}\right)^6\right]^{-1} \tag{8.40}$$

$$F.T. \Rightarrow \quad B_y^m(c,k) = \left[\delta_{m,0}\frac{1}{3}\left(\frac{k}{|k|}\right)d^2\pi G i\right] \times \left[2e^{-\frac{|k|d}{2}}\cos\left(|k|d\frac{\sqrt{3}}{2} + \frac{\pi}{3}\right) - e^{-|k|d}\right] \tag{8.41}$$

The Fourier transform of Eqn. (8.40) is Eqn. (8.41). At larger values of k it can be seen, from Eqn. (8.33) in conjunction with Eqn. (8.41), the first order current distribution $J_\phi^1(k)$ leads to the approximation:

$$J_\phi^1(k) \propto e^{k(a-c-\frac{1}{2}d)} \tag{8.42}$$

$$\text{for } J_\phi(k) \text{ to converge} \quad \Rightarrow \quad c + \frac{d}{2} > a \tag{8.43}$$

Hence if the sum of all m^{th} ordered current distributions is to converge, then a limit is put on the relationship between a, c and d (as seen above). The parameters c and d, which define a cylindrical volume, are optimised to give the best possible gradient homogeneity. Too large a value of d, will produce a current density

outside the physical boundary of the coil. The following values were used:

$$a = 14.0 \text{ mm}$$
$$c = 8.0 \text{ mm}$$
$$d = 19.0 \text{ mm}$$

A plot of the current distributions (Fig. 8.12) in k space, calculated from the

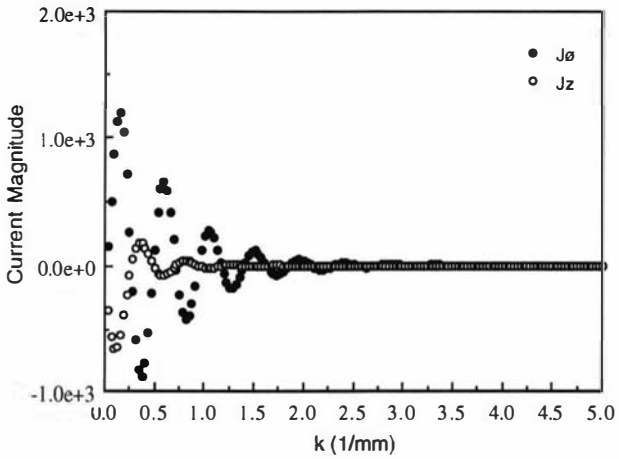

Figure 8.12: Both current distributions (J_ϕ and J_z) are calculated in an inverse space (**k**) for a desired magnetic field distribution. The convergence seen here for large values of k is essential to obtain J_ϕ and J_z in real space, z.

target magnetic field given above, shows both the z and ϕ components converging to zero, as $k \rightarrow \infty$ (Eqn. (8.41)). It is essential that this data is equal to zero at larger values of k, so as to avoid truncation and a 'base line roll' when the F.T. is calculated. Fig. 8.13 shows both of the calculated current distributions in real space (z). It is apparent that as ($J_\phi(z)$) crosses over from a positive to negative value, $J_z(z)$ is a maximum. Also, when J_z is zero for small z, J_ϕ has a maximum value. This type of distribution describes a current arc contour such as that shown in Fig. 8.14(a). Only one octant of the pattern is shown. This contour has been discretised by integrating along the perpendicular to the resultant current distribution, at specified points and dividing these paths into equal magnitudes. These current distributions can then be approximated by discrete wires as shown with in Fig. 8.14(b), again only showing one octant of the pattern, with three wires. The pattern here has been termed a 'moko'[2] pattern. In carrying out the

[2]A 'Māori' facial tattoo.

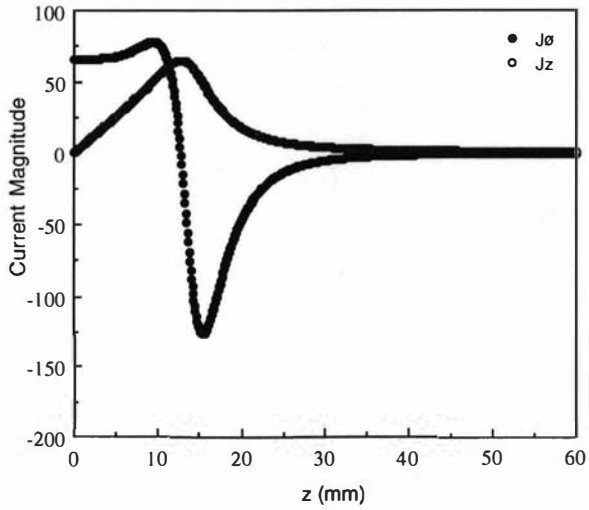

Figure 8.13: The F.T. of the current distributions in Fig. 8.12 produces a current density defined in real space (z), where the direction of y is parallel to B_o.

contour calculations I was greatly assisted by Phillip Back[3].

[3]Postdoctoral fellow, Massey University, Palmerston North, New Zealand.

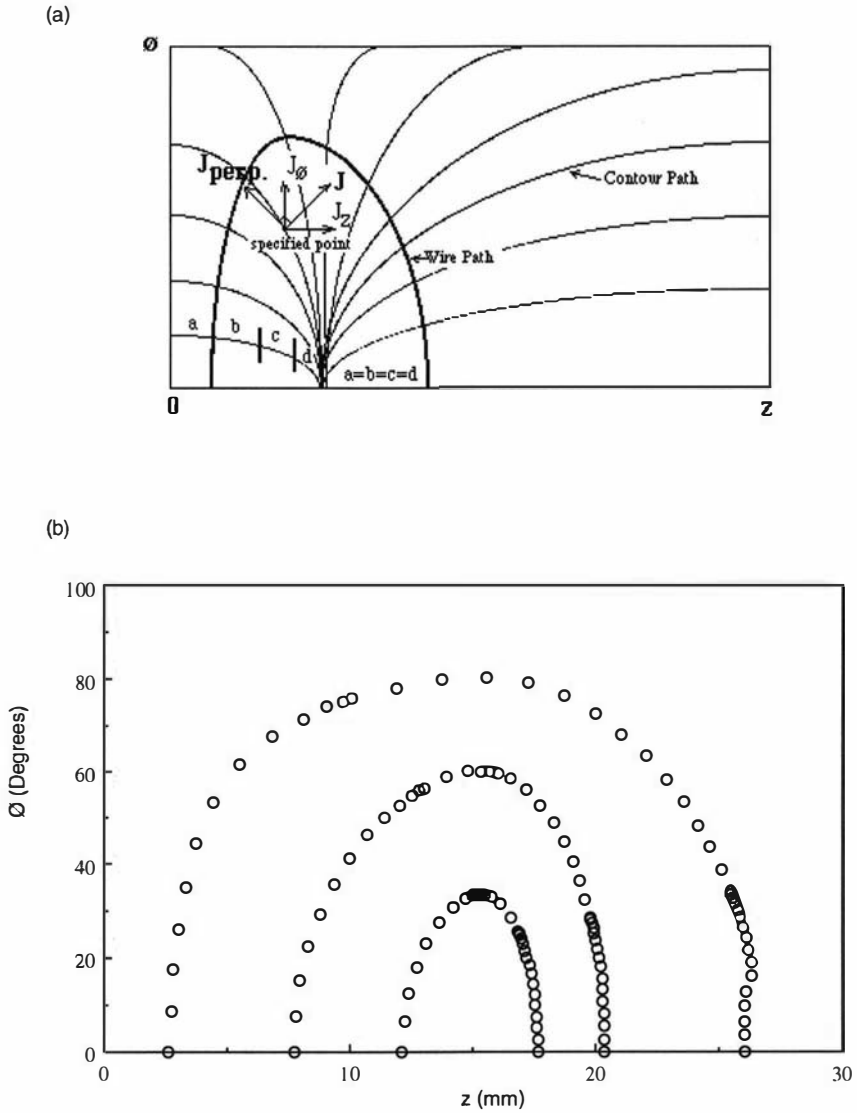

Figure 8.14: (a) From the current distributions defined in Fig. 8.13, discretisation of the currents is obtained by integrating along perpendicular paths to the direction of the current. After this integration, each path is divided equally into the number of discrete current paths desired. (b) A discrete current configuration for one octant is shown consisting of three separate paths.

8.2.2.2 Homogeneity and Gradient Calculations

Again the Biot Savart law was used to perform field calculations for the target field coil. We now adopt the normal NMR axes where the z axis is aligned with the main magnetic field, B_o. The three contour solution for all eight octants was used with the volume of interest being: -5 mm$\leq z \leq +5$ mm and -2 mm$\leq y \leq +2$ mm. A gradient of 3.3×10^{-2} T m^{-1} A^{-1} was calculated with a 0.7 % variation over a 12.5 mm^3 volume. This gradient strength has been achieved with only one discrete wire per contour, over the eight octants.

8.2.2.3 Former Design and Wiring

Both the quadrupole and target field coil contours were milled into a former with an an injected mould weave material called 'tufnol'. The computerised milling for the moko pattern is not described here, but details of this operation can be found elsewhere[105]. Each gradient set in turn was milled with a vertical mill to the required depth. Each groove had a 2.0 $\times$ 2.0 mm width and depth. Wire was then laid in the grooves according to the configuration described on pages 130 and 146. Six wires per contour were used for the wiring of the target coil to increase the expected gradient strength from 3.3×10^{-2} T m^{-1} A^{-1} to approximately 20.0×10^{-2} T m^{-1} A^{-1}.

The wire used was an enameled 24 gauge (0.18 Ω m^{-1}) copper wire. As the wire was being placed into the groove, a small amount of 'super glue' is used to keep it in position. After all the wires are temporarily fixed by this super glue, the groove was then filled in again with '24 hour' epoxy resin. In this last process it is important that no air bubbles should be present to ensure no movement of the wires when being pulsed in the magnetic field. Constant rotation of the former during the curing time of the epoxy resin, ensures that none of the 'problem' air bubbles are present. After the glue is set, the above contour grooving procedure is repeated, but this time for the next gradient set at a shallower depth. A 0.5 mm gap between the next groove and the existing gradient set, ensures that no short circuit is caused by milling through existing wires. The former is supported (Fig. 8.15) by a tufnol cradle with adequate clearance inside the cradle for the r.f. connections. This cradle is again supported by a standard Bruker macor r.f. base for attachment onto a standard Bruker micro imaging probe.

The r.f. tuning circuit consisted of series-parallel arrangement shown in Fig. 8.16, attached to a four winding transverse solenoidal coil. This arrangement

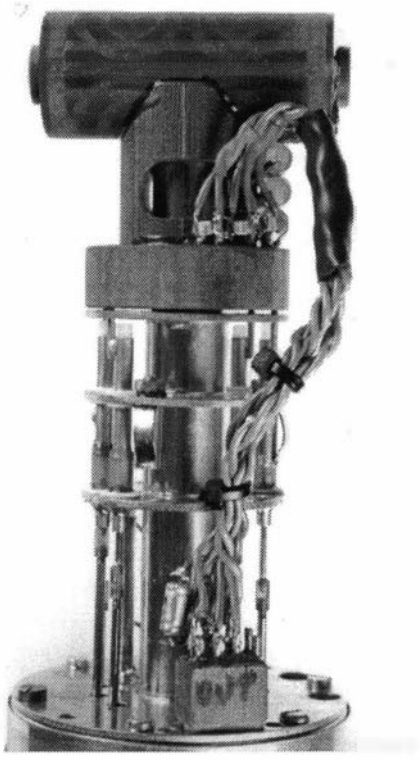

Figure 8.15: To hold the discrete wires in place, grooves are made in a former of Tufnol. The former is positioned on a standard Bruker r.f. holder with the wires fixed in place by epoxy resin.

results in a circuit impedance of the following:

$$z = \frac{R + j(X_L - X_{C_1})}{1 - \frac{X_L - X_{C_1}}{X_{C_2}} + j\frac{R}{X_{C_2}}} \tag{8.44}$$

where R, X_{C_1}, X_{C_2} and X_L are the resistance, reactance of capacitor, C_1, reactance of capacitor, C_2 and reactance of inductor, L, respectively. The circuit is best tuned where $X_{C_1} = X_L$. When $X_{C_2} = R$, the circuit is said to be 'matched'. The r.f. coil was wound around a 1.20 mm OD, 1.00 mm ID glass tube, held in place by two teflon caps located at either end of the gradient coil. The circuit is best tuned to a resonant frequency of 300.136 MHz, at which frequency it has a 'Q' of over 100.

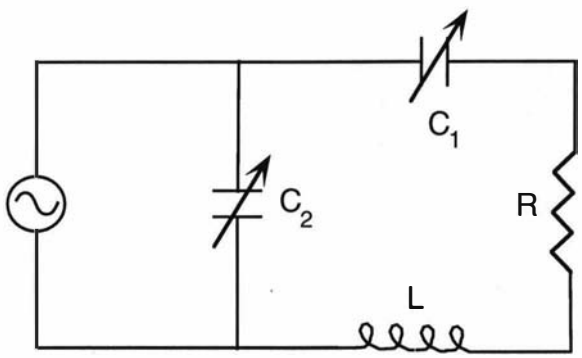

Figure 8.16: The r.f. tuning is a series-parallel circuit with the normal 50 Ω line resistance.

8.2.2.4 Gradient Strength and Eddy Current Testing

Using a tube of water of known dimension as a sample and by measuring the NMR frequency broadening $(\omega_2 - \omega_1)$ associated with the application of each of the gradients in turn, magnitudes (G) of the gradients can be determined as follows:

$$G = \frac{\hbar(\omega_2 - \omega_1)}{\gamma I r}$$

I is the applied current and r is the (known) radius of the sample.

To obtain three orthogonal projections through a 5.0 mm ID test tube of doped[4] water, a 300 MHz AMX spectrometer with a wide bore super conducting magnet was used. Magnitudes of all three gradients are shown in table 8.1.

	Current (A)	Sample Width (mm)	Freq. Width (kHz)	Grad. Magnitude (T m^{-1} A^{-1})
G_x	0.87	5.0	35.0	0.190
G_y	2.97	2.0	50.0	0.198
G_z	0.95	5.0	40.0	0.197

Table 8.1: Gradient magnitudes for the quadrupole and target field coils determined by the frequency spread of proton nuclei on application of a gradient.

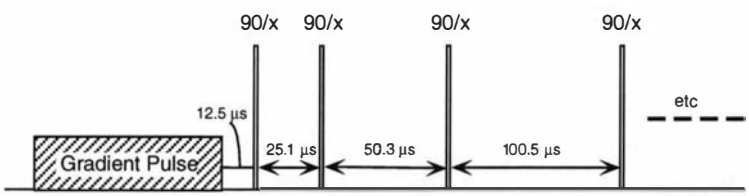

Figure 8.17: The above pulse sequence samples an F.I.D. at different time intervals after the application of a gradient pulse.

Eddy current testing was performed at Bruker using a 270 MHz spectrometer with a wide bore vertical magnet. A pulse sequence was used consisting of a gradient pulse followed by eight 90° pulses (Fig. 8.17), of delay times: 12.5, 25.1, 50.3, 100.5, 201.0, 402.0, 804.1, 1000.2 μs. If the gradient were not pulsed, eight identical F.I.D.'s would be obtained, as no perturbation of B_o would occur (refer to page 140). Identical F.I.D.'s (even down to a delay time of 25.0 μs) were obtained

[4]Doped water is distilled water with copper sulphate added to reduce the relaxation time, T_1.

	Inductance (μH)	Resistance (Ω)
G_x	70	1.4
G_y	20	0.7
G_z	18	1.0

Table 8.2: The quadrupole-target-field coil show low inductances for all three gradients. These inductances were measured at 1.0 kHz.

with the G_x gradient being pulsed at 1.0 T m^{-1}. Similarly for the G_y and G_z gradients, eddy current tests reveal the same minimum delay is obtained. These comparatively short recovery times obtained for the gradients support previous calculations on page 139, where it was suggested that eddy currents would not be a significant problem in a wide bore geometry when pulsed at 1.0 T m^{-1}.

As mentioned earlier one of the advantages of the quadrupole coil is the low inductance it achieves, thus the coil can be operated at lower driving voltages. Inductance measurements of each three gradients were achieved at a frequency of 1.0 kHz using a *Hewlett Packard HP 4192A LF impedance analyser*. These inductances are summarized in table 8.2 along with the coils' resistances. The G_y gradient shows a similar magnitude to that of the other gradients.

8.3 High Spatial Resolution & Double Phase Encoding

The ultimate limit to resolution in nuclear magnetic resonance is determined by the intrinsic signal-to-noise ratio[106]. In principle the best resolution is achieved, since the noise power is dependent upon the acquisition bandwidth, where the minimum bandwidth is comparable to the intrinsic linewidth ($[\pi T_2]^{-1}$)[54]. However two types of limitations can intervene before the above takes place. In particular, diamagnetic susceptibility inhomogeneity may broaden the linewidth well in excess of $[\pi T_2]^{-1}$. Molecular self-diffusion, in the presence of applied and local susceptibility gradients, will further attenuate the NMR signal. While the two effects are fundamentally different in their influence upon signal-to-noise, the techniques for avoidance are similar.

8.3.1 Susceptibility Effects

The details of susceptibility and diffusion effects, as they pertain to NMR microscopy, can be found elsewhere[107]–[109]. Only a summary shall be given here.

The field variations caused by susceptibility variations cause a local precession frequency offset, $\gamma \Delta B_o(\mathbf{r})$, which is superimposed on the frequency spread caused by applied gradients. The effect of $\Delta B_o(\mathbf{r})$ is dependent upon the exact imaging pulse sequence employed. For the usual phase-frequency spin-echo type of Fourier imaging shown in figure 8.18 (a), the signal amplitude may be written as:

$$S(k_x, k_y) = \int\int \rho(x,y) e^{i2\pi k_x (x + \Delta B_o(x,y)/G_x)} e^{i2\pi k_y y} dx dy \qquad (8.45)$$

where G_x and G_y are the read-gradient and phase gradient amplitudes, respectively. The k space components are k_x and k_y given by $(2\pi)^{-1}\gamma G_x t_x$ and $(2\pi)^{-1}\gamma G_y t_y$ respectively. The effect of the field offset, ΔB_o, in equation (8.45), is to displace the original object's elements by $\Delta B_o(x,y)/G_x$ in the direction of the read gradient while phase gradient effects are absent. The distortion length scale is characterised by the parameter, Δx_{local}. An inherent phase modulation, caused by the phase gradient, is also evident with the above type pulse sequence. As spin echoes have been used here, the phase differences are refocussed, hence the omission of such a term in equation (8.45).

In contrast with phase-frequency encoding, the use of phase-phase encoding (Fig. 8.18 (b)) leads to an apparent lack of image distortion when the signal amplitude is examined for this different pulse sequence:

$$S(k_x, k_y) = \int\int \rho(x,y) e^{i2\pi(k_x x + k_y y)} e^{i\gamma \Delta B_o(x,y) t} dx dy \qquad (8.46)$$

What is evident in equation (8.46) is the phase modulation caused by *both* phase gradients. One is reminded that, as with phase-frequency encoding (Eqn. (8.45),

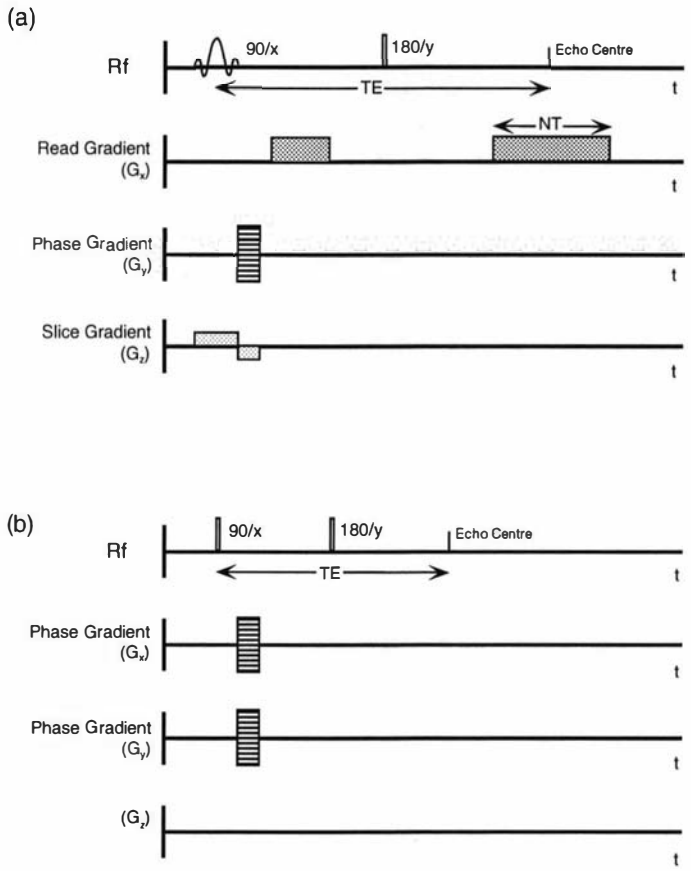

Figure 8.18: (a) The spin echo, phase-frequency pulse sequence is vulnerable to image distortion when susceptibility field offsets are present. (b) The phase-phase encoding pulse sequence, on the other hand, avoids image distortion when subjected to field offsets caused by susceptibility differences.

the phase modulation for phase-phase encoding is again refocussable if spin echoes are employed. In the event of not using spin echoes, such as when acquiring a signal immediately after the application of a phase gradient to reduce T_2 effects, the resultant local phase shifts may cause destructive interference if a sufficient phase difference occurs across a pixel. Such a null will cause attenuation of the signal, a term we have called 'phase smearing'. This effect can be avoided if a 'modulus' of the image is taken, as well as the applied maximum gradient, G_{max}, being a lot larger than local inhomogeneity gradients caused by the original field offset, $\Delta B_o(x, y)$ (ie. $\Delta B_o(x, y) \ll G_{max}[107]$).

The phase-phase encoding system requires a longer experimental time because of its N^2 phase encoding steps, in contrast to the phase-frequency method which

requires N phase encoding steps. In terms of signal-to-noise however, the experiments are equivalent[107].

8.3.2 Diffusive Effects

The unrestricted diffusion of molecules in the presence of spatially dependent magnetic fields, induces phase shifts in the spin transverse magnetisation (Sec. 3.2.3.1). This effect can cause loss of signal intensity which ultimately can limit the spatial resolution, since increasing spatial resolution requires progressively larger gradients.

8.3.2.1 Homogeneous Systems

The resultant attenuation, A, associated with the application of a steady uniform gradient, G, for time t, with diffusion coefficient, D, is[110]:

$$A = e^{-\frac{1}{3}\gamma^2 DG^2 t^3} \tag{8.47}$$

$$\Rightarrow \quad A_p(k_y) = e^{-\frac{1}{3}\gamma^2 DG_y^2 t^3} \tag{8.48}$$

$$= e^{-\frac{4}{3}\pi^2 Dk_y^2 t} \tag{8.49}$$

$$\Rightarrow \quad A_{pp}(k_x, k_y) = e^{-\frac{4}{3}\pi^2 Dk^2 t} \tag{8.50}$$

For the case of phase-frequency encoding, the phase gradient would result in the attenuation factor of equation (8.49). A similar term is found for double phase encoding (Eqn. (8.50)). The k-dependent nature of the phase-phase attenuation, leads to blurring of sharp features of an image, but no loss of average image amplitude occurs since there is no attenuation at $k = 0$. The blurring can be reduced if a larger gradient is applied, thus reducing the applied time, proportionately.

The influence diffusion has for a phase-frequency encoding scheme shown in figure 8.18 (a) is two-fold. Firstly, the same diffusive phase term is evident (Eqn. (8.49)) as found in the phase-phase scheme. This is expected and is again reduced if larger gradients and shorter application times are sought. Secondly, a more dramatic effect is seen with the application of the read gradient in the presence of diffusion where attenuation of the signal occurs when $k_x = 0$:

$$A_f(0) = e^{-\frac{4}{3}\pi^2 D{k_{max}}^2 (NT)} \tag{8.51}$$

To gauge the effectiveness of the term in equation (8.51) it is useful to note that $2D{k_{max}}^2(NT)$ is equivalent to $(\Delta x_{diff}/\Delta x_{pixel})^2$, where Δx_{pixel} is the pixel width and Δx_{diff} is the RMS distance diffused over the time interval NT. Thus for a given pixel size the effect of diffusive attenuation decreases with increasing bandwidth.

8.3.2.2 Heterogeneous Systems

In the previous section it was assumed that the gradient, G, and diffusion coefficient, D, where homogeneous throughout the sample. This assumption is somewhat idealistic as demonstrated by susceptibility field offsets which vary locally within a sample. Where these inhomogeneities are present, diffusive effects will be strongly modulated by local fields. The relative parameters for diffusive effects with uniform local fields were $\Delta x_{diff}/\Delta x_{pixel}$. Providing the read and local gradients' magnitude are comparable, a superposition of these gradients can cause site specific null points in real space. These points will cause bright features in the image.

In contrast the phase gradients' (Fig. 8.18 (b)) diffusive effects can be summarised in a point-spread function (PSF, Eqn. (8.52)), the details of which can be found elsewhere[107].

$$\begin{aligned} PSF(\mathbf{r}') &= \left(\frac{3}{16\pi Dt}\right)^{\frac{3}{2}} e^{-\frac{3\mathbf{r}'^2}{16DNT}} \\ &\quad \times e^{-i\gamma\frac{11}{8}\mathbf{G}^{loc}(\mathbf{r})\cdot\mathbf{r}'t} \\ &\quad \times e^{-\frac{7}{48}\gamma^2 G^{loc}(\mathbf{r})^2 Dt^3} \end{aligned} \tag{8.52}$$

where $\mathbf{G}^{loc}(\mathbf{r})$ is the local gradient at element $\mathbf{r}$, to which $\mathbf{r}'$ are adjacent and $t = NT/2$. The main features of the PSF are a result of the diffusive attenuation null points occurring in k space. This leads to the PSF containing a Gaussian of width of order $\sqrt{\frac{16}{3}Dt}$ and a spatially modulated phase roll associated with the local field offset. If the susceptibility-related local field causes a shift, Δx_{local}, which is comparable with the pixel dimension, strong diffusive modulation may occur depending on the relative magnitudes of local and applied gradients. In particular when $G^{loc} \simeq G^{max}(\Delta x_{diff}/\Delta x_{pixel})$ cancellation of the image intensity can occur.

8.3.3 Experimental Setup

The microimaging experiments described here were completed using a Bruker AMX 300 MHz spectrometer in conjunction with a 7 T wide bore superconducting magnet. The quadrupole-target field gradient coil, described earlier in section 8.2.2.3, was used here also. The coil was positioned on a standard Bruker microimaging probe, and with the 30 A available from our current amplifiers, offered a maximum gradient of around 6 T m^{-1} (600 G cm^{-1}). This magnitude of gradient proved more than sufficient for the imaging experiments described here.

In order to demonstrate the effects that susceptibility differences within a sample have on NMR images, a model phantom was constructed consisting of a

glass cylinder of 300 μm inserted in a glass tube with an inner diameter of 1600 μm. The intervening space was filled with acetone, giving a susceptibility difference of around 2.6 ppm.

The plant work described here used a section (leaf stem) of a geranium petiole in which both ends were sealed with wax to prevent drying. The stem consists of an outer epidermis layer surrounding cortex cells, typically 10 to 50 μm in diameter. The cortex contains many intercellular airholes, typically 10μm diameter, as do the much larger parenchyma cells (40 to 50 μm diameter) in the center of the stem. The vascular bundles contain both xylem and phloem. The stem was soaked in a water solution containing 0.1 % (w/v) copper sulphate which had been added to reduce T_1.

8.3.4 Experimental Results

Figure 8.19 shows the 'susceptibility phantom' images acquired using a standard spin-echo pulse sequence (refer Fig. 8.18 (a)) under two different acquisition bandwidths. The images have a field of view of 2.5 mm, slice thickness of 2000 μm and a 128^2 resolution. A slight asymmetric distortion of the glass cylinder is noticed with the image collected at 10 kHz. The '5 kHz image', in contrast, reveals strong distortion with the known circular glass cylinder 'transformed' into an 'arrowhead' arrangement. The 5 kHz bandwidth corresponds to a 0.47 T m^{-1} read gradient with TE being of the order of 30 ms. Both images reveal low signal-to-noise ($\simeq$ 2.5) caused by T_1, T_2 and diffusion effects. The latter processes are discussed in detail in section 8.3.2, in particular the null gradient points that exist with phase-frequency imaging. These points are clearly visible in figure 8.19 (b) where three high intensities are located around the arrowhead.

In order to show the effectiveness of double phase encoding with regards to avoiding susceptibility and diffusion artifacts, an image was obtained of the same glass/acetone sample as above using the pulse sequence shown in figure 8.18 (b). As seen in figure 8.19 (c) not only has image distortion been avoided but the image has an apparent increase in signal-to-noise ($\simeq$ 24). The reason for the latter improvement is two-fold; firstly the image was acquired with a phase time, t_y, of 1 ms with corresponding gradient magnitude of 1.20 T m^{-1}. Because the influence gradients have in the phase-phase encoding scheme is simply one of image blurring, the image has avoided diffusive attenuation from the uniform gradients. Secondly the echo time, TE, for this second experiment is only of the order of 10 ms. This short time has the advantage of reducing T_2 relaxation. In practice a small read gradient (0.09 T m^{-1}) is applied during the acquisition of the signal. This was carried out to counteract the effect of small echo fluctuations, caused by

gradient instabilities. These fluctuations were found to give rise to severe local attenuation within the images. The read gradient has been scaled to give a slice thickness of 2000 μm to allow direct comparison to the phase-frequency image found in figure 8.19 (a), (b).

A similar comparison of phase-frequency and double phase encoding schemes is shown in figure 8.20 where 128^2 pixel images are compared for the case of the plant stem. The susceptibility distortion artifacts have been avoided with the phase-frequency image (Fig. 8.20 (a)) because of the large acquisition bandwidth of 100 kHz. Again, as above, the slice thicknesses have been scaled with the geranium images to coincide. The double phase encoding image (Fig. 8.20 (b)) again shows an enhanced signal from the geranium stem. A similar cause to the increase in signal for the glass/acetone experiment is given for the observation here.

As a consequence of the lack of the read gradient in the double phase encoding pulse sequence (as depicted in Fig. 8.18 (b)) the third dimension, in the three dimensional experiment, is frequency. If the artifacts associated with echo instabilities caused by read gradient absence, as described above, are not present, the additional frequency domain can be beneficial in selecting chemical shift species. For example, the same 5.0 % (w/v) PEO/H_2O solution described in chapter 4, was used to replace the acetone around the glass cylinder described earlier. A 300 Hz separation is found between the PEO and H_2O protons. Double phase encoding images, without the application of a read gradient, revealed a distinct separation of the protons detected from the PEO polymer and that of the water. A summation of these two chemical species is shown in figure 8.21. Note again with these images the lack of pixel distortion and relatively good signal-to-noise achieved.

To investigate severe diffusive attenuation caused by phase encoding in conjunction with inhomogeneous local gradients, a glass/water susceptibility sample was prepared with a glass cylinder and tube as before. A phase encoding time of 50 ms was applied with corresponding image shown in figure 8.22 (a). An additional susceptibility difference is noted with this image at the bottom-right of the tube, manifesting itself as a high intensity region. This anomaly should be ignored as it is caused by dust impurities within the water. Using equation (8.52), calculated attenuated images were produced using an estimated susceptibility difference between silica glass/water of 0.7 ppm and diffusion coefficient of water of 2.5×10^{-9} m^2 s^{-1}. These images are shown in figures 8.22 (b), (c) incorporating real and imaginary components respectively. It must be noted the bright thin line at the center of the image is a calculation artifact. Lastly, figure 8.22 (d) shows the modulus of figures 8.22 (b) and (c). The comparison of images (a) and (d) are

quantitatively good.

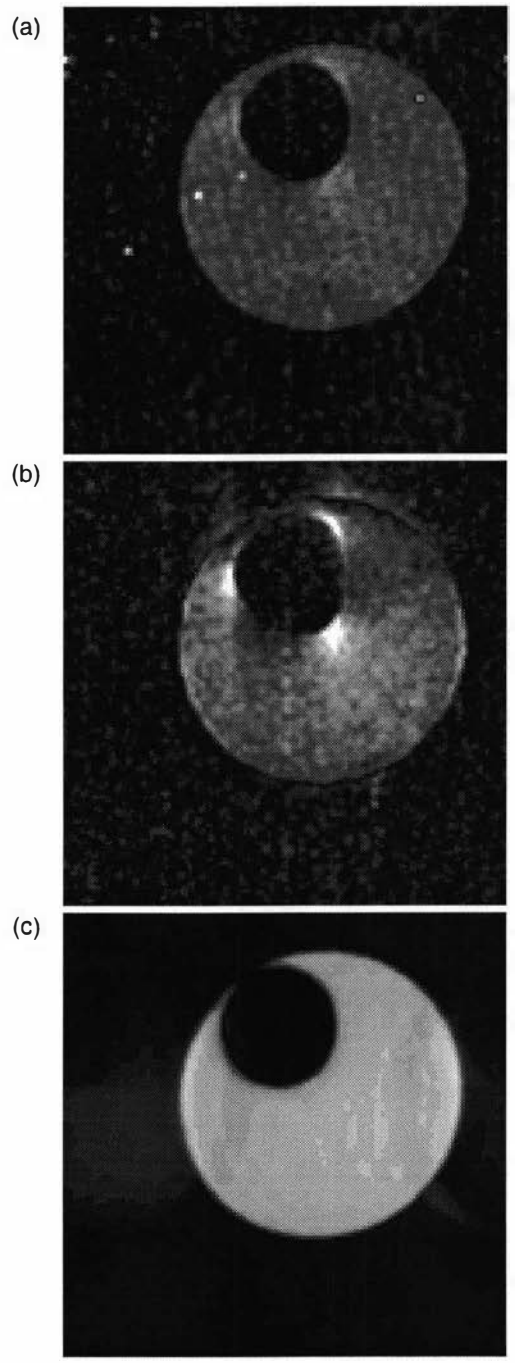

Figure 8.19: (a) The spin echo, phase-frequency pulse sequence images were collected at an acquisition bandwidth of 10 kHz and (b) 5 kHz. Gradient cancellation is evident with the three high intensity points around the distorted image of the glass cylinder. (c) The same image collected with double phase encoding shows an absence of image distortion and a reduction in diffusive attenuation.

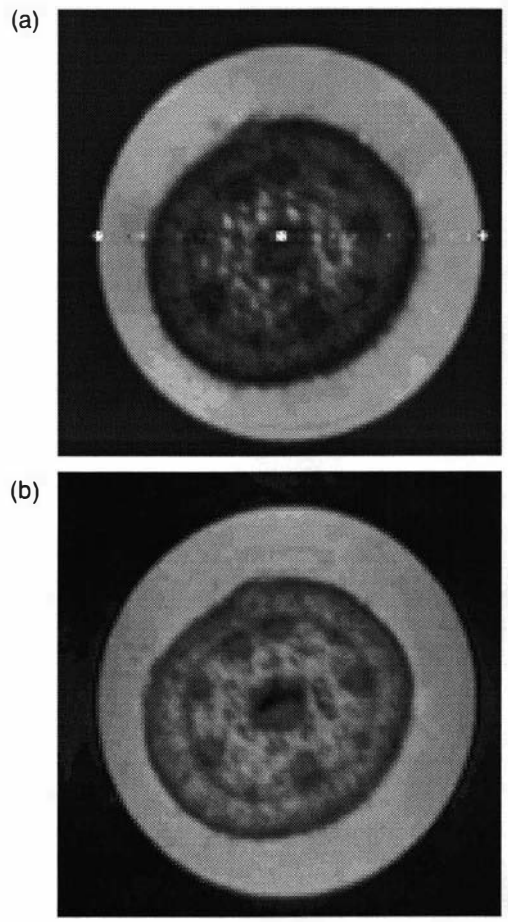

Figure 8.20: (a) Phase-frequency spin echo image of a geranium stem soaked in doped water. (b) The same stem imaged with a double phase encoding scheme.

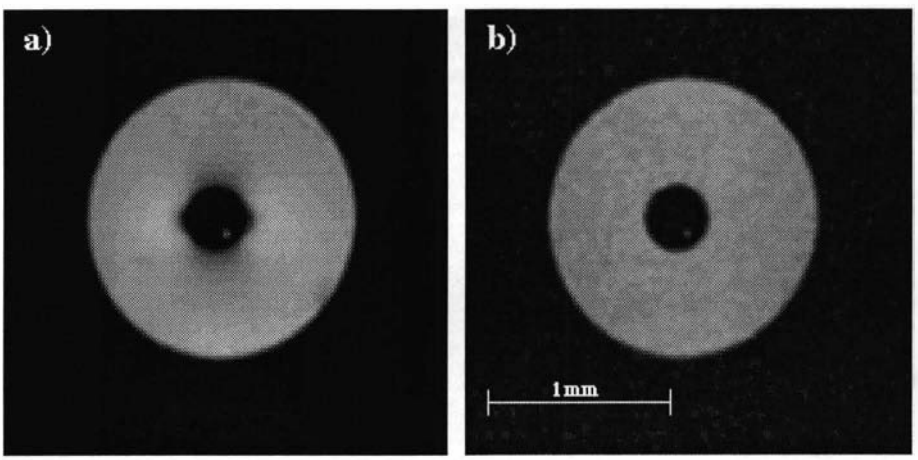

Figure 8.21: (a) Double phase encoding, without the application of a stabilising read gradient, produces chemical selective images of water and (b) PEO in a PEO/H_2O solution.

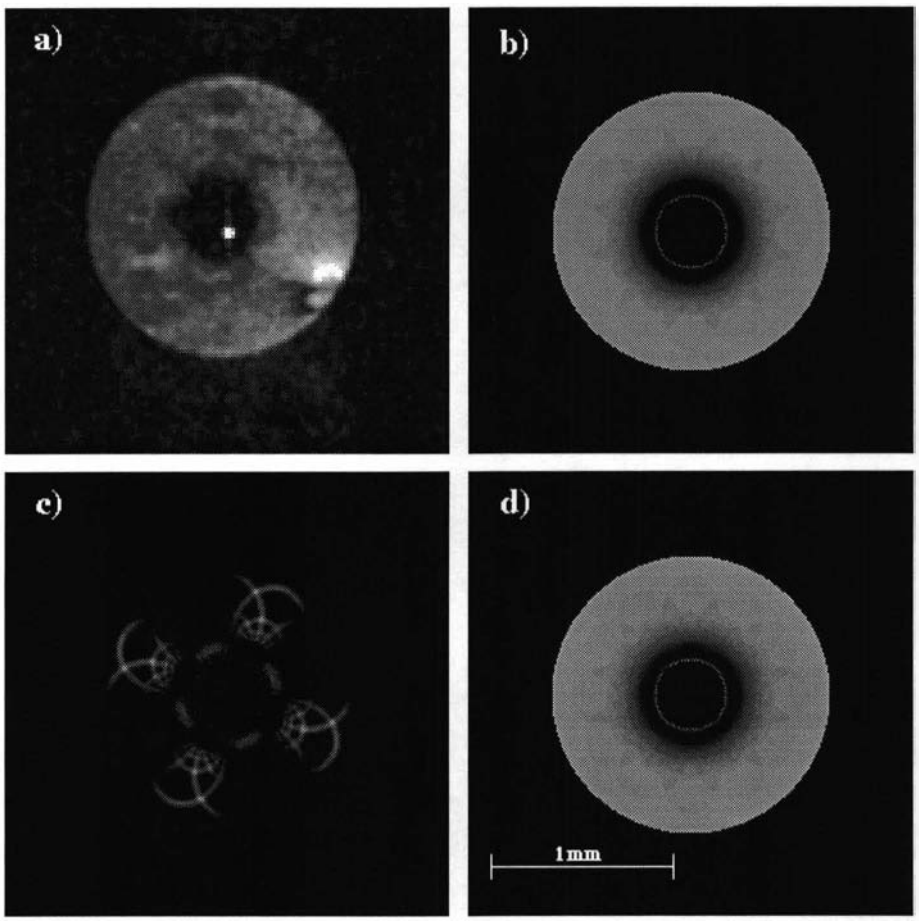

Figure 8.22: (a) A phase encoding time of 50 ms ensured a comparatively large diffusive attenuation was achieved with the glass rod/water sample. (b) The real, (c) imaginary and (d) modulus calculations, using equation (8.52), show a promising likeness when images (a) and (d) are compared.

8.4 Conclusions

The production of an integrated gradient coil containing three orthogonal gradients, each producing gradients of up to 6.0 T m^{-1}, has been achieved with the desired homogeneity and eddy current specifications.

Large magnetic field gradients can be beneficial in eliminating susceptibility artifacts if double phase encoding schemes are employed. The additional time required for such an experiment can be offset with the improvement of signal-to-noise. Diffusive artifacts can be reduced also with phase-phase encoding, providing the applied gradients are larger than local gradients caused by inhomogeneities.

Chapter 9

Future Directions

In this chapter suggestions will be given for possible future experiments that would complement the work presented earlier. In most cases the following suggestions were intended to be an integral part of the study presented in this thesis, but time restrictions prevented this. The following additional comments can be classified into two broad categories; revisiting experiments presented in this thesis and new experiments.

9.1 Revisiting Experiments

Experiments similar to those presented in this thesis, could be performed with improvements which would enable additional investigations. Following is a revisitation of experiments found in the various previous chapters.

Included in the velocity measurements of polyethylene oxide (PEO) solutions (Ch. 4) was a study investigating the center-of-mass diffusion of PEO for various concentrations. In particular, the critical concentration, c^*, at which the polymers became entangled was sought. This process manifested itself as an abrupt decrease in diffusion magnitude as the concentration was increased. A more conclusive investigation of this 'entanglement concentration' could be achieved if more data points were obtained around the 1-2 % (w/v) concentration. An ideal study could include more diffusion data well below 1 % concentration.

The chemical selective imaging of both PEO and water (Sec. 4.2) revealed a similar normalised signal amplitude when the sample was sheared at 30 s^{-1}. It may be more fruitful to search for the migration of PEO and water molecules at larger shear rates. This study will require the use of smaller capillary pipes, thus higher resolution images will have to be employed. These experiments could take advantage of the quadrupole gradient coil, described in chapter 8, which will allow a tube diameter of 1.0 mm or smaller. Close attention should be made to

acquiring images of the boundary of the tube wall. It must be mentioned that similar preliminary experiments have been completed but not included in this thesis because of poor data quality.

A question arises with the rheological data presented in this thesis as to the difference, if any, between the slip and spurt phenomena. As seen in chapter 6, at higher flow rates the enhanced shear rate of the CPyCl/NaSal wormlike micelle, close to the capillary wall, developed into a flow profile akin to the slip phenomenon. As a result of this development, the question emerges as to whether Xanthan gum solutions also follow a similar flow development. The slip experiments, performed on Xanthan solutions, could be repeated with the emphasis of the study toward collecting low shear rate velocity data. Perhaps an intermediate flow behavior could be found. It must be noted that a clear difference between the slip and spurt phenomena has been postulated in this thesis, stating boundary and bulk fluid properties respectively. The low shear rate experiments would hopefully support the above postulates.

The study of the amount of slippage of Xanthan solutions (Sec. 5.4.2), and its dependence upon reservoir/capillary diameters, is not conclusive and requires further velocity measurements with more W/D combinations.

The hysteresis effect of wormlike micelles, mentioned in section 2.3.2, could be examined utilising velocity profiles in capillary geometry. Careful flow rate adjustments would have to be made approaching the unstable flow rate from below and above. Also, further analysis is needed of the behavior of CPyCl/NaSal wormlike micelles under the influence of *higher* shear rates. The theory of the 'shear band's' spatial increase with increasing shear rate could be verified. Again, as with the proposed higher shear rate study of Xanthan solutions, smaller capillary pipes, in conjunction with the quadrupole gradient coil, could be used.

Although extensive research has been completed on the echo instability of the double phase encoding pulse sequence, further exploration is required to find the cause for such anomalies. In particular, careful mapping of the susceptibility fields is needed, as the orientation of the glass cylinder/acetone sample is maneuvered from a position perpendicular to B_o, to parallel. The changes to image's attenuation as a result to the rod's orientation may prove an interesting clue to the source of the instabilities.

9.2 New Experiments

The different rheometer geometries presented in this thesis offer a variety of stress variations. For example, the linear variation provided with the pipe and the more

'gentle' stress variation ($\frac{1}{r}$) observed with the cylindrical-Couette. Throughout this thesis, various assumptions have been incorporated into the research. One in particular is the shear rate homogeneity with the cone-and-plate rheometer. Because of the unique orientation and cone-plate arrangement, it is postulated that shear rate of the sample will have no radial dependence. This postulate should be verified using careful velocity measurements of the combined cylindrical-Couette-cone-and-plate rheometer described in section 3.4.3. Naturally measurements should be concentrated on the cone-and-plate region of the rheometer.

Other geometries for rheometers should also be investigated, including extensional flow. The research in this thesis has concentrated on shear type stresses and would be complimented with further study with extensional stresses. The rheometer could be assembled using finely bored jets, each propelling its fluid toward the other. This unique arrangement would provide a topographical map of stress components.

Finally, as mentioned in chapter 8, measurement of other order parameters, which are sensitive to molecular alignment, would be beneficial to the studies presented here. These include proton dipolar and deuterium quadrupolar interactions which could be incorporated while the sample molecules are being subjected to a stress or strain-controlled experiment. Again, the quadrupole gradient coil would be useful to obtain the gradient strength required for spatial localisation of a deuterium image.

Bibliography

[1] Tanner R.I. *Engineering Rheology.* Oxford University Press, New York, (1985).

[2] Ferry J.D. *Viscoelastic Properties Of Polymers -Third Edition.* John Wiley and Sons, Inc., New York, (1980).

[3] Segré G. and Silberberg A. *J. Fluid Mech.*, **14**, 136 (1962).

[4] Hoffman H. and Rehage H. *J. Phys. Chem.*, **92**, 4712 (1988).

[5] Berret J.F., Roux D.C., Porte G., and Linder P. *Europhysics Letters*, **32**, 137 (1995).

[6] Porges K.G.A., Cox S.A., Herzenberg C., and Kampschër C. *J. Fluid Eng.*, **111**, 337 (1989).

[7] Gao P. and Mackley M.R. *Polymer*, **35**, 5210 (1994).

[8] Hoppler H. U., Dinkel A., and Tomka I. *Polymer*, **36**, 3809 (1995).

[9] Brunn P.O., Durst F., and Wunderlich A.M. *J. Non-Newt. Flui. Mech.*, **22**, 381 (1987).

[10] Weigel R., Lauger J., Richtering W., and Lindner P. *J. Phys. II France*, **6**, 529 (1996).

[11] Nakatani A.I., Poliks M.D., and Samulski E.T. *Macromolecules*, **23**, 2686 (1990).

[12] Xia Y. and Callaghan P.T.C. *Macromolecules*, **24**, 4777 (1991).

[13] Christensen R.M. *Theory of Viscoelasticity - An introduction.* Academic Press, New York, (1982).

[14] Wagner M.H. *Rheol. Acta*, **15**, 136 (1976).

[15] Cohen Y. PhD thesis, University of Delaware, (1981).

[16] Green H. *Proc. Am. Soc. Test. Mater. II*, **20**, 451 (1920).

[17] Scott-Blair G.W. *J. Rheol.*, **1**, 127 (1930).

[18] Reiner M.J. *J. Rheol.*, **2**, 337 (1931).

[19] Mooney M. *J. Rheol.*, **2**, 210 (1931).

[20] Toms B.A. *J. Colloid Sci.*, **4**, 511 (1949).

[21] Wales J.L.S. *J. Polym. Sci. Polym. Symp.*, **50**, 469 (1975).

[22] Cohen Y. and Metzner A.B. *Macromolecules*, **15**, 1425 (1982b).

[23] Pérez-González J. and de Vargas L. *Rheol. Acta.*, **31**, 83 (1992).

[24] Gibbs S.J. *J. Rheol.*, **40(3)**, 425 (1996).

[25] Kiljański T. *Rheol. Acta.*, **28**, 61 (1989).

[26] Schlegal H. *Rheol. Acta*, **19**, 375 (1980).

[27] Bagley E.B., Cabot I.M., and West D.C. *J. Appl. Phys.*, **29**, 109 (1958).

[28] Vinogradov G.V. *Rheol. Acta.*, **12**, 273 (1973).

[29] McLeish T.C.B. and Ball R.C. *J. Polym. Sci. Part B:Polymer Physics*, **24**, 1735 (1986).

[30] Tordella J.P. *Rheology Theory and Applications, Eirich F. Ed.* Academic Press, New York, (1969).

[31] de Pablo J.J., Ottinger H.C., and Rabin Y. *J. AIChE*, **38**, 273 (1992).

[32] Ross-Murphy S.B., Morris V.J., and Morris E.R. *Farraday Symp. Chem. Soc.*, **18**, 115 (1983).

[33] Chauveteau G. *J. Rheol.*, **26**, 111 (1982).

[34] Stockmayer W.H. and Kurata M. *Adv. Polym. Sci.*, **3**, 196 (1963).

[35] Flory P.J. *Principles of Polymer Chemistry.* Cornell University Press, Ithaca, New York, (1953).

[36] Flory P.J. *Statistical Mechanics of Chain Molecules.* Interscience, New York, (1969).

[37] Rouse P.E. Jr. *J. Chem. Phys.*, **21**, 1272 (1953).

[38] Doi M. and Edwards S.F. *The theory of polymer dynamics.* Oxford University Press, Oxford, (1987).

[39] McLeish T.C.B. and Ball R.C. *J. Polym. Sci.*, **24**, 1735 (1986).

[40] Hoffman H. et al. *Ber. Bunsen-Ges. Phys. Chem.*, **85**, 255 (1981).

[41] Hoffman H., Rehage H., and Wunderlich I. *Rheol. Acta.*, **26**, 532 (1987).

[42] Hoffman H. and Rehage H. *Mol. Phys.*, **74**, 933 (1991).

[43] Bloch F., Hansen W.W., and Packard M. *Phys. Rev.*, **70**, 474 (1946).

[44] Purcell E.M., Torrey H.C., and Pound R.V. *Phys. Rev.*, **69**, 37 (1946).

[45] Anderson P.W. and Weiss P.R. *Rev. Mod. Phys.*, **25**, 269 (1953).

[46] Lauterbur P.C. *Nature*, **242**, 190 (1973).

[47] Mansfield P. and Grannell P.K. *J. Phys C*, **6**, L422 (1973).

[48] Mansfield P. and Morris P.G. *NMR Imaging in Biomedicine.* Academic Press, New York, (1982).

[49] Morris P.G. *NMR Imaging in Biology and Medicine.* Oxford University Press, Oxford, (1986).

[50] Ernst R.R. *Principles of Nuclear Magnetic Resonance in One and Two Dimensions.* Claredon Press, Oxford, (1987).

[51] Bottomley P.A. *Rev. Sci. Instr.*, **53**, 1319 (1982).

[52] Ernst R.R. *Q. Rev. Biophysics*, **19**, 183 (1987).

[53] Bailes D.R. and Bryant D.J. *Contemp. Phys.*, **25**, 441 (1984).

[54] Callaghan P.T. *Principles of Nuclear Magnetic Resonance Microscopy.* Clarendon Press, New York, (1993).

[55] Lauterbur P.C. *Pure Appl. Chem.*, **40**, 149 (1974).

[56] Lauterbur P.C., Kramer D.M., House W.V., and Chen C.N. *J. Am. Chem. Soc.*, **97**, 6866 (1975).

[57] Lauterbur P.C. *NMR in Biology.* Academic Press, London, (1977).

[58] Lauterbur P.C. *IEEE Trans. Nucl. Sci.*, **NS26**, 2808 (1979).

[59] Kumar A., Welti D., and Ernst R.R. *Naturwiss.*, **62**, 34 (1975).

[60] Kumar A., Welti D., and Ernst R.R. *J. Magn. Reson*, **18**, 69 (1975).

[61] McCall D.W., Douglass D.C., and Anderson E.W. *Ber. Bunsenges. Physik. Chem.*, **67**, 336 (1963).

[62] Stejskal E.O. and Tanner J.E. *J. Chem. Phys.*, **42**, 288 (1965).

[63] Karger J. and Heink W. *J. Magn. Reson.*, **51**, 1 (1983).

[64] Stejskal E.O. *J. Chem. Phys.*, **43**, 3597 (1965).

[65] Wang M.C. and Uhlenbeck G.E. *Rev. Mod. Phys.*, **17**, 323 (1963).

[66] Y. Xia. *Dynamic NMR Microscopy.* PhD thesis, Massey University, (1992).

[67] Rofe C.J., Lambert R.K., and Callaghan P.T.C. *J. Rheol.*, **38(4)**, 875 (1994).

[68] Mansutti D. and Rajogopal K.R. *Int. J. Non-Lin. Mech.*, **26(5)**, 769 (1991).

[69] Subramanian V., Hoseney R.C., and Bramel-Cox P. *Cereal Chemistry*, **71(3)**, 272 (1994).

[70] Gingrich W.K., Cho Y.I., and Shyy W. *International Journal of Heat and Mass Transfer*, **35(2)**, 2823 (1992).

[71] Hess O. and Hess S. *Physica A*, **207(4)**, 517 (1994).

[72] Muller F.L. and Davidson J.F. *Industrial and Engineering Chemistry Research*, **33(10)**, 2364 (1994).

[73] Talwar K.K. and Khomani B. *J. Non-Newt. Fluid Mech.*, **57(2-3)**, 177 (1995).

[74] Manias E., Bitsanis I., Hadziioannou G., and Brinke G.T. *Europhysics Letters*, **33(5)**, 371 (1996).

[75] Doi M. and Edwards S.F. *J. Chem. Soc. Faraday Trans.*, **74**, 1789 (1978).

[76] de Gennes P.G. *J. Chem. Phys.*, **55**, 572 (1971).

[77] de Gennes P.G. *Scaling Concepts in Polymer Physics.* Cornell University Press, Ithaca New York, (1979).

[78] Graessley N. *Adv. Polym. Sci.*, **16**(1974).

[79] Ianniruberto G., Greco F., and Marrucci G. *Industrial and Engineering Chemistry Research*, **33(10)**, 2404 (1994).

[80] Rumpel H. and Pope J.M. *Mag. Res. Imag.*, **10(2)**, 187 (1992).

[81] Pope J.M., Rumpel H., Kuhn W., Walker R., Leach D., and Sarafis V. *Mag. Res. Imag.*, **9**, 357 (1991).

[82] Pope J.M., Walker R., and Kron T. *Mag. Res. Imag.*, **10**, 695 (1992).

[83] Rofe C.J., de Vargas L., Lambert R.K., and Callaghan P.T. *J. Rheol.*, **40(6)**, 1115 (1996).

[84] Mc Neely W.H. and Kang K.S. *Industrial Gums, 2nd ed.* Academic Press, New York, (1973).

[85] Cottrell I.W. and Kang K.S. *Dev. Ind. Microbiol.*, **7**, 161 (1978).

[86] Jansson P., Kenne L., and Lindberg B. *Carbohydr. Res.*, **45**, 275 (1975).

[87] Melton L.D., Mindt L., Rees D.A., and Sanderson G.R. *Dev. Ind. Microbiol.*, **46**, 245 (1976).

[88] Dintzis F.R., Babcock G.E., and Tobin R. *Dev. Ind. Microbiol.*, **13**, 257 (1970).

[89] Moorhouse R., Walkinshaw M.D., Arnott S., Sanford P.A., and Laskin A. *American Chemical Society Symposium*, **45**, 90 (1977).

[90] Whitcomb P.J. and Macosko C.W. *Rheology*, **22**, 493 (1978).

[91] Norton I.T., Goodall D.M., Frangou S.A., Morris E.R., and Rees D.A. *J. Mol. Biol.*, **175**, 392 (1984).

[92] Speers R.A. and Tung M.A. *J. Food Sci.*, **51(1)**, 96 (1986).

[93] Moorhouse R. *Kelco Div. of Merck & Co Inc.*(1987, Personal Communication).

[94] Coviello T., Kajiwara K., Burchard W., Dentini M., and Crescenzi V. *Macromol.*, **19**, 2826 (1986).

[95] Valdez M.A., Yeomans L., Montes F., Acuna H., and Ayala A. *Rheol. Acta*, **34**, 474 (1995).

[96] Cohen Y. and Metxner A.B. *J. Rheol.*, **29**, 67 (1985).

[97] Walters K. *Rheometry.* Chapman and Hall, London, (1975).

[98] Callaghan P.T., Cates M.E., Rofe C.J., and Smeulders J.B.A.F. *J. Phys II France*, **6**, 375 (1996).

[99] Spenley N.A., Cates M.E., and McLeish T.C.B. *Phys. Rev. Lett.*, **71**, 939 (1993).

[100] Callaghan P.T. *Polymer*, **29**, 1951 (1988).

[101] Sudmeijer O. Discussion, AG/32, Shell Laboratorium, Amsterdam, The Netherlands.

[102] Turner R. and Bowley R.M. *J. Phys. E*, **19**, 876 (1986).

[103] Jackson J.D. *Classical Electrodynamics.* Wiley, New York.

[104] Turner R. *J. Phys. D*, **19**, L147 (1986).

[105] Eccles C.D., Crozier S., Roffman W., Doddrell D.M., Back P., and Callaghan P.T. *Mag. Res. Imag.*, **12(4)**, 621 (1994).

[106] Mansfield P. and Morris P.G. *NMR Imaging in Biomedicine.* Academic Press, New York, (1982).

[107] Callaghan P.T., Forde L.C., and Rofe C.J. *J. Magn. Reson.*, **104**, 34 (1994).

[108] Rofe C.J., Van Noort J., and Callaghan P.T. *J. Magn. Reson.*, **108**, 125 (1995).

[109] Callaghan P.T., Coy A., Forde L.C., and Rofe C.J. *J. Magn. Reson.*, **101**, 347 (1993).

[110] Abragam A. *Principles of Nuclear Magnetism.* Oxford Uni. Press, Oxford/New York, (1961).

Author's Publications Arising From Thesis

- Rofe C.J., Lambert R.K. and Callaghan P.T.C. "Nuclear Magnetic Resonance Imaging of Flow for a Shear-Thinning Polymer in Cylindrical-Couette Geometry" *J. Rheol.*, **38(4)**, 875, (1994).
- Callaghan P.T., Cates M.E., Rofe C.J. and Smeulders J.B.A.F. "A Study of the 'Spurt Effect' in Wormlike Micelles using Nuclear Magnetic Resonance Microscopy" *J. Phys II France*, **6**, 375, (1996).
- Callaghan P.T., Forde L.C. and Rofe C.J. "Correlated Susceptibility and Diffusion Effects in NMR Microscopy using both Phase-Frequency Encoding and Phase-Phase Encoding" *J. Magn. Reson.*, **104**, 34, (1994).
- Rofe C.J., Van Noort J. and Callaghan P.T. "NMR Microscopy using Large Magnetic-Field Gradients" *J. Magn. Reson.*, **108**, 125, (1995).
- Callaghan P.T., Coy A., Forde L.C. and Rofe C.J. "Diffusive Relaxation and Edge Enhancement in NMR Microscopy" *J. Magn. Reson.*, **101**, 347, (1993).
- Rofe C.J. and de Vargas L. and Lambert R.K. and Callaghan P.T. "Nuclear Magnetic Resonance Imaging of Apparent Slip Effects in Xanthan Solutions" *J. Magn. Rheol.*, **40(6)**, 1115, (1996).